Diffusion-Weighted MR Imaging: Behaviors of Phenomenological Models and Enhanced PROPELLER Data Acquisition

by

Chu-Yu Lee

A Dissertation Presented in Partial Fulfillment
of the Requirements for the Degree
Doctor of Philosophy

Approved October 2012 by the
Graduate Supervisory Committee:

Josef Debbins, Co-Chair
Kevin Bennett, Co-Chair
Lina Karam
James Pipe

ARIZONA STATE UNIVERSITY

December 2012

ABSTRACT

The aim of this study was to investigate the microstructural sensitivity of the statistical distribution and diffusion kurtosis (DKI) models of non-monoexponential signal attenuation in the brain using diffusion-weighted MRI (DWI). We first developed a simulation of 2-D water diffusion inside simulated tissue consisting of semi-permeable cells and a variable cell size. We simulated a DWI acquisition using a pulsed gradient spin echo (PGSE) pulse sequence, and fitted the models to the simulated DWI signals using b-values up to 2500 s/mm^2. For comparison, we calculated the apparent diffusion coefficient (ADC) of the monoexponential model (b-value = 1000 s/mm^2). In separate experiments, we varied the cell size (5-10-15 μm), cell volume fraction (0.50-0.65-0.80), and membrane permeability (0.001-0.01-0.1 mm/s) to study how the fitted parameters tracked simulated microstructural changes. The ADC was sensitive to all the simulated microstructural changes except the decrease in membrane permeability. The σ_{stat} of the statistical distribution model increased exclusively with a decrease in cell volume fraction. The K_{app} of the DKI model increased exclusively with decreased cell size and decreased with increasing membrane permeability. These results suggest that the non-monoexponential models have different, specific microstructural sensitivity, and a combination of the models may give insights into the microstructural underpinning of tissue pathology.

Faster PROPELLER DWI acquisitions, such as Turboprop and X-prop, remain subject to phase errors inherent to a gradient echo readout, which ultimately limits the applied turbo factor and thus scan time reductions. This study

introduces a new phase correction to Turboprop, called Turboprop+. This technique employs calibration blades, which generate 2-D phase error maps and are rotated in accordance with the data blades, to correct phase errors arising from off-resonance and system imperfections. The results demonstrate that with a small increase in scan time for collecting calibration blades, Turboprop+ had a superior immunity to the off-resonance related artifacts when compared to standard Turboprop and recently proposed X-prop with the high turbo factor (turbo factor = 7). Thus, low specific absorption rate (SAR) and short scan time can be achieved in Turboprop+ using a high turbo factor, while off-resonance related artifacts are minimized.

DEDICATION

To my parents, my sister, my brother-in-law, and their children.

ACKNOWLEDGEMENTS

I would like to acknowledge Dr. Debbins for being supportive whatever research interests I like to pursue and explore since the beginning. I thank Dr. Bennett and Dr. Karam for their insightful comments, their time and passion I have shared for this work. I thank Dr. Pipe for creating a great team environment that I truly enjoy working at lab almost every day.

I also thank my colleagues at the Keller center. I am grateful for computing resources and image reconstruction codes that were developed and provided by my colleagues. My projects couldn't succeed without their help.

Finally, I want to thank my family in Taiwan: my parents, my sister, my brother-in-law and their children. They have been a greatest support and encouragement for me that I never feel alone while I am far away from home.

TABLE OF CONTENTS

Page

CHAPTER Page

CHAPTER Page

LIST OF TABLES

Table Page

LIST OF FIGURES

Figure Page

Figure Page

Figure Page

Chapter 1

INTRODUCTION

Diffusion-weighted magnetic resonance (MR) imaging (DWI) allows the non-invasive probing of tissue structures *in vivo* in a scale of a few microns, opening a broad spectrum of clinical applications [1,2]. Despite its clinical usefulness, there exists a gap between the signal changes of DWI and underlying tissue microstructure [3,4] that impedes the understanding of related pathological mechanisms.

The signal changes in DWI are typically modeled by the monoexponential model with a single parameter: apparent diffusion coefficient (ADC). The ADC model assumes free water diffusion in a homogeneous medium. In human brains, the monoexponential model is a good approximation at b-value = 1000 s/mm^2, providing a measure of the mean diffusivity [5]. When the b-value is high (b > 2000 s/mm^2), the signal attenuation of DWI *in vivo* has been observed to deviate from a monoexponential relation [6,7].

Several phenomenological models have been developed to fit the non-monoexponential decay at high b-values, and their fitted parameters have been demonstrated to be potential biomarkers [8-13]. However, relationship between the fitted parameters and tissue microstructure is unclear and has been an active research area.

The signal changes of DWI at high b-values arise from water protons with a slower diffusivity, which are expected to provide more information about interactions between water diffusion and microstructure at long diffusion times.

The hypothesis of this work is that these models of non-Gaussian water diffusion exhibit more specific sensitivities to microstructural changes relatively to the ADC. The hypothesis is tested by creating a Monte Carlo simulation of DWI experiments in a microenvironment composed of intra/extra-cellular compartments. Three simplified but pathologically relevant cell parameters: cell size, cell volume fraction, and membrane permeability are varied independently to study how the non-Gaussian water diffusion models correlate with the simulated biophysical changes.

Another challenge of DWI is in data acquisition, which are commonly performed by single-shot echo planar imaging (EPI) method [14]. EPI method is a fast imaging method and is insensitive to patient motion. However, it suffers from geometric distortion and ghosting artifacts. The image resolution is also limited.

An alternative approach is PROPELLER (Periodically Rotated Overlapping Parallel Lines with Enhanced Reconstruction) [15]. It is a multi-shot, fast spin echo (FSE) technique, providing high resolution images with minimal image artifacts. The major issues with PROPELLER are long scan time and high SAR. To address these issues, Turboprop [16] and X-prop [17] have been proposed to reduce scan time and SAR by incorporating gradient and spin echo (GRASE) sequence [18]. However, those methods remain subject to the phase error particularly at a high acceleration (turbo factor). This study presents a new phase correction to the turbo PROPELLER (Turboprop), called 'turboprop+'. Turboprop+ allows a high turbo factor, which further reduces scan time and SAR, without compromising the image quality. The technique could be a promising tool for clinical and research DWI.

The following is a summary of the upcoming chapter contents:

Chapter 2 introduces basic principles of MRI, including relaxation, image contrasts, and imaging method.

Chapter 3 presents the fundamentals of diffusion physics, covering from Einstein's theory of Brownian motion to anomalous diffusion. The water diffusion in biological tissues is also discussed.

Chapter 4 introduces diffusion-weighted MR imaging, including the current methods of biophysical modeling and data acquisition.

Chapter 5 presents a study of behaviors of the non-monoexponential DWI models using a clinical study and a Monte Carlo simulation.

Chapter 6 proposes the developments of the whole-blade method and turboprop+ to address issues with PROPELLER.

Chapter 7 summarizes the contributions presented in this work and discusses future directions.

Chapter 2

MR PHYSICS

Nuclear magnetic resonance (NMR) is a physical phenomenon that was first discovered independently by Felix Bloch and Edward Purcell, who shared the Nobel Prize in physics in 1946 for this discovery. At that time, NMR was used to study the molecular structures and composition of chemical substances in chemistry and physics. Until 1973, the first NMR spatial image was constructed by Paul Lauterbur through the use of linear field gradients. This imaging technique, called magnetic resonance imaging (MRI), allows for *in vivo* probing tissue properties from various, unique perspectives, greatly facilitating the advancement of biology and medicine.

MRI shares the similarities with computer tomography (CT). Both belong to tomographic modalities that produce the anatomic images of a selected part of the body. However, there are two fundamental differences. First, unlike X-ray in CT, MRI poses no risk of ionizing radiation by applying magnetic fields and delivering radio waves through the body. Secondly, image contrast in CT is dependent on the attenuation of the X-ray beams, which are related to the electron density and effective atomic number of the tissues. The contrast derived in MRI offers immense flexibility, reflecting compositions of chemical elements and dynamics of physical mechanisms. For instance, MRI is able to measure the homodynamic response during the neuron activation, the method called functional MRI (fMRI). Another example is the arterial spin labeling (ASL), which quantify

the tissue perfusion through the blood flow dynamics. Nonetheless, the drawbacks of MRI include high cost, long scan time, and various image artifacts.

This chapter introduces basic MRI principles, starting from single atomic nuclei to the macroscopic magnetization in an image voxel. The basic MRI contrasts and imaging methods are discussed. The contents of this chapter are summarized from references [19-21].

2.1 Origins of the MR Signal

2.1.1 Nuclear Spin and Magnetic Moment

Atomic nuclei are composed of protons and neutrons, both of which possess two physical properties: spin angular momentum and magnetic momentum. Spin angular momentum can be envisaged as a rotation around its axis. The orientation of the axis is related to the magnetic moment (μ), a behavior that is referred as a magnetic dipole and can be described by the right-hand rule in a classical picture (Fig. 2.1). A nucleus can be composed of multiple protons and neutrons, and its net magnetic moment is thus the vector sum of the magnetic moments of all the protons and neutrons. Because the pair of protons or neutrons tends to produce magnetic moments with opposite directions, their resulting net magnetic moments cancel out. For instance, the common isotope of carbon: ^{12}C is with 6 protons and 6 neutrons exhibits no net magnetic moment and cannot be used for MRI. Instead, ^{1}H only consists of one single proton and is abundant in human body. Therefore, it is by far the most used nucleus for MRI, and is the main focus of this dissertation.

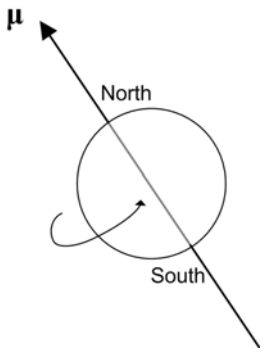

Figure 2.1: Illustration of a conceptual magnetic dipole with a north and south poles. The strength and orientation of this rotation is given by the magnetic moment: μ.

2.1.2 Magnetization

The basic idea of MRI is to detect the magnetic moment through Faraday's law of induction, so the large net magnetic moment is required to induce a detectable current in a coil. However, the magnetic moments of hydrogen ^1H in human body are oriented randomly, and the net magnetic moment is zero. To ensure the magnetic moments of protons are aligned in a single direction, a strong, static magnetic field B_0 is applied to human body, creating a net magnetization. The amount of the net magnetization is related to the energy distribution. For hydrogen ^1H, the gap between two energy states are:

$$\Delta E = \gamma h B_0 \tag{2.1}$$

where γ is the gyromagnetic ratio; $\gamma = 42.5$ MHz for ^1H. The lower energy state E_1 with spin population N_1 in tends to align with the direction of the applied static magnetic field B_0, whereas the higher energy state E_2 with spin population N_2 tends to orient in opposite to the direction of the magnetic field. The ratio of spin populations N_2 to N_1 is governed by the Boltzman distribution:

$$\frac{N_1}{N_2} = \exp(\frac{\Delta E}{kT}) \tag{2.2}$$

where k is Boltzmann's constant and T is absolute temperature. With T equals room temperature, the difference in the spin populations can be approximated to be:

$$N_1 - N_2 = (\frac{h\gamma}{2k})\frac{B_0(N_1+N_2)}{T} \tag{2.3}$$

This indicates that the detectable magnetization is proportional to the strength of static magnetic field B_0 and the total protons, but is inversely proportional to the absolute temperature. The proportion of 'excess' spins, however, is very small (~ 10^{-6}) at room temperature (~ 300 K) and B_0 ~ 1.5 T.

2.1.3 Precession and Radiofrequency Excitation

When a spin is placed in the applied static magnetic field B_0, a torque is exerted on the spin toward the alignment with the B_0. Because the spin with the magnetic moment has its own rotation, these combined forces lead to the spin precession around the axis of the B_0 (Fig. 2.2a). The angle with the B_0 depends on the initial orientation of spins (Fig. 2.2b). The angular frequency ω of spin precession is proportional to the B_0:

$$\omega_0 = \gamma B_0 \tag{2.4}$$

The angular frequency of spins with random orientations is identical. But because spins' orientations are random, the net magnetic moment of spins: M only exists along the longitudinal direction, proportional to the number of excess spins (Eq. (2.3)), whereas the transverse magnetic moments cancel out.

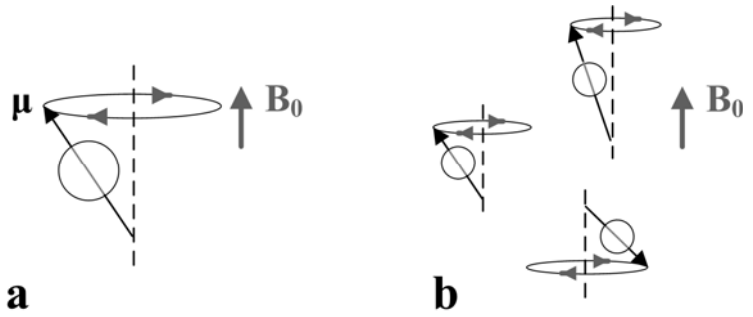

Figure 2.2: a: Spin precession with the magnetic moment: μ in the presence of a static magnetic field B_0. b: Multiple spin precession with random orientations.

Through the use of static applied magnetic field B_0, the magnitude and direction of a net magnetic moment are stationary at thermal equilibrium. The stationary net magnetic moment is unable to induce a detectable electric current, according to Faraday's low of induction. In MRI, radiofrequency (RF) waves are applied to irradiate the protons and disturb thermal equilibrium. This results in a net transverse magnetic moment rotating with the angular frequency ω (Eq. (2.4)). Because this disturbing of thermal equilibrium with applied radio waves is temporary, system eventually re-attains thermal equilibrium. The electromagnetic radiation (EM radiation) is the mechanism that produces image contrasts of MRI. The EM radiation is also applied in computer tomography (CT). The essential difference is that the energy induced by RF waves in MRI is much lower than the energy by X-rays in CT, and poses no health risk to human body.

To irradiate the protons, the RF energy has to be exactly fills the energy gap: ΔE (Eq. (2.1) between two (low and high) energy states:

$$\Delta E = h\nu_{RF} \tag{2.5}$$

In other words, the RF waves have to oscillate in resonance with the angular frequency of protons (ω). When this energy gap is filled, the energy exchange

occurs between the two populations of protons with low energy state and high energy state.

Figure 2.3 illustrates a classical figure of this energy exchange. An applied static magnetic field leads to a spin precession around the axis of the magnetic field. If another magnetic field B_1 rotating at the identical angular frequency as the spin precession is applied at the transverse plane, it exerts a torque tipping the magnetic moment into transverse plane (Fig. 2.3a). When the magnetic moments move toward the transverse plane, the net magnetization M, which is originally pointed at longitudinal direction, also moves toward the transverse plane. Because the spins and magnetic field B_1 rotate at the same angular frequency (ω), the dynamic behavior of the net magnetization M can be described in a rotating frame (Fig. 2.3b). The flip angle: θ is related to the length of time t when the magnetic field B_1 is applied.

$$\theta = \gamma B_1 t \tag{2.6}$$

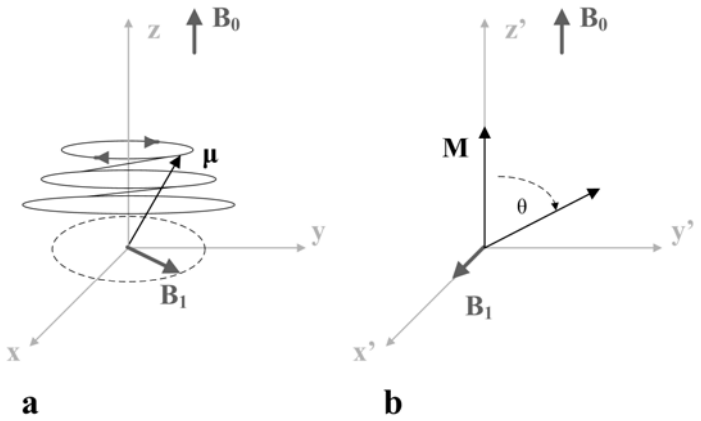

Figure 2.3: The evolution of a spin magnetic moment: μ (a) and a net magnetization: M (b) in the presence of a static magnetic field B_0 (z direction) and a magnetic field B_1 rotating in resonance with the spin precession (x, y plane). The net magnetization: M is in the rotating frame (x', y', z').

2.2 Relaxation and Image Contrasts

2.2.1 Bloch Equation

The RF magnetic field B_1 is applied for a short period of time. When it is removed, the RF energy emission starts to take place, and the system gradually regains thermal equilibrium, where the net magnetization re-aligns with the direction of the static magnetic field: B_0. The rate of this RF energy emission depends on the chemical and physical environment of the spins, giving rise to the MRI contrasts. The evolution of the net magnetization: $\overline{M} = [M_x, M_y, M_z]^T$ during the RF energy emission can be classically described by the Bloch Equation:

$$\frac{d\overline{M}}{dt} = \overline{M} \times \gamma \overline{B} - \frac{(M_x \bar{x} + M_y \bar{y})}{T_2} - \frac{(M_z - M_0)}{T_1} \bar{z} \qquad (2.7)$$

$\overline{B}$ is the applied magnetic field, including the static magnetic field B_0 and RF magnetic field B_1. M_0 is the net magnetization at the thermal equilibrium.

Assuming the RF magnetic field B_1 is just removed, and the applied magnetic field $\overline{B}$ only includes the static magnetic field B_0 applied along z axis, the time derivative of the net magnetization:

$$\frac{dM_x}{dt} = \omega_0 M_y - \frac{M_x}{T_2} \tag{2.8}$$

$$\frac{dM_y}{dt} = -\omega_0 M_x - \frac{M_y}{T_2} \tag{2.9}$$

$$\frac{dM_z}{dt} = -\frac{(M_z - M_0)}{T_1} \tag{2.10}$$

The resulting time evolving magnetization:

$$M_x(t) = (M_x(0)\cos(\omega_0 t) + M_y(0)\sin(\omega_0 t))e^{-\frac{t}{T_2}} \tag{2.11}$$

$$M_y(t) = (M_x(0) - \sin(\omega_0 t) + M_y(0)\cos(\omega_0 t))e^{-\frac{t}{T_2}} \tag{2.12}$$

$$M_z(t) = (M_z(0))\, e^{-\frac{t}{T_1}} + (1 - e^{-\frac{t}{T_1}})\, M_0 \tag{2.13}$$

The equations (2.11-2.13) indicate that the transverse magnetization rotates around the z-axis with an angular frequency ω_0, and attenuates to zero when time goes to infinite ($t \rightarrow \infty$). The longitudinal magnetization progressively grows to the equilibrium magnetization M_0. The relaxation rates T_1 and T_2 are to be discussed in the later sections.

2.2.2 T_1 and T_2 relaxation

As described in Eq. (2.13), T_1 is the rate that determines how long of the longitudinal magnetization M_z reaches to the equilibrium magnetization M_0. This process involves RF energy emission from the nuclear spin system to its external environment, so T_1 relaxation is also called “spin-lattice” relaxation. Similar to RF energy radiation (Sec. 2.1.3), this RF energy emission of a spin needs to be

induced through a surrounding magnetic field fluctuating near the angular frequency of spin precession (ω_0). The molecular tumbling rate is related to the molecular size and the state where the molecule is bounded or restricted. When the water is in a partially bounded or restricted state as bounded to proteins and other macromolecules, T_1 relaxation is the most effective, and T_1 relaxation time is short. Instead, for free water or protons on large macromolecules and in membrane lipids, the molecular tumbling rate is either too fast or too slow relatively to ω_0, and T_1 relaxation time in those tissues is long.

T_2 determines the rate of the attenuation of transverse magnetization M_{xy} (Eq. (2.11-2.12). The RF energy emission results in an attenuation of transverse magnetization M_{xy}, and a re-growth of longitudinal magnetization M_z. However, T_2 relaxation can also result from a change in the local magnetic field that lead to a loss of phase coherence of spins. The change in the local magnetic field is non-stationary and occurs when there is an interaction between spins or an alternation in the chemical environment. Therefore, T_2 relaxation is called "spin-spin" relaxation. If the molecular tumbling rate is slow, protons experience the local magnetic field inhomogeneity, and the incoherent phases of protons shorten T_2 relaxation time. Conversely, if the molecular tumbling rate is fast, the incoherent phases of protons caused by the local magnetic field inhomogeneity is averaged out in a short period of time, leading to a long T_2 relaxation time.

These additional factors that lead to T_2 relaxation make the T_2 relaxation time shorter than the T_1 relaxation time. Another difference is that T_2 relaxation is less dependent on the static magnetic field B_0, which related to angular frequency of spin precession (ω_0) (Eq. (2.4)). At the static magnetic field B_0 = 1.5 T, the T_1

relaxation time of gray and white matter are around 800 and 900 ms, and the T_2 relaxation time of gray and white matter are around 100 and 92 ms [21].

2.2.3 Free Induction Decay

The net magnetization: M right after the 90º RF pulse is on the transverse plane rotating at the frequency (ω_0) (Eq. (2.11-2.12)). If a receiver coil is placed along the direction of the transverse plane, the time-varying magnetization: M induce an electric current oscillating at the frequency (ω_0) and the amplitude of the current attenuates with time when the spin phase progressive loses phase coherence (Fig. 2.4). The detected signal decay is called free induction decay (FID).

This decay rate of the transverse magnetization M_{xy} is determined by T_2 relaxation (Eq. (2.11-2.12)). In reality, there are other factors that also create the phase incoherence of protons, including B_0 magnetic field inhomogeneity and magnetic susceptibility. Thus, the decay rate of FID is faster than T_2, and is called T_2^* ($T_2^* < T_2$). These factors create frequency shifts from the angular frequency of spin precession (ω_0) that are stationary. The separation of the stationary frequency shifts and T_2 relaxation is expressed as:

$$\frac{1}{T_2^*} = \frac{1}{T_2} + \frac{1}{T_{2\_int}} \tag{2.14}$$

where T_{2_int} refers to the decay rate resulting from the stationary frequency shifts.

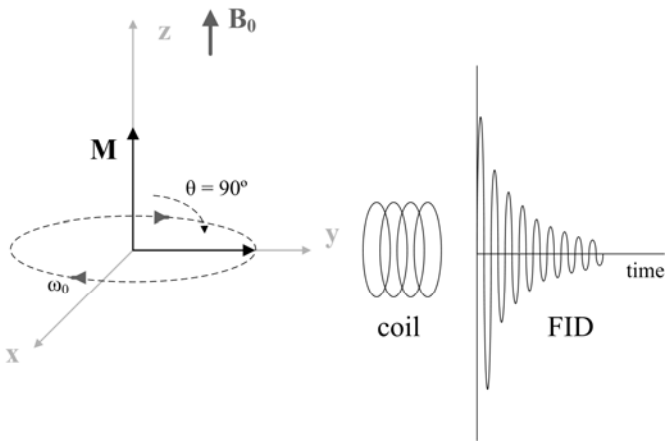

Figure 2.4: The magnetization M immediately after a 90º RF pulse and an induced free induction decay (FID) from a receiver coil.

2.2.4 Spin Echo and T_2 Contrast

T_2 relaxation is a result of non-stationary frequency shifts of spin precession, a fact that can be used to separate it from T_2^* attenuation. In this section, a method used to produce T_2 contrast is described, called "spin echo". As shown in Fig. 2.5, spins de-phase immediately after a 90º RF pulse, leading to a FID (T_2^* attenuation). At time t_2, the phase shift ($\Delta\theta$) due to the stationary frequency shift ($\Delta\omega_0 = \gamma\Delta B_0$) can be represented by:

$$\Delta\theta_{t2} = \omega_0(t_2 - t_0) \tag{2.15}$$

This phase shift is a factor of $(t - t_0)$. It indicates that if this phase is reversed, it is possible to re-create the phase coherence at t_3 by applying a 180º RF pulse at time t_2 to reverse the phase shift $\Delta\theta_{t2}$ to $-\Delta\theta_{t2}$. If $(t_3 - t_2)$ equals $(t_2 - t_0)$, the accumulated phase shift at time t_3:

$$\Delta\theta_{t3} = \omega_0(t_3 - t_2) + (-\omega_0(t_2 - t_1)) = 0 \tag{2.16}$$

Thus, the phase coherence is re-created (Fig. 2.5). The echo produced by this phase coherence is called "spin echo". The time t_3 is called "echo time" (T_E).

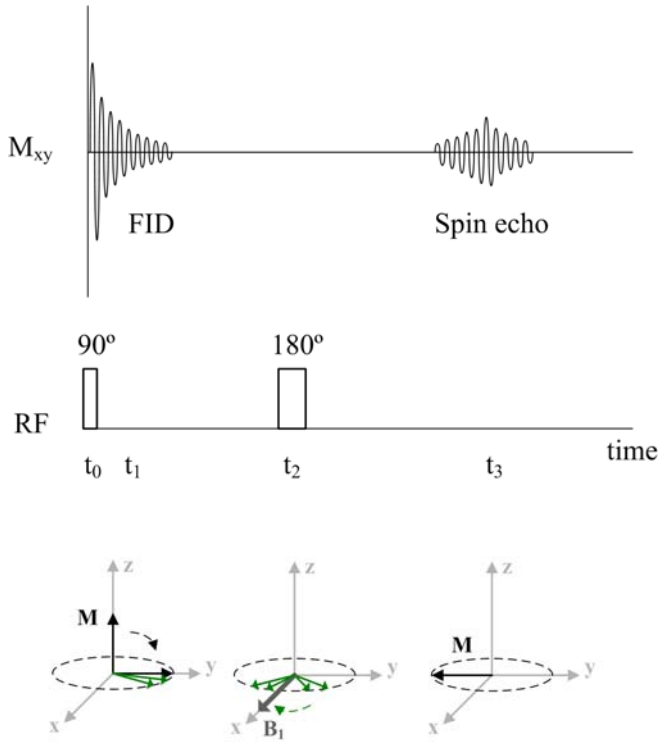

Figure 2.5: Time-evolution of transverse magnetization M_{xy} and spin phases during applications of RF pulses (B_1) of 90º and 180º.

The spin echo method is a very important development in MRI by allowing: (1): a measurement of T_2 relaxation and (2): an adjustment of echo time (T_E). Because different tissues have different T_2 relaxation, the flexibility of adjusting T_E enables the optimization of T_2 contrast in tissues.

2.2.5 Gradient Echo and T_1 Contrast

In spin echo method, 180º RF refocusing pulse has to be placed after the FID to avoid the signal overlap between FID and spin echo (Fig. 2.5). Therefore, T_E is normally long in spin echo method. Long T_E is beneficial to optimization of T_2 contrast in tissues, but not suitable for optimized T_1 contrast in tissues that requires a short T_E. To produces an echo at short T_E, the section describes a method, called "gradient echo".

As shown in Fig. 2.6, a magnetic field gradient is applied immediately after a 90º RF pulse. A negative lobe gradient creates a de-phasing effect to the FID, leading to a very rapid decay of FID. Then a positive gradient lobe creates a re-phasing effect, producing an echo at T_E, where the negative and positive gradients cancel each other, and the signal continues to attenuate after T_E.

Since the re-phasing effect by the positive gradient lobe is only acted on the de-phasing effect by the negative gradient lobe, those phase shifts caused by T_2^* relaxation still persist, and the magnitude of the gradient echo is affected by T_2^* relaxation:

$$M_{xy}(t_E) = M_0 e^{-\frac{t_E}{T_2^*}} \tag{2.17}$$

As described in Eq. (2.10), T_1 relaxation determines the rate of re-growth of longitudinal magnetization M_z. It indicates that to generate image contrast between different tissues, the echo should be produced before the longitudinal magnetization M_z of tissues reaches the thermal equilibrium M_0. Second, because only transverse magnetization is detectable (Fig. 2.4), a 90º RF pulse is required to "tip" the longitudinal magnetization M_z into the transverse plane.

One standard method for detecting T_1 relaxation is the inversion-recovery pulse sequence (Fig. 2.7). Immediately after a 180º RF pulse, the initial longitudinal magnetization M_z is $-M_0$, and it starts to re-grow at a rate T_1. The longitudinal magnetization at time t_2 before a 90 º RF pulse is:

$$M_z(t_2) = (1 - 2\, e^{-\frac{t_2}{T_1}})\, M_0 \tag{2.18}$$

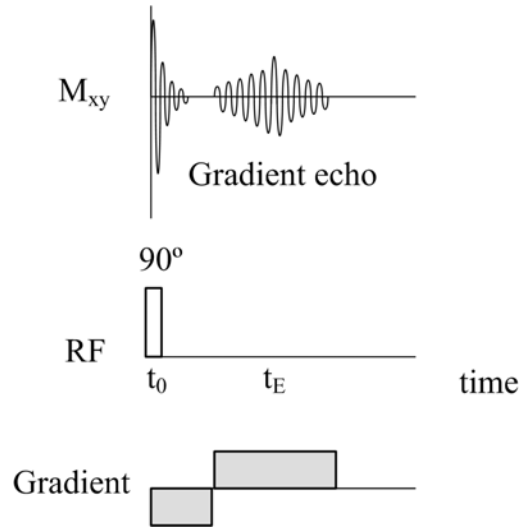

Figure 2.6: Time evolution of transverse magnetization M_{xy} with applications of a 90º RF pulse and magnetic field gradient.

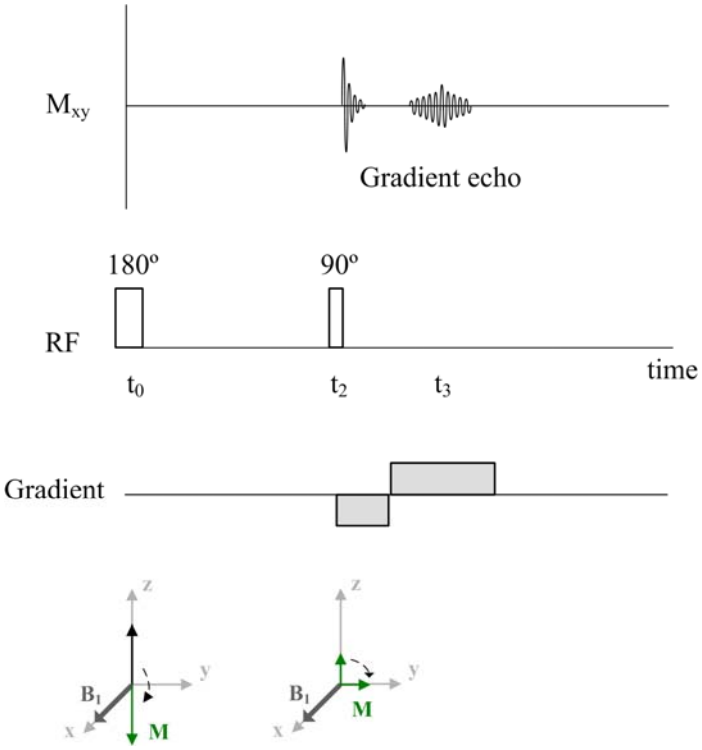

Figure 2.7: Illustration of pulse sequence: inversion recovery and the time evolution of transverse magnetization.

After a 90º RF pulse, the longitudinal magnetization M_z is tipped into the transverse plane, and it attenuates at a rate T_2^*. The transverse magnetization M_{xy} at time t_3 can be represented:

$$M_{xy}(t_3) = e^{-\frac{(t_3 - t_2)}{T_2^*}} |1 - 2\, e^{-\frac{t_2}{T_1}}|\, M_0 \qquad (2.19)$$

2.3 2-D Imaging Methods

This section describes the most common way to collect 2-D images using a slice selection and a subsequent 2-D spatial encoding (frequency-encoding and phase-encoding).

2.3.1 Frequency-encoding and *k*-space

When a magnetic gradient is applied along longitudinal direction (Fig. 2.8), a linearly increasing magnetic field is created. Because a RF excitation requires a condition of resonance, oscillating frequency of RF magnetic field B_1 can be adjusted to match the precession frequency of the selected slice location. The bandwidth (BW) of the RF magnetic field is the slice thickness Δz:

$$BW = \gamma\, G_z\, \Delta z \qquad (2.20)$$

Ideally, the RF magnetic field function $B_1(t)$ is a time-infinite sinc function sinc(t), corresponding to a rectangular function in frequency domain. In reality, the truncation effect of the sinc function leads to a tapering-off effects of the rectangular function in frequency domain. This non-rectangular slice profile could possibly excite tissues outside a prescribe slice, an effect called “cross-talk”. In clinical MR imaging, it is commonly to leave a small gap between slices.

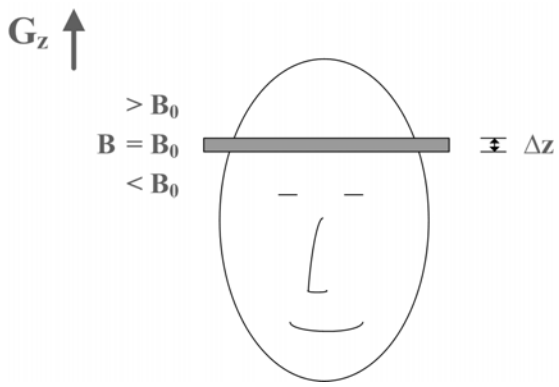

Figure 2.8: Illustration of slice-selective excitation using a magnetic filed gradient G_z.

After a RF field succeeds in exciting a slice, spatially localized information of transverse plane (x, y) is needed to produce a 2-D image. For instance, tissues A and B are located at different location and have different relaxation rate T_2^* (Fig. 2.9). If a FID is collected right after the excitation, the data consists of a combined T_2^* from tissues A and B. However, when a magnetic gradient is applied along x direction, the precession frequency of tissue A (ω_A) is slower than that of tissue B (ω_B). Thus, the T_2^* decay from tissue A and tissue B can be differentiated through the Fourier transform of the FID signal (Fig. 2.9). This Fourier relationship (time (t) versus precession frequency (ω)) can be represented as:

$$s(t) = \int m(\omega)\, \exp(-i\omega t)\, d\omega \qquad (2.21)$$

where $\omega = \gamma G x$. Through the variable transformation, this Fourier relationship can be converted to a space (x) versus spatial frequency (k_x):

$$s(k_x) = \int m(x)\, \exp(-ik_x x)\, dx \qquad (2.22)$$

where $k_x = \gamma G t$ or $k_x = \gamma \int_0^t G(\tau) d\tau$. Eq. (2.22) describes how a spatially information can be encoded by a applied magnetic gradient G.. The method is call

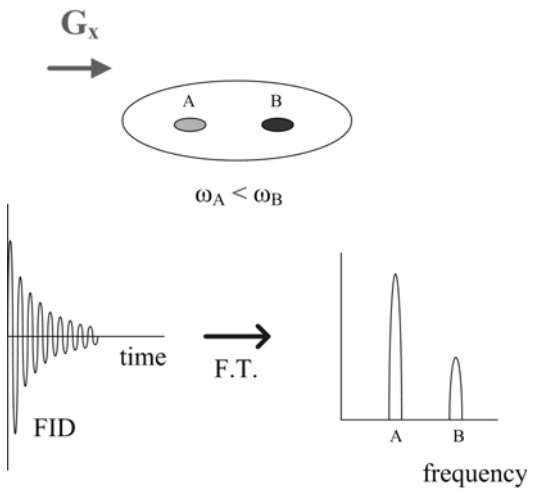

Figure 2.9: Illustration of spatial localization method using a magnetic gradient applied along x. The Fourier transform (F.T.) of FID signals yield two peaks located at ω_A and ω_B ($\omega_A < \omega_B$).

frequency-encoding method. The spatial frequency domain k_x is referred as *k*-space.

k-space scheme is very helpful in illustrating the trajectory of collecting MRI signals. Figure 2.10 shows an example of *k*-space trajectory using gradient echo method. Despite the *k*-space traversal occurs during the time interval t_0-t_1-T_E-t_2, the data acquisition is only performed during the time interval t_1-t_E-t_2. There are several reasons for selecting this acquisition time interval. First, the center of *k*-space, which contains the most information of object, can be well collected at a controllable timing (t_E). Because of the hardware limitation and patient safety concern, there is a rise time for gradient to settle and data acquisition cannot be started immediately at t_0 (Fig. 2.10). Second, the accuracy and uniformity of *k*-space data can be improved. The magnitude of an image object normally is slow-varying in space, so the signal intensity outside the central *k*-space is small. If data acquisition starts from the center of *k*-space, the small signal intensity out-

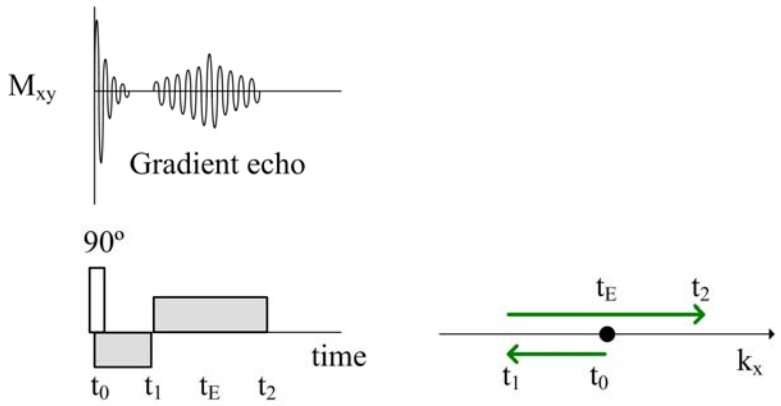

Figure 2.10: Illustration of *k*-space trajectory of the gradient echo method.

side the central *k*-space is even diminished by T_2 or T_2^* relaxation. This relaxation effects could potentially result in a filtering effect, creating an image blurring.

2.3.2 Phase-encoding

For a 2-D image, it requires a data acquisition along k_y direction of *k*-space. Because only one data point is collected at a time, it is impossible to simultaneous apply frequency encoding along y direction. However, the phase information in Fourier transform can be used to help with spatial localization in y direction. As shown in Fig. 2.11, the first wave vector adds no phase into the collected signals. The measured signals would be signals A + C oscillating at ω_1, and signals B + D oscillating at ω_2. The second wave vector adds a 180º phase to the first row (A and B) and a zero phase to the second raw (C and D). The measured signals would be signals - A + C oscillating at ω_1, and signals - B + D oscillating at ω_2. Therefore, signals A and C, and signals B and D can be solved through the measured signals at ω_1 and ω_2 respectively.

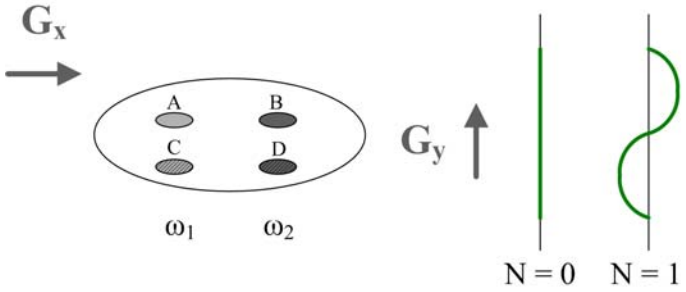

Figure 2.11: Illustration of frequency-encoding gradient G_x and phase-encoding gradient G_y, where $\omega_2 > \omega_1$. Two wave vector created by G_y: N = 0 ($G_y = 0$), and N = 1 ($G_y = (\gamma\, t_y\, L_y)$-1). ty is the time duration of phase-encoding gradient. L_y is the object length in y direction.

The higher resolution in y direction thus requires more data collection along phase-encoding direction to resolve the signals in y direction. For instance, a data matrix of 128 × 128 requires 128 phase-encoding lines. The 2-D image can then be obtained through a 2-D Fourier transform:

$$s(k_x,k_y) = \int m(x, y)\, \exp(-i(k_x x + k_y y))\, dxdy \qquad (2.23)$$

where $k_x = \gamma\int_0^t G_x(\tau)d\tau$, $k_y = \gamma\int_0^t G_y(\tau)d\tau$.

2.3.3 2-D Spin Echo Pulse Sequence

Normally, it is difficult to complete a 2-D *k*-space sampling in one excitation, due to the T_2^* and T_2 relaxation. One way is to perform multiple excitations for each echo. In each excitation, there is an additional time period after echo time T_E because the longitudinal magnetization has to be fully recovered from the previous excitation. The time interval between each excitation is called repetition time T_R (Fig. 2.12). In human brains, T_R is larger than T_E by a factor above 10, because T_1 relaxation time is longer than T_2 relaxation time. The total scan time for 2-D *k*-space sampling is thus (number of phase-encoding lines) × T_R.

2.3.4 Small Flip Angle and Gradient Echo Pulse Sequence

In spin-echo method with a flip angle of 90º, the fully recovered magnetization requires a long T_R and a long scan time ((number of phase-encoding lines) $\times$ T_R). When a small flip angle of RF pulse is used, it takes less time for full recovery of M_z (smaller T_R). The scan time thus can be potentially reduced with a small flip angle. This section describes the gradient echo method with a small flip angle.

Instead of assuming a full recovery of M_z in spin echo method, a special situation is considered where a serial of RF pulses of equal flip angle (α) are applied in order to maintain a steady-state longitudinal magnetization M_z (Fig. 2.13). Assuming that T_2^* relaxation is negligible (very short T_E), the transverse magnetization right after the excitation is:

$$m_{xy} = \frac{(1- \exp(-T_R /T_1))}{(1- \cos(\alpha) \exp(-T_R /T_1))} \sin(\alpha) \qquad (2.24)$$

For fixed T_1 and T_R, the flip angle α that maximizes the transverse magnetization m_{xy} is:

$$\alpha = \cos^{-1}(\exp(- T_R /T_1)) \qquad (2.25)$$

α is called “Ernst angle”.

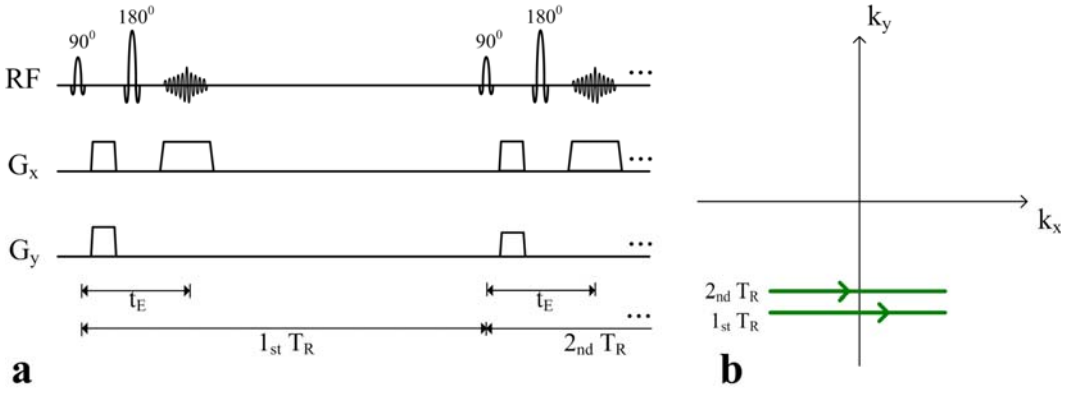

Figure 2.12: a: Diagram of 2-D spin echo pulse sequence: RF pulses (RF), frequency-encoding gradients (G_x), phase-encoding gradients (G_y). b: corresponding *k*-space trajectory of 1st and 2nd T_R.

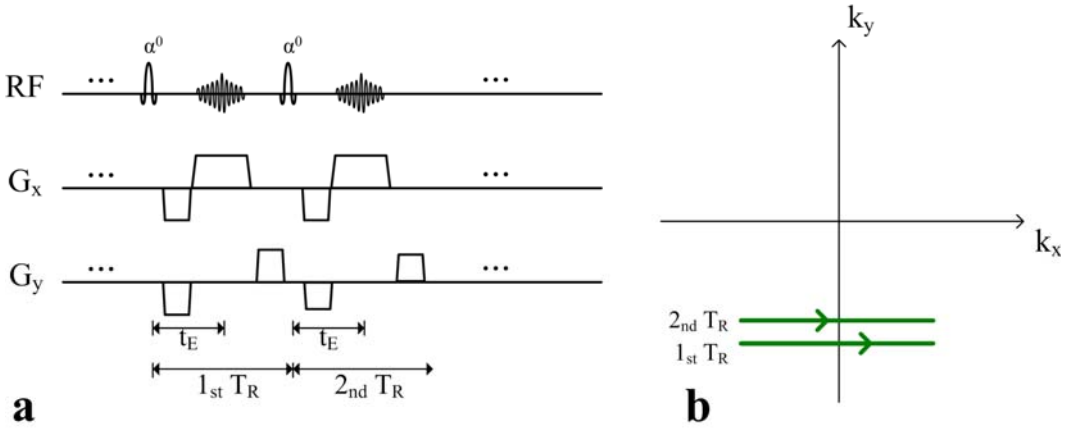

Figure 2.13: a: Diagram of 2-D gradient echo pulse sequence with a small flip angle α: RF pulses (RF), frequency-encoding gradients (G_x), phase-encoding gradients (G_y). b: corresponding *k*-space trajectory of 1st and 2nd T_R.

2.4 Imaging Considerations

2.4.1 Image Contrast

Both spin echo and gradient echo methods have controllable parameters: flip angle, echo time (T_E), and repetition time (T_R) that allow the flexibility of reflecting image contrast.

The spin echo method has an inherent long T_E, and eliminates T_2^* relaxation using a 180º RF pulse. It is typically used to measure T_2 relaxation. It employs a 90º RF pulse to maximize the transverse magnetization M_{xy}, and a long T_R to minimize T_1 relaxation and ensure the fully recovered longitudinal magnetization M_z.

The gradient echo method has an inherent short T_R to reduce the scan time, and is normally used to measure T_1 relaxation, and also allows the measurements of proton density and T_2^* relaxation. For a typical T_1 value of human brain: 800 ms and a T_R: 30 ms, the Ernst angle is around 30º. The larger flip angle increases T_1 contrast, and a smaller flip angle increases the contrast of proton density. In clinical applications, the flip angle α is adjusted with respect to the Ernst angle to increase the image contrast and also maximize the signal. T_2^* contrast is based on the chosen T_E. A long T_E increases T_2^* contrast.

2.4.2 Off-resonance

The rationale of 2-D spatial-encoding by applying frequency and phase-encoding gradients assumes that spin precession frequency of an image volume is identically ω_0 with an applied static magnetic filed B_0, a condition called “on-resonance”. Therefore, the created frequency and phase differences by

the magnetic field gradients are used to differentiate different spatial location of an image. However, there are factors that lead to the shifts from the precession frequency (ω_0) and thus interferes the spatial encoding. These factors can be generally categorized into: (1) static field B_0 inhomogeneity, (2) magnetic susceptibility, and (3) chemical shift.

The B_0 magnetic field inhomogeneity originates from imperfections of generated magnetic field. Most MRI machines provide additional equipments to minimize the magnetic field inhomogeneity, an action referred as shimming.

Magnetic susceptibility and chemical shift are related to the interactions between the molecular structure and the external applied magnetic field B_0. When an object is placed in a magnetic field, currents are induced through its electrons, producing an internal magnetic field, which augments (paramagnetism) or opposes (diamagnetism) the external magnetic filed B_0. Water and organic molecules are diamagnetic, while the metals (Cr, Fe, Mn, Co) and air are paramagnetic. The differences in magnetic susceptibility of tissues, such as an air-tissue interface create local magnetic field inhomogeneity.

Chemical shift refers to the reduced magnetic field experienced by the proton because of chemical shielding of electron clouds. For instance, the spin precession frequency of proton in fat is measured to be approximately 3.5 ppm slower than that of proton in water. In 1.5 Tesla, this shift of precession frequency is around 223 Hz. This specific frequency shift is used to suppress the effects of chemical shift, such as fat suppression.

Magnetic susceptibility and chemical shift are proportional to the strength of applied magnetic field. Therefore, while high filed magnet brings a higher magnetization and SNR (Eq. (2.3), issues of field inhomogeneity are exacerbated.

This spatially dependent shift of precession frequency can be represented as: $\Delta\omega(x, y)$. If the variation of $\Delta\omega(x, y)$ is very rapid in space, the phase dispersion occurs in an image voxel, resulting in a T_2^* relaxation. This T_2^* relaxation mitigated by using a smaller voxel size.

Here, an effect of the frequency shift: $\Delta\omega(x, y)$ on the frequency and phase-encoding of convention 2-D spin echo method (Fig. 2.12) is described.

Assuming there is a field inhomogeneity along frequency-encoding direction: $\Delta\omega(x) = \gamma G_x' x$, the measured signal during an acquisition time interval can be represented as:

$$s(k_x(t),k_y(t) = \int m(x, y) \exp(-i\, k_x(1+\frac{G_x'}{G_x})\, x - i\, k_y y))\, dxdy \qquad (2.26)$$

This indicates that this frequency shift results in a pixel shift along frequency-encoding direction.

If field inhomogeneity occurs along phase-encoding direction: $\Delta\omega(x) = \gamma G_y' y$, the measured signal at n_{th} phase-encoding step:

$$s(k_x(t), k_y(n) = \int m(x, y) \exp(-i\, k_x x - i\, (k_y + \gamma G_y' \tau) y)\, dxdy \qquad (2.27)$$

This indicates that the frequency shift results in a constant shift in *k*-space along k_y direction, corresponding to a linear phase ramp in image-space.

The spin echo method can eliminate T_2^* relaxation, but cannot reduce other effects of field inhomogeneity, including a pixel shift and a linear phase ramp in

an image. The phase of the image can simply removed after image reconstruction. The issue of a pixel shift can be mitigated by increasing the bandwidth of data acquisition.

2.4.3 Noise

Noise is an important concern in MRI, because of the original limited signal and the rapid relaxation. The noise originates from random electrical fluctuations in the receiver coil and human body, producing a detectable voltage. It can be statistically modeled as additive random Gaussian noise.

Because the noise is random, its power (σ^2) is proportional to the bandwidth of frequency spectrum:

$$\sigma^2 \propto \mathrm{BW} = \frac{1}{\Delta t} \tag{2.28}$$

where Δt (1/BW) is the sampling rate of data acquisition. If a signal-to-noise ratio (SNR) is defined as signal amplitude divided by the noise deviation:

$$\mathrm{SNR} = \frac{A}{\sigma} \tag{2.29}$$

The slower sampling rate (larger Δt) and signal averaging are helpful to reduce the noise power. One can easily prove that the SNR is proportional to $\sqrt{\text{scan time}}$.

Another way to increase SNR is by increasing the signal. The signal is proportional to the voxel size, defined by (slice thickness) $\times$ (field-of-view)/sampling points. The SNR dependence on these two imaging parameters can be represented as:

$$\mathrm{SNR} \propto \sqrt{\text{scan time}}\ (\text{voxel size}) \tag{2.30}$$

Chapter 3

DIFFUSION PHYSICS

Brownian motion was first observed by Robert Brown, who described it as the irregular, jittering movement of small particles suspended in a fluid, such as liquid or gas [22]. The underlying mechanism of Brownian motion was unclear until Einstein established its relation with the molecular kinetic theory [23]. This resulted in the connection between the thermal driven movement of individual molecules and the mass transport of diffusion resulting from concentration gradients. The physical properties of the particles and fluid can be derived given the measurement of the diffusion coefficient. Besides, the irregular molecular movement can be described using the random walk model.

These theoretical formulations by Einstein assume that the suspended particles diffuse in a homogeneous fluid, called normal diffusion. This assumption no longer holds in the presence of heterogeneous medium or physical compartments common to various real-world phenomenon. Anomalous diffusion [24] is used to describe the molecular movements deviating from the normal diffusion. The physical factors that lead to anomalous diffusion are unclear and remain a topic of active research. The anomalous diffusion in the biological tissues [25] is the primary focus of this study.

3.1 Brownian Motion and Diffusion

The jiggling movement of Brownian motion has been ascribed to the collisions between particles. According to the molecular kinetic theory, the average kinetic energy of the suspended particles is $k_B\ T \times 3/2$, where k_B is the

Boltzmann constant and T is the temperature. By considering a dynamic equilibrium between the force exerted on the moving particle and the diffusion from the thermal molecular movement, the diffusion coefficient is given as [23]:

$$D = \frac{k_B T}{6\pi\pi\eta} \tag{3.1}$$

where T is the temperature, r is the radius of the particle, η is the viscosity of the fluid, k_B is the Boltzmann constant. The relation was derived assuming the state of thermal equilibrium. Thus, for a given universal parameters (k_B and T), the diffusion coefficient is only dependent on the viscosity of the fluid and the particle sizes. This essence of the equation is that it relates the mass transfer to the microscopic physical quantity of the suspended particles and fluid.

As the direction of particle movement reverses constantly in an irregular way, the displacement is used to measure this movement. By selecting a time interval Δt that is short with respect the observation interval but long enough to experience several molecular collisions, the movements between the two successive intervals are regarded as statistically independent. The step of particle movement during the time interval Δt is Δx moving in any direction with equal probability $P(\Delta x)$:

$$\int_{-\infty}^{\infty} P(\Delta x) d\Delta x = 1 \tag{3.2}$$

If the number of particles per unit volume is defined as f(x,t), a function of location and time, f(x,t) can be expanded with respect to time and location through a perturbation theory:

$$\frac{\partial f(x,t)}{\partial t} = D \frac{\partial^2 f(x,t)}{\partial x^2} \tag{3.3}$$

where the diffusion coefficient D:

$$D = \frac{\int_{-\infty}^{\infty} \Delta x^2 P(\Delta x) d\Delta x}{2\Delta t} \tag{3.4}$$

Eq. (3.3) is exactly the diffusion equation with the analytical solution:

$$f(x,t) = \frac{1}{\sqrt{4Dt\pi}} \exp(-\frac{x^2}{4Dt}) \tag{3.5}$$

Obviously, f(x,t) is a Gaussian distribution function. The diffusion coefficient D:

$$D = \frac{\overline{x^2}}{2t} \tag{3.6}$$

Eq. (3.6) indicates that the variance of particle displacement is proportional to the diffusion time t. The diffusion equation in Eq. (3.3) was previously derived by Adolf Fick [26]. The main distinction here is that this relates the behavior of the movement of one suspended particle to the diffusion equation, which governs the mass transfer in the present of concentration gradient.

3.2 Random Walk Model

Through an appropriate selection of time interval Δt, the time-evolving Brownian motion can be modeled with a random walker taking step Δx toward random directions. Considering a 1-D case with equal probability moving right or left: $P(\Delta x) = P(-\Delta x) = 0.5$, the location *s* after N steps of random walking:

$$s = \Delta x_1 + \Delta x_2 + \Delta x_3 + ...\Delta x_N \tag{3.7}$$

According to the central limit theorem [27], when the N is sufficiently large, s approaches a normal distribution:

$$f(s) = \frac{1}{\sqrt{2var[s]\pi}} \exp(-\frac{s^2}{2var[s]}) \tag{3.8}$$

where the mean and variance:

$$E[s] = 0 \tag{3.9}$$

$$\text{var}[s] = N\Delta x^2 \tag{3.10}$$

Based on eq. (3.4), $D = \Delta x^2 / 2\Delta t$, and $t = N\Delta t$, f(s) can be given as:

$$f(s) = \frac{1}{\sqrt{4Dt\pi}} \exp(-\frac{s^2}{4Dt}) \tag{3.11}$$

which is the same equation derived from the diffusion equation (Eq. 3.5). As the assumption stated by Einstein, time interval Δt has to be short relatively to the observation interval t, inferring a sufficiently large N ($N = t/\Delta t$), a displacement of molecular movement is expected to be Gaussian distributed. The Monte Carlo simulation was performed to validate the random walk model, as shown in Fig. 3.1. The simulated molecular displacement is approximately Gaussian distributed, and its variance increased linearly with the diffusion time, consistent with the relation in Eq. (3.5-3.6).

3.3 Anomalous Diffusion

The random walk model formulates the time-evolving displacement probability density function (pdf) utilizing the nice properties of central-limit theorem. It relies on the assumptions: (1): the pdf of step Δx is symmetric with the zero first moment (mean) and finite second moment (variance), (2): the time interval Δt is fixed, (3): the steps Δx between different time intervals are statistically independent, and (4): number of steps N has to be sufficiently large.

The various physical phenomena that violate the above assumptions have been observed to deviate from the behaviors of normal diffusion. The deviation generally refers to a non-linear relation between the mean squared displacement and diffusion time, in contrast with the linear relation in normal diffusion (Eq. 3.6). The possible factors that contribute to anomalous diffusion include structural

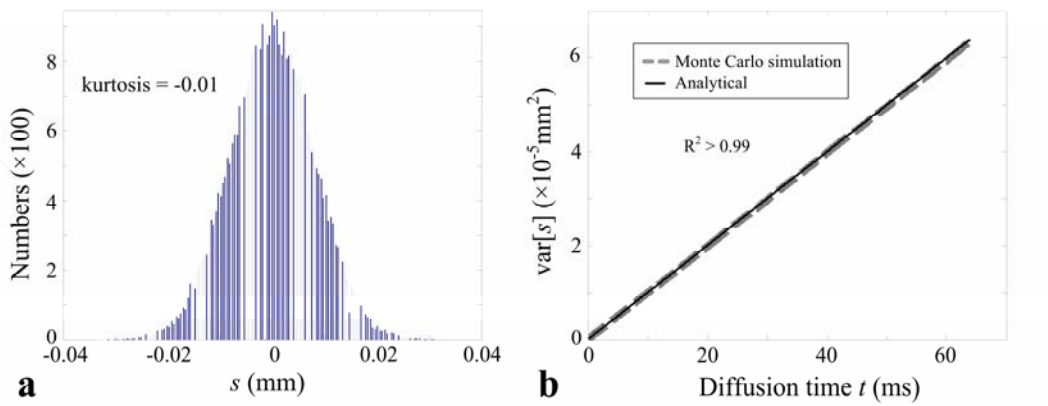

Figure 3.1: Monte Carlo simulation of the Brownian motion; 40'000 random walkers with step size Δx : 2.24×10^{-4} mm and time interval Δt : 5×10^{-2} ms. D = 5×10^{-4} mm^2/s (Eq. (2.4)). a: Histogram of molecular displacement at diffusion time: 64 ms. b: Variance of displacement versus diffusion time.

heterogeneity, interactions between physical compartments, and dynamical structural variations [24]. Several physically-motivated modifications are thus made to the original assumptions of the normal diffusion. Continuous time random walk (CTRW) [24] provides a theoretical framework dealing with the deviations of the normal diffusion. When the step Δx of random walks has the finite variance but the time interval is power-law distributed, exhibiting a heavy-tail behavior:

$$f(\Delta t) \sim \frac{1}{\Delta t^{1+\alpha}} \quad 0 < \alpha < 1 \tag{3.12}$$

The relation between the mean square displacement and the diffusion time is:

$$\overline{x^2} \sim t^{\alpha} \tag{3.13}$$

As in Eq. (3.12), larger α ensures smaller probability of large Δt . When $\alpha = 1$, it is the same linear relation as in Eq. (3.6). When α is smaller, the higher probability of large Δt means that the time interval between successive steps can be long, slowing down the random walks, called 'sub-diffusion'. Conversely, the time

interval has a finite expected value, whereas the step x is power-law distributed:

$$f(\Delta x) \sim \frac{1}{\Delta x^{1+\beta}} \quad 0 < \beta < 2 \tag{3.14}$$

and the resulting relation between the mean square displacement and the diffusion time is:

$$\overline{x^2} \sim t^{2/\beta} \tag{3.15}$$

Larger β ensures smaller probability for larger jumps, whereas the smaller β ensures the larger chance of big jumps, speeding up the random walk, called 'super-diffusion'. In the situation where both the step Δx and time interval Δt are power-law distributed, the relation between the mean square displacement and time is:

$$\overline{x^2} \sim t^{2\alpha/\beta} \tag{3.16}$$

The non-linear relations of sub- and super-diffusion (Eq. (3.13), (3.15)) are shown in Fig. 3.2.

3.4 Diffusion in Biological Tissues

The thermal-driven diffusion is related to the particle size and the fluid viscosity (Eq. (3.1) with a dynamic behavior that is dependent on the structural complexity (Sec. 3.3). As the biological mechanisms involve dynamical molecular transport among and between cellular compartments, diffusion provides a viable means to assess the structures *in vivo*. The section introduces several biological factors including biophysical mechanisms and microstructures that are relevant to the diffusion behaviors *in-vivo*. The primary focus is on the interaction between intra- and extra-cellular compartments. Please note that the coverage here is far from being complete, as some aspects of this topic still remain open problems.

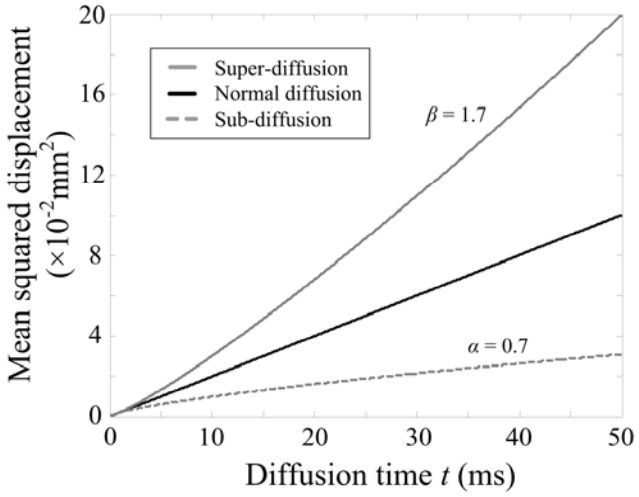

Figure 3.2: The mean squared displacement versus diffusion time in the case of super-diffusion (Eq. (3.15)), normal diffusion (Eq. (3.6)), and sub-diffusion (Eq. (3.13)). The diffusion coefficient D is 1.0×10^{-3} mm^2/s.

A simplified illustration of diffusion in cell compartment is shown in Fig. 3.3. The movement of the extra-cellular space follows the tortuous path bouncing around the cell membrane, whereas the intra-cellular movement is relatively restricted. The inter-compartmental exchange is related to the membrane permeability. Those interactions with cell compartment happen given a sufficiently long diffusion time, providing the opportunity to probe the microstructures in a non-invasive way.

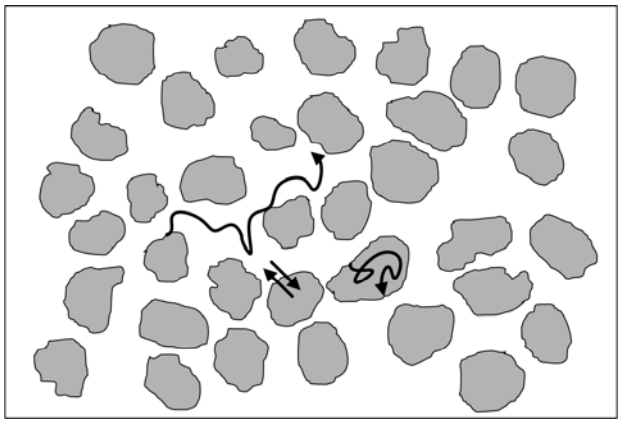

Figure 3.3: Simplified cell structure with intra/extra-cellular (gray/white color) compartments. Arrows indicates the path of intra-, extra-, and inter-cellular movement.

3.4.1 Compartmental Diffusion

At short times, without the interaction between the molecule and cell barrier, the movement behaves in normal diffusion, as described in Eq. (3.1-3.6). In consideration of the general geometry of the media, including the closed pores, a suspension of solids, or a well-connected porous media, when the diffusion time is intermediate, only some portion of molecules experiences the porous barriers. The time-dependent diffusion coefficient D(t) can be derived as a function of surface-to-volume ratio [5]:

$$D(t) = D_0\left(1 - \frac{4}{9\sqrt{\pi}}\frac{S}{V_p}(D_0 t)^{0.5}\right) + O(D_0 t) \qquad (3.17)$$

D_0 is a free diffusion coefficient. S/V_p denotes the pore surface-to-volume ratio, which is a very important parameter characterizing the chemical or biological reactions in a confined geometry. This is a monotonically decreasing function, inferring that the diffusion coefficient D(t) decreases with the diffusion time. The

relation in Eq. (3.17) applies to the intra and extra-cellular diffusion with impermeable membrane illustrated in Fig. 3.3.

At long times, in the case of diffusion in the closed pore, analogous to the intra-cellular diffusion with zero membrane permeability in Fig. 3.3, the intra-cellular diffusion coefficient $D_{in}(t)$ is given by:

$$D_{in}(t) \sim \frac{L_s^2}{2t} \tag{3.18}$$

L_s denotes the pore size. Eq. (3.18) means that the diffusion coefficient is only dependent on the pore size, and approaches to zero as the diffusion time reach the long time limit. Another case is the diffusion in the connected porous medium, analogous to the extra-cellular diffusion with impermeable membrane in Fig. 3.3. The extra-cellular diffusion coefficient $D_{ex}(t)$ is given by [28]:

$$D_{ex}(t \to \infty) \sim \frac{D_0}{\lambda^2} \tag{3.19}$$

$\lambda > 1$ is a tortuosity factor, quantifying the increase in the diffusing path length in a complex medium. The relation between the tortuosity factor (λ) and physical structure is implicit. Some studies have derived the relation between λ and cell volume fraction for randomly placed cell geometry of spheres and cylinders using an effective medium theory [29,30].

3.4.2 Compartmental Diffusion with Exchange

The exchange between compartments plays an important role in biological system, governing the transport of nutrition and ion balance. The barrier permeability κ is defined as [31]:

$$J = \kappa \Delta C \tag{3.20}$$

J is the particle flux density, and ΔC is the difference of the concentration on both

sides. For an equally space plane with distance l, the diffusion coefficient at the long time limit [32]:

$$D(t \to \infty) = \kappa l/(\kappa l/D_0 + 1) \tag{3.21}$$

D_0 is the free diffusion coefficient at short time limit. Another parameter of exchange is the mean lifetime τ within the individual compartment [31]:

$$\tau = \int_0^\infty [1 - \gamma(t)]dt \tag{3.22}$$

$\gamma(t)$ is the relative amount of molecules, which move out of the compartment. For a sphere with radius R:

$$\tau = R^2/15D_0 + R/3\kappa \tag{3.23}$$

This means that the residing time within the compartment is larger when compartment size is larger or the barrier permeability is lower.

A simplified scheme of exchange between two compartments is discussed, assuming D_{in} and D_{out} are the intrinsic diffusion coefficients in intra/extra-cellular compartments with the number of molecular density inside and outside the cell: n_{in}/n_{ex}. Based on the definition of the membrane permeability κ, the flux from intra-cellular compartment to extra-cellular compartment is given by:

$$J_{in\to ex} = \kappa (n_{in} - n_{ex}) \tag{3.24}$$

The flux can also be represented by the molecular movements across the membrane with a drift velocity *v*:

$$J_{in\to ex} = (1/4)v_{in}(n_{in})p_{in\to ex} - (1/4)v_{ex}(n_{ex})p_{ex\to in} \tag{3.25}$$

The intra/extra-cellular drift velocities are calculated as: $v_{in/out} = \sqrt{6D_{in/out}/\delta}$, where δ denotes the small time interval during the molecular movement. By equaling Eq. (3.24) and Eq. (3.25), the membrane permeability κ can be

represented as [30]:

$$\kappa = (1/4)v_{in}\, p_{in\to ex} = (1/4)v_{ex}\, p_{ex\to in} \tag{3.26}$$

This is an important relation describing the molecular density balance between two compartments. The compartment with the larger molecular drift velocity has a smaller probability of crossing the membrane. This also provides a framework of the random walk model in a confined geometry with exchange between two compartments.

Chapter 4

DIFFUSION-WEIGHTED MR IMAGING

As described in the Chapter 3, the dynamics of diffusion correlate with the dimensions of physical compartments and the inter-compartmental exchange. Water accounts for 70% of the composition of the human body, and thus diffusion measurement in the human body is of tremendous clinical value, enabling the probe of microstructure in a non-invasive way. The diffusion measurement requires a highly sensitive tracer of molecular movement, which is of a scale of few microns. MRI achieves the goal by labeling spins using a strong spatially dependent magnetic field. Besides, by means of the directionality of the diffusion, the fiber tract mapping can be created by the diffusion tensor imaging (DTI).

To establish the relation between the diffusion measurement and the underlying microstructure, the biophysical modeling is required. The biophysical models of diffusion MRI can be broadly categorized into phenomenological model and analytical model. Compared with phenomenological model, analytical model normally involve more parameters completely defining physical geometry and mechanisms. Ideally, the distinction between these two categories is obvious given sufficient, uncorrupted measurements. In reality, however, the accuracy of measurements is limited by the SNR, image artifacts and distortions, which are issues with data acquisition of diffusion MRI. In this chapter, fundamentals of diffusion MRI are introduced, covering from the biophysical modeling and data acquisition.

4.1 Pulsed-Gradient Spin Echo Sequence

The pulse-gradient spin echo (PGSE) sequence [33], shown in Fig. 4.1, is typically used in diffusion MRI. The net phase of a i_{th} single spin at the end of the PGSE sequence is:

$$\theta_i = \gamma g(\int_0^{\delta} r_2(t)dt - \int_0^{\delta} r_1(t)dt) \tag{4.1}$$

$r_1(t)$ and $r_2(t)$ denote the spin location during the first and second gradient pulses. The first gradient pulse is used to generate spatially dependent phase dispersion. The phase dispersion of static spins is refocused after the 180° refocusing RF pulse and the second gradient pulse, whereas the incoherent phase of moving spins causes de-phasing effect, resulting in signal attenuation. This sequence thus sensitizes the movements during the time Δ between the two diffusion gradient pulses, defined as diffusion time. The net phase becomes larger when gradient strength g is larger for the same displacement between two gradient pulses. Therefore, the larger gradient strength g, the more sensitive of the PGSE sequence to the molecular movement.

For free diffusion, the signal attenuation as a function of parameters of PGSE sequence is easily derived by virtues of the statistics of Gaussian displacement PDF (Eq. (3.5)). The relation can be derived using two ways: macroscopic approach [33,34] and random walk approach [34,35].

4.1.1 Macroscopic Approach

The Bloch-Torrey equation describes the time-evolving macroscopic magnetization during the T_1 and T_2 relaxation. The effect of diffusion on the macroscopic magnetization is represented by the diffusion equation (Eq. 3.3).

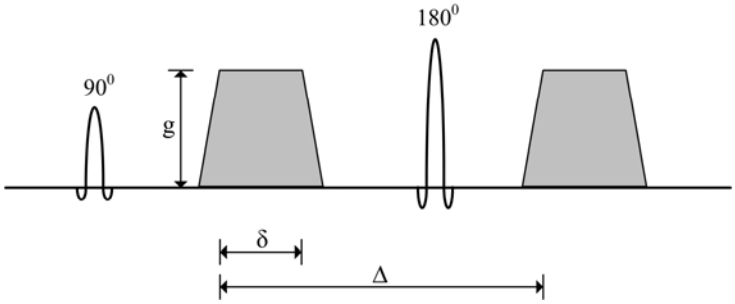

Figure 4.1: Illustration of pulse-gradient spin echo sequence; δ (the width of the gradient pulse) and Δ (diffusion time) are the timing parameters of gradient pulse, and g is the gradient strength.

Neglecting the T_1 relaxation, the net magnetization $M(\vec{r},t)$ in the presence of diffusion gradients is given by:

$$\frac{\partial M(\vec{r},t)}{\partial t} = -i\,\gamma\,\vec{r}\,\vec{g}\,M(\vec{r},t) + D\frac{\partial^2 M(\vec{r},t)}{\partial r^2} - \frac{M(\vec{r},t)}{T_2} \tag{4.2}$$

$\vec{r}$ is the spin location, and $\vec{g}$ is the diffusion gradient. By assuming net magnetization $M(\vec{r},t)$ is in a form of:

$$M(\vec{r},t) = A(t)\exp(-i\,\gamma\,\vec{r}\int_0^t g(t')dt')\exp(-t/T_2) \tag{4.3}$$

This form assumes that molecular movement is geometrically symmetric, and has no effect on the spin phase but resulting in the decay of magnitude A(t) of net magnetization [36]. This decay is dependent of the spin displacement Δr and is independent of the spin location $\vec{r}$ [36]. By applying eq. (4.3) to eq. (4.2), A(t) is give by:

$$A(t) = \exp(-D\gamma^2\int_0^t(\int_0^{t'} g(t'')dt'')^2\,dt') \tag{4.4}$$

In the case of PGSE sequence, A(t) is represented as:

$$A(t) = \exp(-D\gamma^2 g^2\delta^2(\Delta - \delta/3)) \tag{4.5}$$

Back to eq. (4.3), $\int_0^t g(t')t' = 0$ at the end of PGSE sequence, and $M(\vec{r},t)$ is:

$$M(\vec{r},t) = \exp(-D\gamma^2 g^2 \delta^2 (\Delta - \delta/3))\exp(-t/T_2) \tag{4.6}$$

Eq. (4.6) is a very important relation, where the diffusion coefficient D can be calculated from measured signal attenuation $M(\vec{r},t)$ in a PGSE experiment.

4.1.2 Random Walk Approach

For each random walker, every step is sensitized by an applied pulsed gradient. The accumulated phase of single spin after the first pulse gradient with the width δ, and δ takes n time increments ($\delta = n\Delta t$):

$$\theta(\delta = n\Delta t) = \gamma G \Delta t \sum_{i=1}^{n} (n + 1 - i)\Delta x_i \tag{4.7}$$

Δx_i is the step take at i_{th} time increment with $E[\Delta x] = 0$, $var[\Delta x] = 2D\Delta t$, and $E[\Delta x_i]E[\Delta x_j] = 0$. This phase modulation on the transverse magnetization can be calculated by the ensemble average of this phase accumulation:

$$\overline{\exp(i\theta)} = \int_{-\infty}^{\infty} P(\theta)\exp(i\theta)\,d\theta \tag{4.8}$$

Because Δx is independent and identically distributed random variable, θ is a Gaussian distributed according to the central limit theorem [27], and $\overline{\exp(i\theta)} = \exp(-\overline{\theta^2}/2)$ for a Gaussian distribution. From Eq. (3.7), $\overline{\exp(i\theta)}$ is given by:

$$\overline{\exp(i\theta)} = \exp(-\frac{1}{3}\gamma^2 g^2 D\,\delta^3) \tag{4.9}$$

For the second pulsed-gradient in the PGSE sequence, it is assumed to start right after the 180° RF focusing pulse; $\delta = \Delta$. The resulting ensemble average of the phase accumulation [34]:

$$\overline{\exp(i\theta)} = \exp(-\frac{2}{3}\gamma^2 g^2 D\,\delta^3) \tag{4.10}$$

This is consistent with the signal attenuation derived using the macroscopic approach (Eq. (4.6)), where Δ is set to be equal to δ.

4.2 q-Space Model

The relation between the PGSE measurements and the diffusion coefficient in Eq. (4.6) and (4.10) assumes the free diffusion. In this aspect, the signal decay has a linear relation with the square of gradient strength (g^2) and diffusion time (Δ) (Eq. (4.6) and (4.10)). Diffusion in a confined geometry with compartmental exchange, its closed form solution is rather difficult to obtain. However, the analytical solution can be derived by assuming the width of the pulsed-gradient to be closely zero, which is generally referred as the short gradient pulse (SGP) approximation.

From Eq. (4.1), when the gradient pulse width approaches to zero, the net phase of a single spin in a PGSE sequence:

$$\lim_{\delta \to 0} \theta_i = \gamma \, \delta \, g \, r_2 - \gamma \, \delta \, g \, r_1 \tag{4.11}$$

The ensemble average of this phase modulation, which is very similar to Eq. (3.8), but the integral is calculated over all the starting and ending location r_1 and r_2:

$$\overline{\exp(i\theta)} = \iint P(r_1) P(r_2 \mid r_1) \exp(i \, \gamma \, \delta \, g \, (r_2 - r_1)) dr_1 r_2 \tag{4.12}$$

The equation can be simplified by defining an average propagator P(R), which is a displacement distribution, calculated through the integral over all the starting locations r_1:

$$P(R) = \int P(r_1) P(r_1 + R \mid r_1) dr_1 \tag{4.13}$$

For free diffusion, the displacement R is independent of the starting location r_1,

and P(R) is a Gaussian distribution function. Eq. (4.12) can be rewritten as:

$$\overline{\exp(i\theta)} = \int P(R)\exp(i\gamma\,\delta\,g\,R)dR \tag{4.14}$$

As described in Sec. 4.1, the phase modulation because of diffusion results in an attenuated magnitude of magnetization. This decay in magnitude is a function of diffusion time and the parameters of PGSE sequence (g, δ). By defining the parameter $q = \gamma\,\delta\,g$, the signal attenuation in Eq. (4.14) is given by:

$$E(q,\Delta) = \int P(R)\exp(i\,q\,R)dR \tag{4.15}$$

q is the spatial wave vector with respect to the molecular displacement R, called q-space. The relation in Eq. (4.15) is very useful, providing a structural relevant average propagator through the Fourier transform of signal attenuation. Please note that the q-space requires SGP approximation. This Fourier relation is analogous to the Fourier relation between image-space and *k*-space, where *k* denotes the spatial wave vector with respect to the image location.

For free diffusion, the average propagator P(R) is independent of the starting location r_1. The signal attenuation of free diffusion is given by:

$$E(q,\Delta) = \exp(-q^2 D\,\Delta), \text{ where } q = \gamma\,\delta\,g \tag{4.16}$$

This relation is consistent with the derived signal decay of the PGSE sequence with the zero pulsed-gradient width (δ = 0).

For restricted diffusion in a confined geometry, including plane, cylinder, and sphere, the average propagator and signal attenuation in Eq. (4.15) has been derived [37-40]. Figure 4.2 plots the analytical expression of signal attenuation for diffusion in a plane. The diffraction pattern in the SGP limit $(\delta \to 0)$ happens at the factor of the product of wave vector q and planar spacing L. This conforms

to the perception that the moving spins keep being reflected at the barrier boundaries. This is very useful information as the diffraction patterns provide the information of the spatial dimensions, and has been experimentally observed in vitro [41]. However, no observation of the diffraction has been made in the experiments *in vivo*. This may be due to the violation of SGP approximation (Fig. 4.2) [40], compartmental exchange, SNR limit [42] and large variations of compartmental sizes [43,44]. Nonetheless, in *in vivo* experiments, the parameters derived from the displacement profile have been found to correlate with the pathology, including the mean square displacement [42] and kurtosis [45].

4.3 Apparent Diffusion Coefficient

The displacement profile derived from the q-space model in Eq. (4.15) provides statistical behavior of molecular displacement without the assumption about the geometry of the structures. However, the SGP approximation is difficult to achieve in practice, because the maximum gradient strength is limited by the hardware. Besides, the calculation of the displacement profile also requires multiple measurements of signal attenuation at different wave vector q, which prolongs the scan time.

An alternative approach is to apply the phenomenological model, which requires only a few measurements and can be easily implemented in a clinical setting. A most commonly used model is the mono-exponential model, providing a quantitative measure of water diffusion, called apparent diffusion coefficient (ADC).

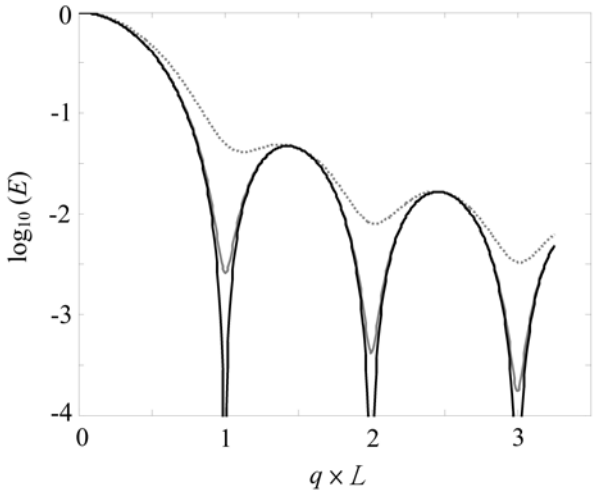

Figure 4.2: Signal attenuation (E) versus the wave vector q × L in the limit of SGP approximation from top to bottom $(\delta \to 0)$. L is a spacing between planes.

$$S(b) = S(0)\exp(-b \times ADC) \tag{4.17}$$

b is a factor of diffusion weighting, defined as: $\gamma^2 g^2 \delta^2 (\Delta - \delta/3)$. S(0) is the T_2 relaxation without diffusion weighting. Eq. (4.17) is equivalent to Eq. (4.6), describing the signal decay in a PGSE experiment for a free diffusion. However, unlike Eq. (4.6), where the mono-exponential relation holds for all the b-values, Eq. (4.17) is a phenomenological fitting model normally applied with b = 1000 s/mm^2.

The typical gradient strength is 40 mT/m of a 3 Tesla clinical scanner and $\delta \approx \Delta \approx 24$ (ms) of b = 1000 s/mm^2. For a free diffusion coefficient: 3 × 10^{-3} mm^2/s (37 °C), the RMS displacement in a 3-D space is around 30 μm, which is larger than the typical human cell size 10 μm. The measured diffusivities using Eq. (4.17) assuming isotropic diffusion is around 1 × 10^{-3} mm^2/s for gray and white matter and 2 × 10^{-3} mm^2/s for cerebrospinal fluid (CSF) in human brain. They

are slower than the pure water as the interactions between water molecules and cell compartments is expected to slow down the measured diffusivity.

For free diffusion in a homogenous medium, the applied diffusion weighting acts equally on all the diffusing molecules with the same diffusivity. However, for diffusion in a heterogeneous structure, the molecules move at the different diffusivities, and the measured diffusivity depends on the applied b-value. At lower b-value (b-value $\leq$ 200 s/mm^2), the perfusion effects mainly contribute to the signal decay. When b is greater than 2000 s/mm^2, the molecules experiencing the restricted diffusion mainly contribute to the signal decay. However, the diffusion weighting at high b-value is limited by SNR.

The ADC value has been shown to be sensitive to the microstructural changes during various pathological states. For instance, ADC values were found to decrease after the onset of ischemic stroke [46], and has an inverse correlation with the tumor cellularity [2]. The reduction in ADC has been attributed to the decrease in membrane permeability [47], increase in cell volume fraction [29], and extracellular tortuosity [48]. It suffices to say that those mechanisms correlate with the reduction in ADC, but the exact mechanism underlying the pathological changes remains difficult to identify [3].

4.4 Diffusion Tensor Imaging

It is straightforward to envisage the directional dependence of diffusion as diffusion time is long enough for water molecule to encounter the barriers. Particularly, brain white matter is composed aligned axons coated with myelin (Fig. 4.3), and the strong directional dependence of brain white matter has been

observed from the early experiments [49,50]. The axon diameter is around 1-20 μm. Thus, in a PGSE experiment, the diffusion perpendicular to the axon orientation is relatively restricted compared with the direction along the axon orientation. This anisotropic information can be analytically represented by a 3x3 diffusion tensor.

$$\begin{bmatrix} D_{xx} & D_{xy} & D_{xz} \\ D_{yx} & D_{yy} & D_{yz} \\ D_{zx} & D_{zy} & D_{zz} \end{bmatrix} \tag{4.18}$$

The diffusion tensor $\overline{D}$ is a symmetric matrix with positive eigen-values: $\lambda_1, \lambda_2, \lambda_3$ and orthogonal eigen-vectors: e_1, e_2, e_3, which is illustrated as an ellipsoid (Fig. 4.3). It can be incorporated into the mono-exponential relation of ADC (Eq. 4.17). This is done by replacing the scalar of gradient strength *g* with a 3-D vector $\overline{g}$.

$$\begin{bmatrix} g_x \\ g_y \\ g_z \end{bmatrix} \tag{4.19}$$

The mono-exponential relation in Eq. (3.17) can be represented as:

$$\log \frac{S(b)}{S(0)} = -\gamma^2 \, \overline{g}^T \overline{D} \overline{g} \delta^2 (\Delta - \frac{\delta}{3}) \tag{4.20}$$

The diffusion tensor $\overline{D}$ is a symmetric matrix, so at least six diffusion measurements along different directions $\overline{g}$ are required to calculate $\overline{D}$. The direction is commonly selected as uniformly distributed unit vectors in space, such as icosahedron and dodecahedrons [51]. More directions of diffusion measurements yields better estimate of diffusion tensor $\overline{D}$ [52]. However, it may offer no advantage using more than 6 directions [53].

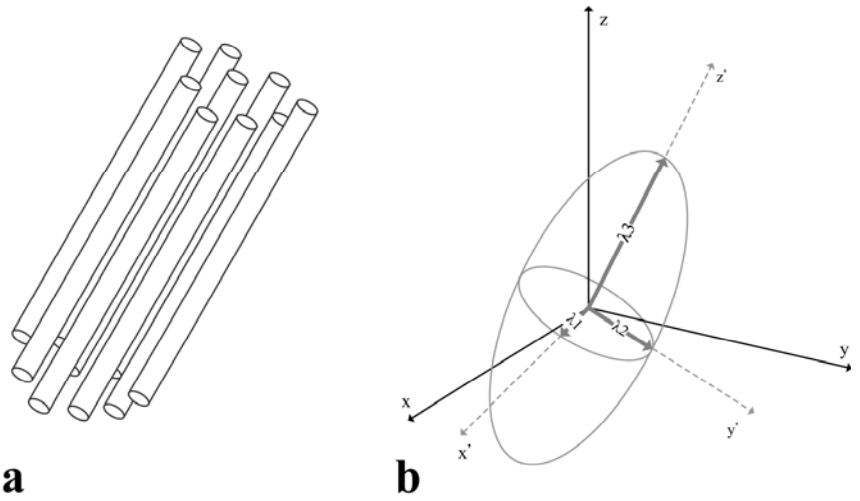

Figure 4.3: Illustration of (a) perfectly aligned axons, and (b) the corresponding diffusion ellipsoid with principle axes e_1, e_2, e_3 of length λ_1, λ_2, and λ_3, which are eigen-values and eigen-vectors of the diffusion tensor.

Based on the measured diffusion tensor $\overline{D}$, some quantitative measures of anisotropic diffusion are derived. The most commonly used parameters: mean diffusivity (mean apparent diffusion coefficient: mean ADC) and fractional anisotropy (FA) are introduced [54].

$$ADC_{mean} = \frac{1}{3}(\lambda_1 + \lambda_2 + \lambda_3) = \frac{1}{3}(D_{xx} + D_{yy} + D_{zz}) \tag{4.21}$$

This is a very useful formula, indicating that the calculation of mean ADC only requires measurements on physical axis: x, y and z. The diffusion tensor $\overline{D}$ can be separated into isotropic and anisotropic parts.

$$\overline{D} = \overline{D}_{iso} + \overline{D}_{aniso} \tag{4.22}$$

$$\text{where } \overline{D}_{iso} = \begin{bmatrix} ADC_{mean} & 0 & 0 \\ 0 & ADC_{mean} & 0 \\ 0 & 0 & ADC_{mean} \end{bmatrix}$$

$$\overline{D}_{aniso} = \overline{D} - \overline{D}_{iso}$$

The FA is defined as the fraction of anisotropic part of the diffusion tensor.

$$FA = \frac{\sqrt{\overline{\overline{D}}_{aniso} : \overline{\overline{D}}_{aniso}}}{\sqrt{\overline{\overline{D}} : \overline{\overline{D}}}} \tag{4.23}$$

$\sqrt{\overline{\overline{D}} : \overline{\overline{D}}}$ is a matrix dot product, defined as the magnitude of a tensor[54]. Figure 4.4 shows the ADC and FA maps of a healthy volunteer. The ADC values of gray matter and white matter are similar, but FA values of white matter are noticeably higher.

The diffusion tensor provides the information about 'macroscopic' anisotropy at a length of one image voxel, and is insufficient to distinguish between the microscopic anisotropy and microscopic isotropy, which both could end up with a low FA value [55]. Similarly, the crossing fiber in a voxel yields a low FA value, posing an issue with fiber tacking [56]. More refined, complete methods have been developed to solve these issues.

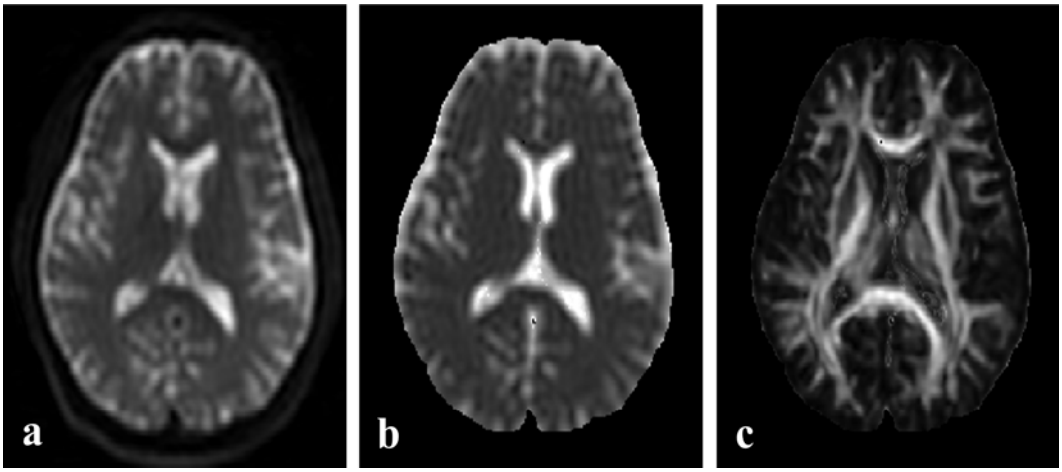

Figure 4.4: a: T_2 images (b = 0 s/mm^2), b: ADC map, and c: FA map. Imaging parameters: acquisition matrix of 64 × 64, NEX of 1, number of diffusion encoding directions of 25, and b-value of 1000 s/mm^2.

4.5 Data Acquisition

This section discusses the spatial encoding of the image following the preceding diffusion encoding gradients in a PGSE sequence. One inherent limitation of DWI is the longer T_E. The typical choice of b-value is 1000 s/mm^2 of clinical DWI, and the values of δ/Δ are approximately 21/27 ms for a PGSE sequence with gradient strength 40 mT/m. This infers that, for the same data acquisition, a DWI scan has a longer T_E than a T_2-weighted scan by 48 ms, resulting in low SNR and limited image resolution because of T_2 relaxation. To shorten T_E, one approach is to maximize the gradient strength and the rate of switching gradient (slew rate). However, these requirements of hardware induce eddy-current effects on diffusion and spatial encoding gradients, including gradient wave form distortions and inhomogeneous gradient magnetic fields. Another issue is that subject motion during the application of diffusion gradients. The applied diffusion gradients are able to sensitize the molecular movement of a

few microns. Meanwhile, only subtle, involuntary subject movements can cause undesired phase accrual, resulting in image artifacts and signal drop.

Various imaging strategies have been developed to address the issues of DWI data acquisition. The primary focus of this section is on echo planer imaging (EPI), which is the most commonly used method in clinical DWI.

4.5.1 Echo Planar Imaging DWI

The *k*-space sampling of EPI and the corresponding pulse sequence diagram are shown in Fig. 4.5. It is exactly the PGSE sequence, followed by a spatial encoding echo train. One major feature of EPI is its efficient *k*-space sampling, which minimize scan time and maximize SNR efficiency. Besides, in EPI, T_E is optimally shortened by using only a gradient-recalled echo train. *k*-space sampling in EPI is typically performed in one acquisition, or called single-shot EPI. There is a phase accrual following the diffusion gradients due to motion during the applied diffusion gradients or eddy currents that are generally referred as motion induced phase herein. This motion induced phase is inconsistent between different excitations. Thus, single-shot EPI is immune to this inconsistent motion induced phase. The short scan time and insensitivity to subject motion has enabled EPI as a clinical standard method. However, EPI method remains subject to various image artifacts arising from subject motion, off-resonance, and eddy currents.

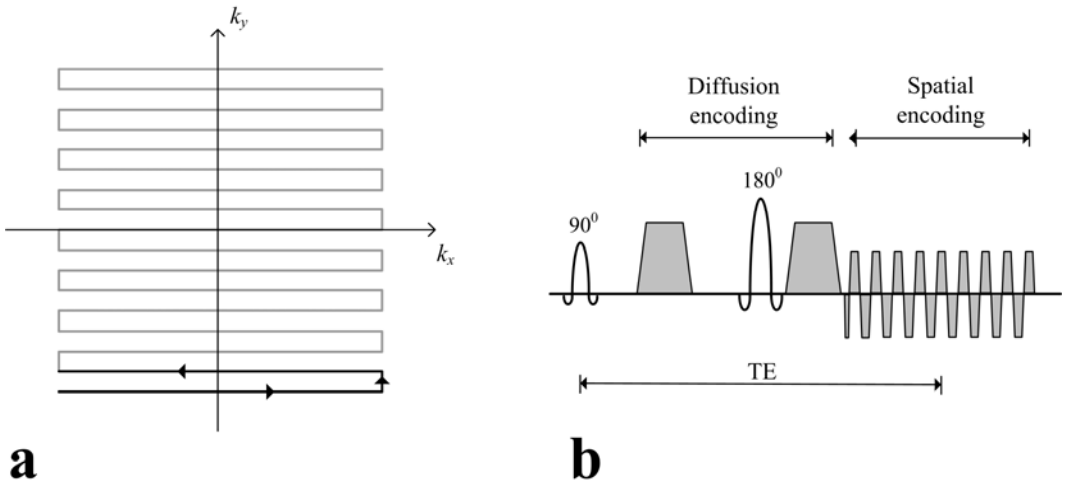

Figure 4.5: a: *k*-space trajectory and b: pulse sequence diagram of echo planar imaging. This is a simplified illustration using merely 17 phase-encoded lines. The data acquisition matrix is normally 128 × 128 or larger.

Motion induced artifact

The single-shot EPI method is immune to the inconsistent motion induce phase encountered by other multi-shot methods, but is subject to subject motion during the applied diffusion encoding gradients or during spatial encoding gradients. For simplicity, the discussion assumes only minor, rigid body motion. The effect of subject motion during the diffusion encoding gradients is more predominant, and would be the focus of the discussion.

A vector is defined to describe the change in location because of translation and rotation (Fig. 4.6).

$$\overline{R}(t) = \overline{x}(t) + \overline{\theta}(t) \times \overline{r} \tag{4.24}$$

The induce phase accrual is presented as:

$$\varphi = \gamma \int \overline{g}(t)\, \overline{R}(t) dt \tag{4.25}$$

The resulting effect is the constant phase offset and a shift in *k*-space:

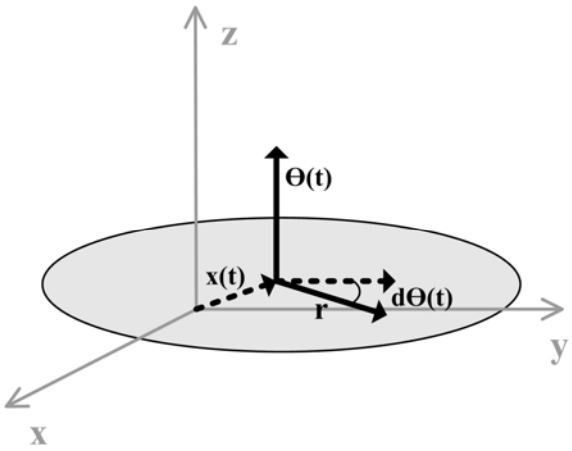

Figure 4.6: Illustration of rigid head motion, including translation and rotation; translation in x-y plane and rotation around z axis.

$$\varphi = \gamma \int \bar{g}(t) \cdot \bar{x}(t) dt + \gamma \int \bar{g}(t) \times \theta(t) dt \cdot \bar{r} \tag{4.26}$$

$$= \Theta + \Delta k \cdot \bar{r}$$

This effect of rigid motion is common to any diffusion acquisition. For the multi-shot methods, because the motion induced effects are different between the excitations, the problem of data inconsistencies cause image artifacts [57,58]. For single-shot method, such as EPI, although the motion effect remains, it can be minimized by simply removing the phase in image-space, including a constant phase and a linear phase ramp because of the shift in *k*-space.

Off-resonance related artifacts

The gradient-recalled echo train employed in EPI shortens the T_E and increases the efficiency of *k*-space sampling. However, it leads to the increased sensitivity to off-resonance from field inhomogeneity, magnetic susceptibility, and chemical shift. Assuming a perfect RF refocusing pulse of 180°, off-resonance phase accrual is related to the time away from the refocusing time point:

$$\varphi(t) = \int_0^t \Delta w dt' \tag{4.27}$$

The chemical shift of a fat nucleus is approximately 3.5 ppm, and the differences in resonance frequency between water and fat (Δw) is around 446 Hz at a 3 Tesla MR scanner. Given a receiver bandwidth of 125 KHz and echo time spacing of 1 ms for a EPI data matrix of 128 $\times$ 128, the bandwidth per pixel is around 977 Hz along readout direction and around 8 Hz along the phase-encoded direction, resulting in shifts of 0.5 pixel along readout direction and 56 pixels along phase-encoded direction. This narrow phase-encoding bandwidth prolongs the time of echo away from the refocusing time point, causing T_2^* signal decay and limiting the image resolution.

Other sources of off-resonance phase, including field inhomogeneity and magnetic susceptibility, can be spatially independent as well as dependent. Their induced phase errors can be approximated as a constant phase and a linear phase ramp in image domain, corresponding to a constant phase offset and a shift in *k*-space. The echo shifting along the direction of readout gradients alternates between odd and even echoes in EPI [59], leading to misregistration in *k*-space. In addition, the accumulation of the off-resonance phase error is different between each phase-encoded line. These factors make it very challenging to remove the phase error in EPI.

In a microscopic scale, which in a scale smaller than an image voxel, the off-resonance phase accrual creates microscopic phase dispersion, leading to a signal loss. This effect of T_2 shortening relaxation, referred as T_2^* signal loss, limiting the image resolution in EPI.

More recently, parallel imaging technique has been applied to increase the phase-encoding bandwidth. The phase-encoding bandwidth is increased by a factor of 2 or more depending on the applied acceleration factor [14], minimizing the effects of chemical shift and off-resonance related artifacts.

Eddy current induced artifacts

The oscillating readout gradients of EPI accelerate the sampling of *k*-space. The rapid change of magnetic flux generates electric field, called eddy current, which in turn distorts the originally planned gradient wave form and shifts the desired *k*-space sampling location primarily along the direction of readout gradients. The oscillating readout gradients thus induce the opposite shifts between even and odd echoes, causing misregistration in *k*-space. Other hardware-driven system delays have similar effects as described above.

The *k*-space misregistration between even and odd echoes in EPI is generally referred as N/2 ghosting. The image artifacts due to the constant phase φ or *k*-space shift along the frequency-encoded direction $u\Delta k_x$ alternating between odd and even echoes can be represented analytically [60].

$$m'(x, y) = m(x, y)\cos\varphi + i\, m(x, y - \frac{N_y}{2})\sin\varphi \tag{4.28}$$

$$m'(x, y) = m(x, y)\cos(\frac{2\pi\pi u}{N_x}) + i\, m(x, y - \frac{N_y}{2})\sin(\frac{2\pi\pi u}{N_x}) \tag{4.29}$$

Both show a ghosting artifacts coming from a shift of signal intensity at $N_y/2$, where N_y is the size of data matrix along the phase-encoded direction, and a modulation of image amplitude.

N/2 ghosting in EPI is normally corrected using the reference scan method [61]. This method requires an additional data acquisition, where each gradient echo is acquired in two opposite readout directions without phase encoding. If there is a positive echo shift associated with the gradient echo, then the negative echo shift is associated with the gradient echo of the opposite readout direction (Fig. 4.7a). By reversing the gradient echo with negative echo shift, the relative echo shift between two gradient echoes is two times the echo shift (Fig. 4.7b). The estimate of echo shift as well as constant phase offset can be calculated by comparing two echoes. The reference scan is acquired for each gradient echo in EPI and the estimate of echo shift and constant phase offset are used to 'un-shift' and remove the phase offset of every gradient echo.

In the reference scan method, the phase error is assumed to exist only in the frequency-encoded direction by turning off the phase encoding for all reference data. This assumption may no longer hold as the off-resonance induced echo shift is present along the phase-encoded direction [59].

Another issue associated with the rapid gradient switching is peripheral nerve stimulation (PNS). The PNS level has been found to be proportional to the change of magnetic field: dB/dt, which is related to the rise time and magnetic gradient strength [62]. No study has found that the PNS level lead to the risk in cardiac and respiratory function. However, caution should be taken as the advancement of MR hardware.

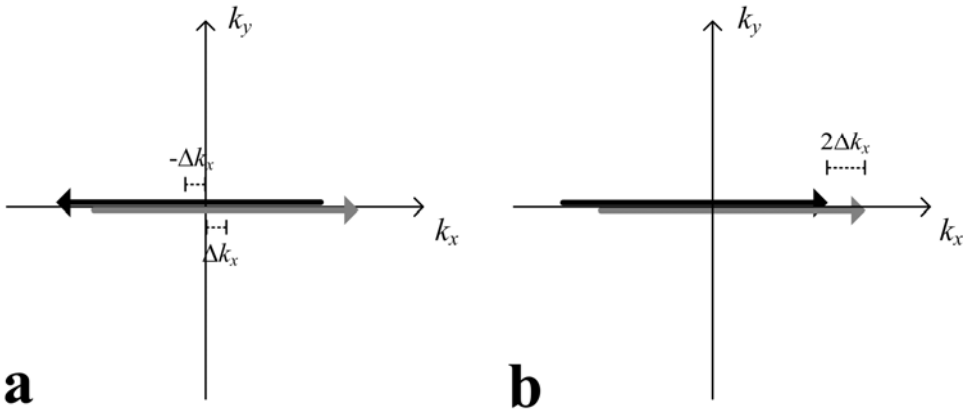

Figure 4.7: Illustration of reference scan method. a: The gradient echoes are acquired in two opposite directions without phase encoding, and their echo shifts have opposite signs. b: By reversing one of the gradient echo of the negative readout direction, the relative shift between two gradient echoes is two times the echo shift.

4.5.2 PROPELLER DWI

PROPELLER (Periodically Rotated Overlapping Parallel Lines with Enhanced Reconstruction) [15] is another alternative method for DWI. In contrast to EPI, where squared *k*-space coverage is finished in one TR, PROPELLER encodes a *k*-space strip in one T_R and other rotated strips in subsequent T_Rs to fill a circle of *k*-space (Fig. 4.8a). In addition, each *k*-space strip is encoded by a fast spin echo train, where each phase-encoded line is a spin echo between each pair of refocusing RF pulses.

The radial nature of data acquisition in PROPELLER make the high resolution diffusion-weighted images achievable, which are normally limited by the T_2 or T_2^* relaxation in the phase-encoded direction. The use of fast spin echo train minimizes the off-resonance phase warping in the phase-encoded direction.

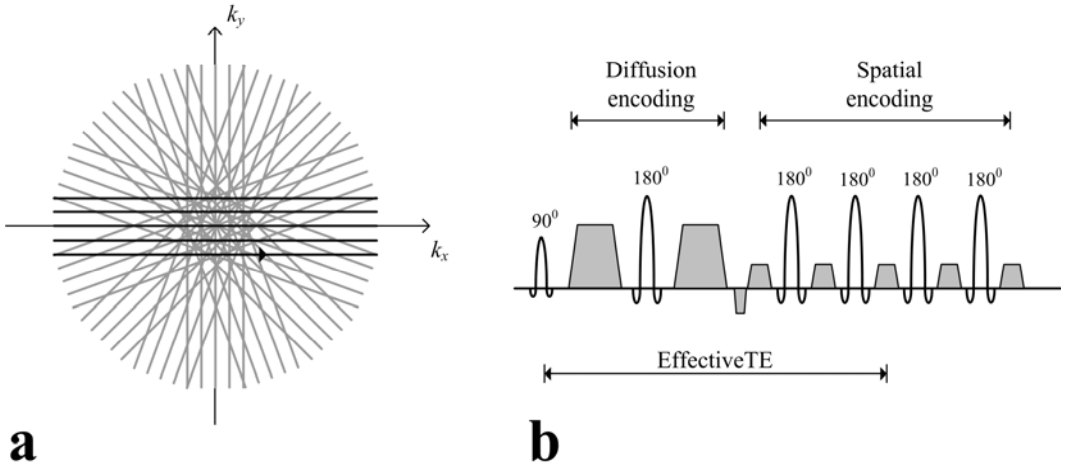

Figure 4.8: a: *k*-space trajectory of diffusion-weighted PROPELLER. The bold lines denote encoded PROPELLER 'blade' in one T_R. b: Pulse sequence diagram of diffusion-weighted PROPELLER in one T_R. The effective T_E is defined as the time reaching the center of *k*-space. Illustrations are for the echo train length of 5.

The overlapped region serves as a self-navigated region for the motion-induced phase, which is to be removed before combining all the data blades to form the final image. The motion induced phase is assumed to be slowly varying in space. Besides, this method requires less demanding hardware for switching gradients, reducing the artifacts due to system imperfections. Nonetheless, PROPELLER method is subject to the issues from high specific absorption rate (SAR), long scan time, non-Carr-Purcell-Meiboom-Gill (non-CPMG) echo train, and motion-induced phase, which to be discussed below.

SAR Issue

SAR, in a unit of watts per kilogram (W/kg), is a quantitative measure of RF energy deposited into the patient. The increase in SAR causes patient heating, which may pose the health risk. A scaling relationship between the main field

strength (B_0), flip angle (θ), and RF bandwidth (Δf) is given by:

$$SAR \propto B_0^2 \theta^2 \Delta f \tag{4.30}$$

Compared with EPI (Fig. 4.5), higher SAR is generated in PROPELLER by requiring more refocusing RF pulses of 180° flip angle, and the problem is even exacerbated at the high field strength; 3T generates 4 times SAR than 1.5T. According to the regulatory guideline for SAR by International Electro technical Commission (IEC) and the Food and Drug Administration (FDA), SAR value must be less than 8 W/kg over 15 minutes and less than 4 W/kg over 5 minutes.

Non-CPMG Echo Train

The perfect 180° refocusing RF pulses of a fast spin echo train (Fig. 4.8b) ensure the stable signals with no dephasing from the off-resonance phase. However, the prefect refocusing is difficult to achieve in reality because of B_1 field inhomogeneity. When the flip angle is smaller than 180°, the transverse magnetization is partially delivered to the longitudinal magnetization after the fist refocusing RF pulse, and at the subsequent refocusing RF pulses, the multiple echoes are generated from multiple signal pathways [63]. Those multiple echoes are associated with different phases, resulting in signal losses throughout the refocusing echo train. The CPMG echo train [64] was developed to minimize the signal loss for an echo train with non-180° refocusing RF pulses. This requires two conditions, called CPMG conditions. First, there must be a 90° phase difference between the excitation and refocusing RF pulses. Besides, the time spacing between each pair of refocusing RF pulses has to be uniform throughout

an echo train, such that the echo is formed in the mid-point between each pair of refocusing RF pulses. Second, the gradient area between each pair of refocusing RF pulses has to be identical throughout an echo train.

A simulation was performed to investigate the spin phase evolution during a refocusing echo train [15]. A refocusing echo train satisfying the CPMG condition (90° phase shift between excitation and refocusing RF pulses) has a greater immunity over the signal losses due to the non-180° flip angle (Fig. 4.9). Lower flip angle allowed in a CPMG echo train also lead to a reduction in SAR (Eq. 4.30). The required 90° phase difference between excitation and refocusing RF pulses ensures the transverse magnetization after the 90° excitation pulse lies along the axis of the refocusing RF pulse (Fig. 4.10a). However, in diffusion-weighted sequences (Fig. 4.8b), the preceding diffusion encoding gradients produce a unknown, spatially varying phase because of subject motion (Eq. 4.26), shifting the transverse magnetization away from the axis of the refocusing RF pulse (Fig. 4.10b). The resulting out-of-phase component of the transverse magnetization is sensitive to non-180° refocusing RF pulses [65], causing an overall signal loss (Fig. 4.11a). MLEV sequence [66] was applied to reduce this effect using alternating refocusing RF pulses (Fig. 4.11b). However, the out-of-phase component of transverse magnetization (Fig. 4.10b) still oscillates between odd and even echoes. This phase shift is termed as motion induced phase herein. The alternating motion induced phase between odd and even echoes causes phase inconsistencies in a PROPELLER blade. The phase inconsistencies can be minimized by conjugating the motion induced phase of odd echoes in image domain to match the motion induced phase of even echoes [15].

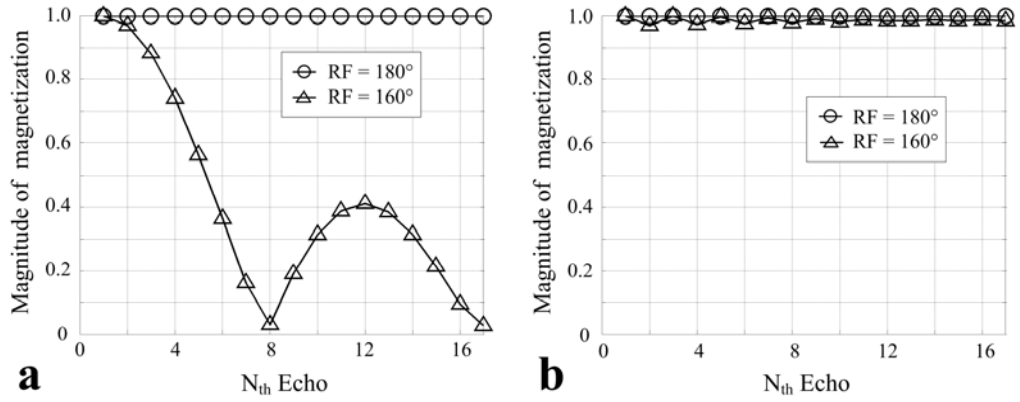

Figure 4.9: Magnitude of transverse magnetization of echoes throughout a refocusing echo train with refocusing RF pulse of 180° and 160°; a: no phase difference and b: 90° phase difference between excitation and refocusing RF pulses.

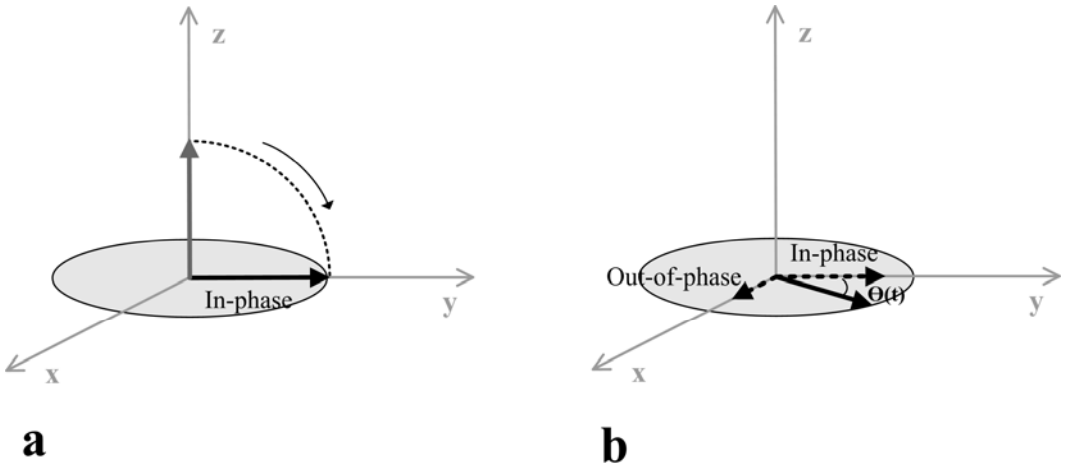

Figure 4.10: a: The change of magnetization after a 90° excitation RF pulse applied along x axis. b: The phase modulation (Θ(t)) deviates the magnetization from y axis, creating a out-of-phase component.

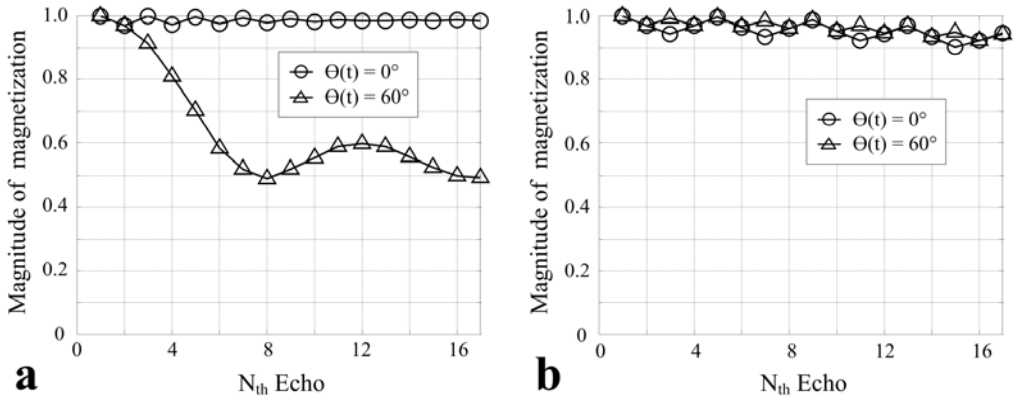

Figure 4.11: Magnitude of transverse magnetization of echoes throughout a refocusing echo train with refocusing RF pulse of 160° with a phase shift of 0° and 60°. a: Echo train with excitation RF pulse of 90° x and subsequent refocusing RF pulses of 160° y. b: Echo train with excitation RF pulse of 90° x and subsequent alternating refocusing RF pulses of 160° x, 160° y.

Motion Induced Phase Removal

The motion induced phases are different between data blades from different T_{RS}, and need to be removed prior to the combination of data blades to form the final image. By assuming that the motion induced phase is slowly varying in space, the overlapping area of PROPELLER blades (Fig. 4.8a) becomes the navigated region of the motion induce phase. If the motion induced phase is consistent between odd and even echoes, the phase map of the motion induced phase can be created through Fourier transform of the data blade. However, the short blade width of a data blade results in Gibbs ringing phase along the phase-encoded direction. The Gibbs ringing phase should be kept during the image reconstruction to avoid the blurring effects on the final reconstructed image. Therefore, a pyramid function is applied to the data blade to 'filter' out the Gibbs ringing for creating a motion induced phase map [15].

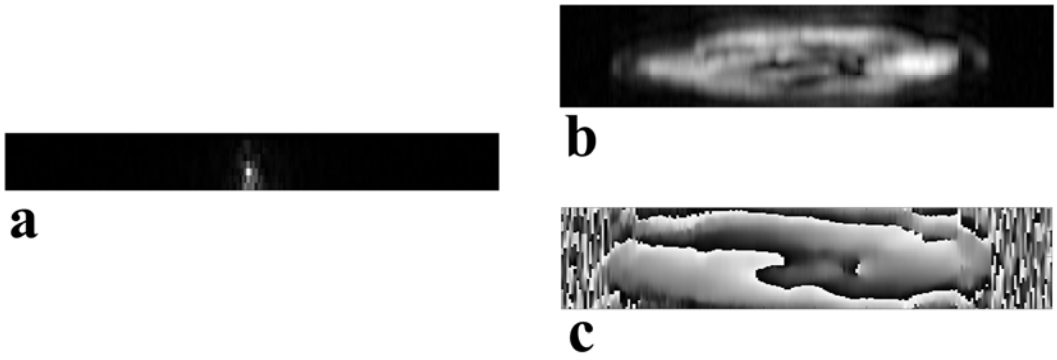

Figure 4.12: Magnitude of one PROPELLER data blade (a) with diffusion weighting b = 1000 s/mm^2 at y axis, and its corresponding phase map: magnitude images (b), and phase maps (c).

Those approximations are problematic for a data blade with a narrow blade width. The rapid varying phase in space can possibly shift the majority of *k*-space data out of the data blade (Fig. 4.12). In addition, the spatial variation of Gibbs ringing phase is slower at the short blade width. The applied pyramid function could no longer filter out the Gibbs ringing phase, which can be removed together with the motion induced phase (Fig. 4.12b-c).

Chapter 5

NON-MONOEXPONENTIAL PHENOMENOLOGIAL MODELS

When b-value is larger than 2000 s/mm^2, the diffusion-weighted signal decay has been observed to deviate from a monoexponential behavior in the brain. This deviation at higher b-values could potentially provide valuable information about pathological mechanisms [67-73]. Recent works have been dedicated to establish the relationship between the signal decay and tissue microstructure. In general, the approaches can be divided into two categories: analytical models and phenomenological models.

Analytical models [30,74-77] give the complete description of tissue structure, and the model parameters are direct measure of physical quantities. The models have multiple parameters and normally impose the assumption of short gradient pulse (SGP) ($\delta \rightarrow 0$) or assumptions about geometry of microstructure. However, it is difficult to achieve the SGP condition in current human imaging systems because of limited field gradient strengths. Besides, real tissues are composed of complex microstructure and biophysical mechanisms, which are difficult to describe using certain geometry even with multiple model parameters.

Phenomenological modeling is developed to describe the observed non-monoexponential decay. It has a few fitted parameters and makes no assumption about tissue microstructure.

Diffusion-weighted MR measurements have an inherently low SNR, because of a long T_E and an application with diffusion encoding gradients. At higher b-values, further SNR loss is caused by a longer T_E and an increased

diffusion-weighting. More number of excitations (NEX) is thus necessary to increase SNR. This combined with multiple b-value measurements prolongs the scan time for the high-value experiments. Long scan time is a very important limiting factor, because it poses concerns over patient discomfort and safety. Longer scan time also makes MR imaging more susceptible to patient motion. In this respect, phenomenological models with only a few parameters are applicable in a clinical setting. The major issue with phenomenological models is their lack of the relationship with tissue structures.

The objective of this work was to study the behaviors of two phenomenological models: the statistical distribution and the diffusion kurtosis models. For this purpose, we acquired DWI data from clinical cases of ischemic stroke and recurrent high-grade gliomas to study how the phenomenological diffusion models responded to the pathological changes. In addition, we developed a Monte Carlo simulation of microstructures and a PGSE experiments to investigate how the fitted parameters were related to microstructural changes. If each of the diffusion models exhibits different, specific sensitivity to microstructural changes, the models may be used together to better understand and identify the underlying biophysical mechanisms.

5.1 Background

5.1.1 Multi-exponential Models

The exponential relaxation is a common phenomenon in physics and chemistry. The non-monoexponential relaxation is empirically attributed to the summation of multiple relaxations from heterogeneous sources [78]. For a cell

structure with intra/extra-cellular compartments (Fig. 2.3), it is tempting to envisage the slow and fast diffusion components arising from intra- and extra-cellular compartments with fractions: $f_{slow} + f_{fast} = 1$.

$$\frac{S(b)}{S(0)} = f_{slow}\exp(-b \times ADC_{slow}) + f_{fast}\exp(-b \times ADC_{fast}) \quad (5.1)$$

The bi-exponential model with three fitted parameters has been shown to fit the data well and correlate with the pathological changes [72,73,79]. However, the measured fractions of slow/fast diffusion components (0.20-0.33/0.67-0.80) are inconsistent with the known intra/extra-cellular fractions (0.80/0.20) [80]. In addition, the bi-exponential decay has been observed at the intracellular space [81] and at the cellular space with the disintegrated cell membrane [82]. It can also be over-parameterized in some cases [83].

In complex tissue structure, it is likely that the signal attenuation observed with DWI can arise from a continuous distribution of diffusion rates [10,11,84]:

$$\frac{S(b)}{S(0)} = \int_0^\infty P(ADC)\exp(-b \times ADC)dADC \quad (5.2)$$

P(ADC) is the continuous PDF of apparent diffusion rates without the assumption about the number of diffusion rates or short gradient pulse condition. Calculation of P(ADC) through Eq. (4.2) is a numerically ill-posed problem [84,85].

Many relaxation problems in physics and chemistry are formulated as multiple relaxation sources arising from heterogeneous mediums that are similar to Eq. (4.2). The signal relaxation can be empirically described by the Kohlrausch-Williams-Watts (KWW) function [86]. The application of KWW function to diffusion-weighted signal attenuation was first presented by Bennett et al. [11], called the stretched exponential model (α-DWI):

$$\frac{S(b)}{S(0)} = \exp(-b \times DDC)^{\alpha} \tag{5.3}$$

DDC is described as the distributed diffusion coefficient, and α is termed as "heterogeneity index". The α-DWI model has been used to measure structural heterogeneity in the brain [11,71,87,88] with a high b-value: 4000-5000 s/mm^2. It has been linked to fractal tissue microstructure [89,90].

The α-DWI model makes no assumption about the type of the distribution P(ADC). Alternatively, other statistical distribution model assumes P(ADC) as a truncated Gaussian distribution [10]:

$$\frac{S(b)}{S(0)} = \exp(-b \times D_{stat} + \frac{1}{2} b^2 \times \sigma_{stat}^2) \tag{5.4}$$

D_{stat} refers to the most probable apparent diffusion rates, and σ_{stat} is the width of P(ADC). Another choice of P(ADC) is a gamma distribution [13].

$$\frac{S(b)}{S(0)} = \frac{\beta^{\alpha}}{(\beta^{\alpha} + b)^{\alpha}} \tag{5.5}$$

where $\alpha = (D_{gamma}/\sigma_{gamma})^2$, $\beta = D_{gamma}/(\sigma_{gamma})^2$, D_{gamma} is the mean diffusion rate and σ_{gamma} is the standard deviation (STD) of P(ADC).

5.1.2 Cumulant Expansion Model

Instead of making an assumption about the multiplicity of water diffusion rates as in the multi-exponential models, the diffusion kurtosis imaging (DKI) model measures the deviation of water displacement PDF from a Gaussian distribution. The DKI model was derived from a Taylor expansion of signal attenuation in the q-space model (Eq. (4.15)).

$$E(q,\Delta) = \int P(R)(1 + iqR - \frac{1}{2}(qR)^2 + \frac{1}{6}(qR)^3 - \frac{1}{24}(qR)^4 + ...)dR \tag{5.6}$$

The cumulant expansion of Eq. (5.6):

$$\log E(q,\Delta) = -q^2 \Delta D + \frac{1}{6} q^4 \Delta^2 D^2 \times \text{kurtosis} + \ldots \quad (5.7)$$

The kurtosis is defined as:

$$\text{kurtosis} = \frac{E[R^4]}{E[R^2]} - 3 \quad (5.8)$$

The kurtosis can also be related to distribution of apparent diffusion rates (Eq. (5.2)) as:

$$\text{kurtosis} = \frac{3\,\text{var}[ADC]}{(E[ADC])^2} \quad (5.9)$$

If the short gradient pulse approximation is applied ($\delta \rightarrow 0$), and only the first two terms in the cumulant expansion (Eq. (3.16) are kept, the DKI model can be represented as a truncated cumulant expansion:

$$\log E(b) = -bD_{app} + \frac{1}{6} b^2 D_{app}{}^2 \times K_{app} \quad (5.10)$$

D_{app} and K_{app} refer to apparent diffusion coefficient and apparent kurtosis.

The DKI model has a well-defined theoretical basis. However, the truncated representation in Eq. (5.10) is only valid when both the b-value (q-vector) and the high moment of displacement R are small [91]. The b-value for the DKI model is less than 2500 s/mm^2 in human brains. In addition, the derivation of the DKI model still requires the short gradient pulse approximation ($\delta \rightarrow 0$). In light of the above limiting factors, the DKI model is considered as a phenomenological model [74,91].

5.1.3 Summary

The statistical distribution and the DKI models quantify non-Gaussian water diffusion with a relatively low b-value of less than 2500 s/mm^2, and these models can thus be implemented in the clinic with a reasonable scan time and an adequate

SNR. The models have been used to study biophysical and pathological changes [70,92-97], potentially exhibiting higher sensitivity and specificity compared to the ADC of the monoexponential model. However, the relation between these models of non-Gaussian water diffusion and tissue microstructure is still unclear.

To gain a better understanding of how these models related to healthy and diseased tissue, we investigated the relationship between two non-Gaussian water diffusion models (the statistical distribution and DKI models) and a simulated tissue microstructure. For this purpose, we performed a clinical study on ischemic stroke (n = 5) and recurrent gliomas (n = 7) to study how the fitted parameters correlated with pathological changes. We implemented multiple b-value imaging protocols with maxim b = 2500 s/mm^2 in the clinics, and correlated the fitted parameters with the defined ROIs. We also created a 2-D Monte Carlo simulation of the DWI experiment and water diffusion in an intra/extra-cellular microstructure with the continuously distributed compartmental size. We independently varied three relevant microstructural parameters: cell size, volume fraction, and membrane permeability to study how the fitted parameters (D_{stat}, σ_{stat} of the statistical distribution model, D_{app}, K_{app} of the DKI model) correlated with the microstructural changes compared with the ADC. We compared the relative sensitivity between the diffusion models to the changes, and studied the dependence of the models on a realistic SNR. If each of the diffusion models exhibits different, specific sensitivity to microstructural changes, the models may be used together to better understand and identify the underlying biophysical mechanisms.

5.2 Patient Study

An imaging protocol of b-value up to 2500 s/mm^2 was implemented in a clinical scanner, and DWI images were acquired from five case of ischemic stroke (n = 5) and seven cases of recurrent high-grade gliomas (n = 7). The statistical distribution and DKI models were fitted the signal decay, and their fitted parameters were compared between the defined regions of interest (ROIs). The goal was to study how the fitted parameters of the non-monoexponential models correlated with the pathological changes.

5.2.1 Experiment

With the Institutional Review Board approval and informed consent obtained from each patient, 12 patients were included in this study. Five patients (2 females, 3 males with age: 57 ± 14 years, range: 42-77 years) were with ischemic stroke within 7 to 14 days after the onset of the neurological deficit. Seven patients were with recurrent WHO grade IV gliomas (5 females, 2 males with age: 56 ± 13 years, range: 42-74 years), and had undergone previous multimodality therapy, including chemotherapy and radiation. Pre-operative imaging was obtained and was correlated with stereotactic sampled histopathology, which showed to have recurrent tumor. Patients with tissue samples containing both tumor and post-treatment radiation effects were considered as tumor cases if one of the biopsy samples was tumor.

Images were acquired on a GE Signa HDx 3T scanner with an eight-channel head coil. A dual spin echo DW echo planar imaging (EPI) sequence was used with the maximum gradient strength: 40 mT/m. DW images were acquired in

three directions: x, y, and z respectively with b-value: 0-2500 s/mm^2 in increment of 500 s/mm^2 by changing the gradient strength g. The SENSE factor was 2. Other imaging parameters were: acquisition matrix of 128 × 128, field of view of 240 mm, slice thickness of 4.5 mm with 0.5 mm gap, number of excitations (NEX) of 4, δ/Δ = 29/36 ms, and T_E/T_R = 106/4000 ms. For patients with recurrent tumor, routine pre- and post-contrast axial T_1-weighted 3D magnetization prepared rapid gradient echo (MPRAGE) images were acquired with whole brain coverage from each patient.

5.2.2 Data Analysis

Data of diffusion attenuation were fitted with the statistical distribution and DKI models using the Levenberg-Marquardt algorithm in MATLAB (Mathworks, Inc.). For comparison, the ADC of the monoexponential model was calculated using the DWI signals of b = 0 and 1000 s/mm^2. DW attenuation was normalized by the signal of b = 0 s/mm^2, and the fitted parameters obtained from x, y, and z diffusion gradient directions were averaged to yield a mean value for each image voxel. The noise floor was empirically determined to be the mean plus 3 times STD of background noise. The DWI signals below the noise floor were excluded from the data fitting. The goodness-of-fit was assessed using the reduced chi-square statistic (χ_ν^2) [98], defined as the sum of squares of residuals divided by the uncertainty of measurements (σ_i) and the degree of freedom ($\nu = N - 1 - n$; n is the number of free parameters):

$$\chi_\nu^2 = \frac{1}{\nu}\sum_{i=1}^{N}\frac{(S_i - S_{fit})^2}{\sigma_i^2} \tag{5.11}$$

The uncertainty of measurements (σ_i) was empirically determined to be 3 times

STD of background noise. The goodness-of-fit was also assessed using the coefficient of determination (R^2). The data fits with a low R^2 (< 0.95) were excluded from the data analysis.

In the cases of ischemic stroke, two ROIs were selected: brain lesion and brain white matter. The regions of brain lesion were placed on the area of hyper-intensity of diffusion-weighted images with b = 1000 s/mm^2 (Fig. 5.1a). The regions of white matter were segmented on T_2-weighed images (Fig. 5.1b) using SPM (University College London, UK). In the cases of recurrent tumor, three ROIs were defined (Fig. 5.3): enhancing regions on T_1-weighted post-contrast images, peri-enhancing regions on T_2-weighted images (b = 0 s/mm^2), defined as abnormal signals outside of enhancing regions, and white matter regions, which were segmented on T2-weighed images using SPM. An paired two-tailed Student's t-test was used to compare the fitted parameters between the selected ROIs. The difference was considered to be statistically significant, if $p < 0.05$.

5.2.3 Results

An example of calculated parametric maps of a case of ischemic stroke is shown in Fig. 5.1. The fitted parameters in ROIs of five patients with ischemic stroke are shown in Fig. 5.2. Brain lesion ROI showed the smaller average ADC, D_{stat}, D_{app}, and σ_{stat}, and larger average K_{app} than white matter ROI (Fig. 5.3).

Figure 5.4 illustrates an example of calculated parametric maps of a case of recurrent gliomas. The fitted parameters in ROIs of seven patients with recurrent gliomas are shown in Fig. 5.5. Enhancing ROI showed higher average ADC, D_{stat},

D_{app}, and σ_{stat}, and smaller average K_{app}, compared with white matter ROI (Fig. 5.6). Compared with peri-enhancing ROI, enhancing ROI showed smaller average ADC, D_{stat}, and D_{app}, while there was no difference between enhancing and peri-enhancing ROIs in σ_{stat} and K_{app}.

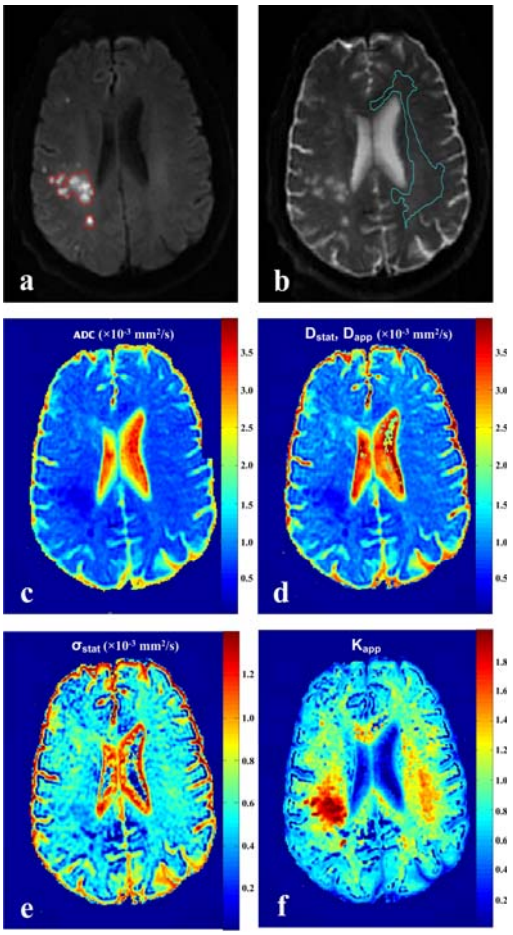

Figure 5.1: Example of ROIs selection and parametric maps of a 63-year-old male with ischemic stroke. a: Isotropically diffusion-weighted image (b = 1000 s/mm^2) with ROIs of brain lesions. b: T_2-weighted (b = 0 s/mm^2) image with ROI of white matter. c-f: Parametric maps calculated by fitting the diffusion models to the DWI signals of b = 0 – 2500 s/mm^2; ADC of monoexponential model, D_{stat}, σ_{stat} of the statistical distribution model, and D_{app}, K_{app} of the DKI model.

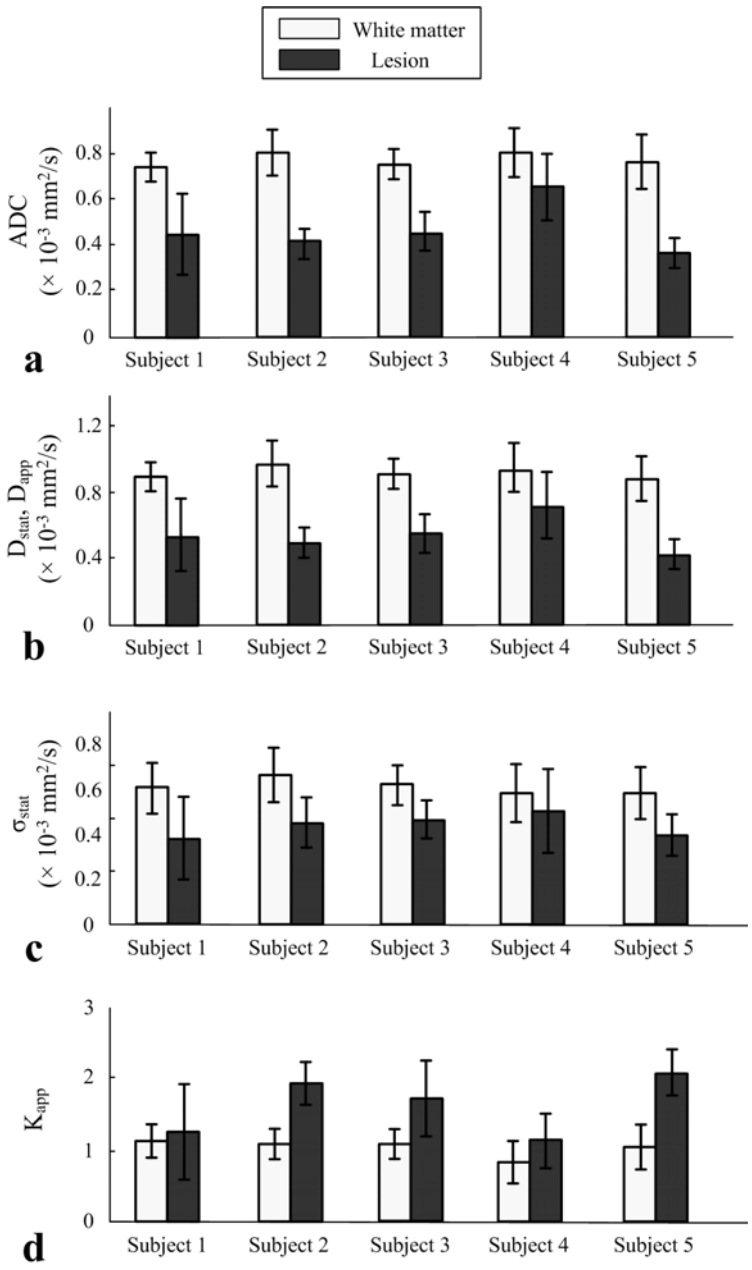

Figure 5.2: The fitted parameters within the ROIs of white matter and brain lesions of five clinical cases of ischemic stroke; ADC of monoexponential model, D_{stat}, σ_{stat} of the statistical distribution model, and D_{app}, K_{app} of the DKI model. Error bar denotes the standard deviation.

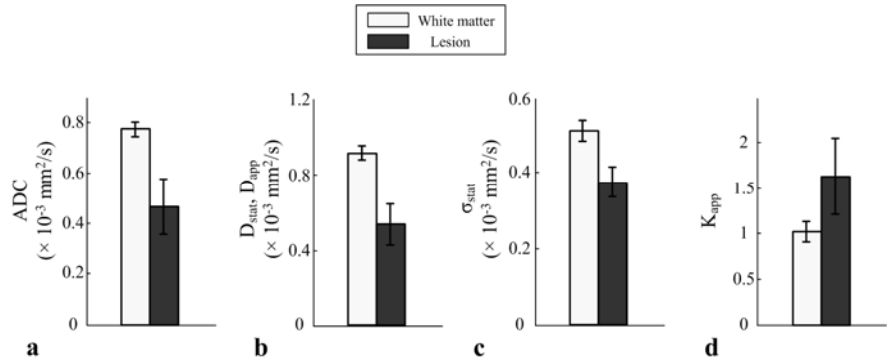

Figure 5.3: The fitted parameters within the ROIs of white matter and brain lesions averaged across five clinical cases of ischemic stroke; ADC of monoexponential model, D_{stat}, σ_{stat} of the statistical distribution model, and D_{app}, K_{app} of the DKI model. Error bar denotes the standard deviation.

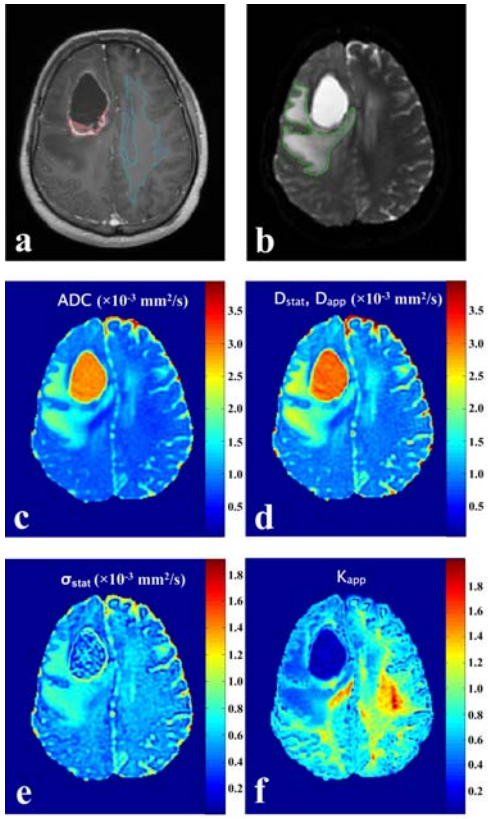

Figure 5.4: Example of ROIs selection and parametric maps of a 46-year-old male with recurrent glioblastoma. a: Post-contrast T_1-weighted image with enhancing and white matter ROIs. b: T_2-weighted (b = 0 s/mm^2) image with peri-enhancing ROI. c-f: Parametric maps calculated by fitting the diffusion models to the DWI signals of b = 0 – 2500 s/mm^2; ADC of monoexponential model, D_{stat}, σ_{stat} of the statistical distribution model, and D_{app}, K_{app} of the DKI model.

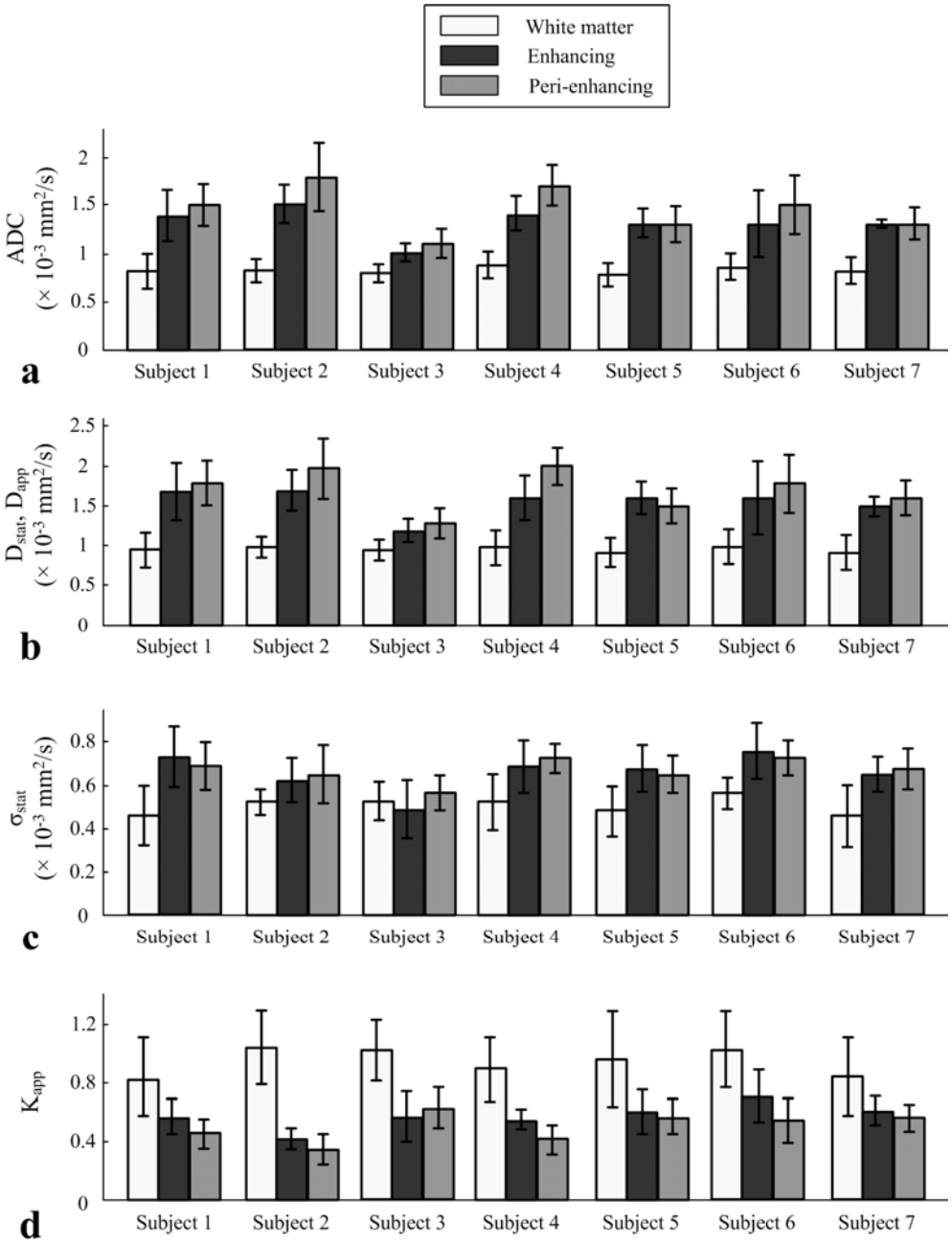

Figure 5.5: The fitted parameters within the ROIs of white matte, enhancing, and peri-enhancing of seven clinical cases of recurrent gliomas; ADC of monoexponential model, D_{stat}, σ_{stat} of the statistical distribution model, and D_{app}, K_{app} of the DKI model. Error bar denotes the standard deviation.

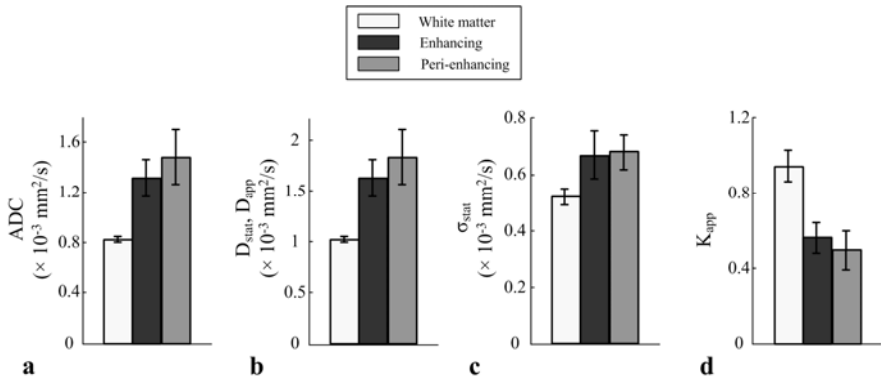

Figure 5.6: The fitted parameters within the ROIs of white matter enhancing, and peri-enhancing averaged across seven clinical cases of recurrent gliomas; ADC of monoexponential model, D_{stat}, σ_{stat} of the statistical distribution model, and D_{app}, K_{app} of the DKI model. Error bar denotes the standard deviation.

5.2.4 Discussion

Our findings of the decreased diffusivity measured by ADC, D_{stat}, and D_{app}, and the increased index of non-Gaussian water diffusion by K_{app} on ischemic lesion were consistent with a previous study on human ischemic stroke using the DKI model [99,100]. In our experiments, the ROI of recurrent tumor showed a decrease in the K_{app} compared with white matter ROI. This result is consistent with the study by Raab et al. [70] on high-grade brain tumor using the DKI models.

Although the measured diffusivity by ADC, D_{stat}, and D_{app} showed differences between enhancing and peri-enhancing ROIs, there were overlaps of the fitted parameters between these two ROIs. These overlaps of the fitted parameters may be due to the highly infiltrative nature of malignant tumor cells [101] and treatment-induced necrosis in the enhancing and peri-enhancing ROIs.

There are several challenges for a ROI-based study of high-grade brain tumor. Most studies including this work define a ROI on the enhancing regions on

T_1-weighted post-contrast images by assuming that modulated cellularity of tumor cells correlates with the enhancing regions on T_1-weighted images. This assumption could be problematic [101]. In addition, the changes in tumor cellularity could be subtle and occurs with surrounding necrotic tissues, and thus may be difficult to detect using low-resolution, diffusion-weighted images.

5.3 Monte Carlo Simulation

Unlike the analytical methods, which require assumptions of certain geometrical structures, short gradient pulse approximation (SGP condition: $\delta \rightarrow 0$), or long time limit ($\Delta \rightarrow \infty$), the Monte Carlo method allows flexibility to approximate realistic DWI experiments and tissue microstructure. It has been used to study the relationship between the physical structures and the phenomenological models, including ADC and DKI models. However, either compartmental exchange is unconsidered in some of the studies [102,103], or the simulated structures composed of uniform cell location or cell size [30,104].

In this study, we simulated molecular water diffusion in a microstructure composed of randomly located semi-permeable cells with a continuously distributed cell size. We also simulated a PGSE experiment with a typical gradient strength (40 mT/m) in human imaging systems.

5.3.1 Methods

To simulate the MRI signal arising from tissue, a Monte-Carlo simulation was implemented in C++. 60,000 dimensionless spins were randomly placed in a 2-D plane of 0.4×0.4 mm^2 and performed a random walk at a rate 40,000 steps/second within and between randomly packed cells (Fig. 5.7). The

intracellular diffusivities was set to 1.0×10^{-3} mm^2/s [30], and the extracellular diffusivity was set to be 2.5×10^{-3} mm^2/s [30], assuming that the intrinsic extracellular diffusivity is faster than the intracellular diffusivity. Cell sizes were specified from a gamma distribution with a mean of 10 μm, a typical human cell size [105], and a standard deviation (SD) of 7 μm in diameter; the ratio SD/mean was set to 0.7 to match the axon size distribution in human corpus callosum [102,106]. The intracellular volume fraction was 0.65, which is within the range of measured values in rat brains (0.73 in gray matter, 0.60 in white matter) [48]. The membrane permeability defined in [31] was 0.01 mm/s, close to the measured values in various cell types [75].

In this study, three important parameters of tissue microstructure were investigated: cell size (2R), cell volume fraction (V), and membrane permeability (P) that have been shown to correlate with pathology. An increase in cell size (around 1-6 μm increase in nuclear size) was observed in tumor cells after treatment in a mouse model of colon cancer [107]. An increase in cell volume fraction by 0.15 was shown after ischemia in rat brains [108], while a decrease of cell volume fraction by 0.19 was found in human glioblastoma [109]. Decreased membrane permeability was suggested as one of the mechanisms for ischemia [47]. An increase in membrane permeability by a factor of around 3 to 7 was shown in brain tumors [110].

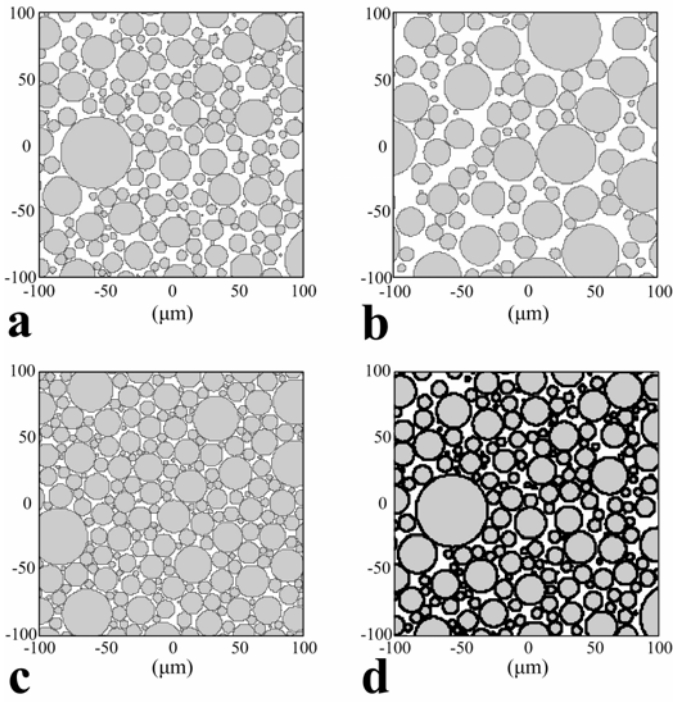

Figure 5.7: Illustration of the simulated cell structure (a) with mean cell size: 10 μm in diameter and cell volume fraction: 0.65, and the microstructural changes in mean cell size (increased to 15 μm) (b), cell volume fraction (increased to 0.80) (c), and membrane permeability (decreased) (d). All the changes (b-d) were made with other microstructural parameters kept the same as in a. Intra/extra-cellular space is shown in gray/white color.

To study how the non-Gaussian water diffusion models respond to pathology-induced microstructural chagnes, three parameters were modified in separate experiments, including a decrease and an increase in mean cell size (5-10-15 μm), cell volume fraction (0.50-0.65-0.80), and membrane permeability (0.001-0.01-0.1 mm/s). Figure 5.7 illustrates how the simulated microstructure was changed.

A PGSE sequence was simulated to create the DWI signal through spin phase accumulation [30, 102]. The parameters of the PGSE sequence were chosen to be similar to those of human MRI systems: the maximum gradient strength 40

mT/m and δ/Δ = 29/36 ms. The gradient was applied along a single axis with maximum b-value: 2500 s/mm^2 in increments of 500 s/mm^2 by changing the gradient strength g. Each experiment was repeated 20 times, and the simulated DWI signals were averaged across the repeated experiments to minimize the deviation from the Monte Carlo simulation; the SD of the simulated DWI signal ~ 3×10^{-3}.

The simulated DWI signals were fitted with the statistical distribution and DKI models using the Levenberg-Marquardt algorithm in MATLAB (Mathworks, Inc.). The goodness-of-fit was assessed using the reduced chi-square statistic (χ_ν^2) (Eq. (5.11)). The uncertainty of measurements (σ_i) was empirically determined to be three times of the SD of the simulated DWI signal (~ 9×10^{-3}). The standard monoexponential model was applied for comparison, and the ADC was calculated using the DWI signals with b = 0 and 1000 s/mm^2.

Pearson's correlation coefficient was used to evaluate the correlation between the fitted parameters of the diffusion models (ADC of the monoexponential model, D_{stat}, σ_{stat} of the statistical distribution model, D_{app}, K_{app} of the DKI model) and the modified microstructural parameters (2R, V, and P) with a significance level: 0.05 ($p < 0.05$). The percentage change of the fitted parameter was used to assess the sensitivity of the fitted parameter in response to the modified microstructural parameters.

The deviations of the fitted parameters due to noise were studied by simulating noisy MRI signals with a Rician distribution. The SNR level at b = 0 were set to be 50, which is typical in DWI experiments. The models were fitted to

the simulated noisy data with b = 2500 s/mm^2. The experiments were repeated 10,000 times by adding the noise independently in each experiment, and the average and the SD of the fitted parameter was calculated across experiments.

5.3.2 Results

The simulation was validated by comparing with the analytical signal attenuation of free and restricted diffusion (Fig 5.8a-b). The minimum precision of the simulation reached 5×10^{-3} (dash line in Fig. 5.8a) with a relative error less than 2×10^{-3}. The noise floor of this simulation was set to be 5×10^{-3}. The simulated signal attenuation of restricted diffusion approximated the diffraction pattern better with the narrower pulse width (Fig. 5.8b). This agrees with the effects of finite pulse width shown by the previous study (Linse and Soderman 1995). The simulated DWI signals with the prescribed microstructural changes caused non-monoexponential attenuation (Fig. 5.8c,d,e). The minimum signal was 2.7×10^{-2}, which was above the noise floor of this simulation (5×10^{-3}).

The quadratic cumulant expansion models (the DKI model and the statistical distribution model) fit all the datasets inside a 95 % confidence interval with b = 2500 s/mm^2 (Table 5.1).

When cell size became larger, the ADC, D_{stat}, D_{app}, and the σ_{stat} positively correlated with cell size, and the K_{app} inversely correlated with cell size (Fig. 5.9). When cell volume fraction was increased, the ADC, D_{stat}, D_{app}, and the σ_{stat} inversely correlated with cell volume fraction, but the K_{app} showed no correlation with cell volume fraction. When membrane permeability was larger, the ADC, D_{stat}, and D_{app} positively correlated with membrane permeability. The K_{app} was in-

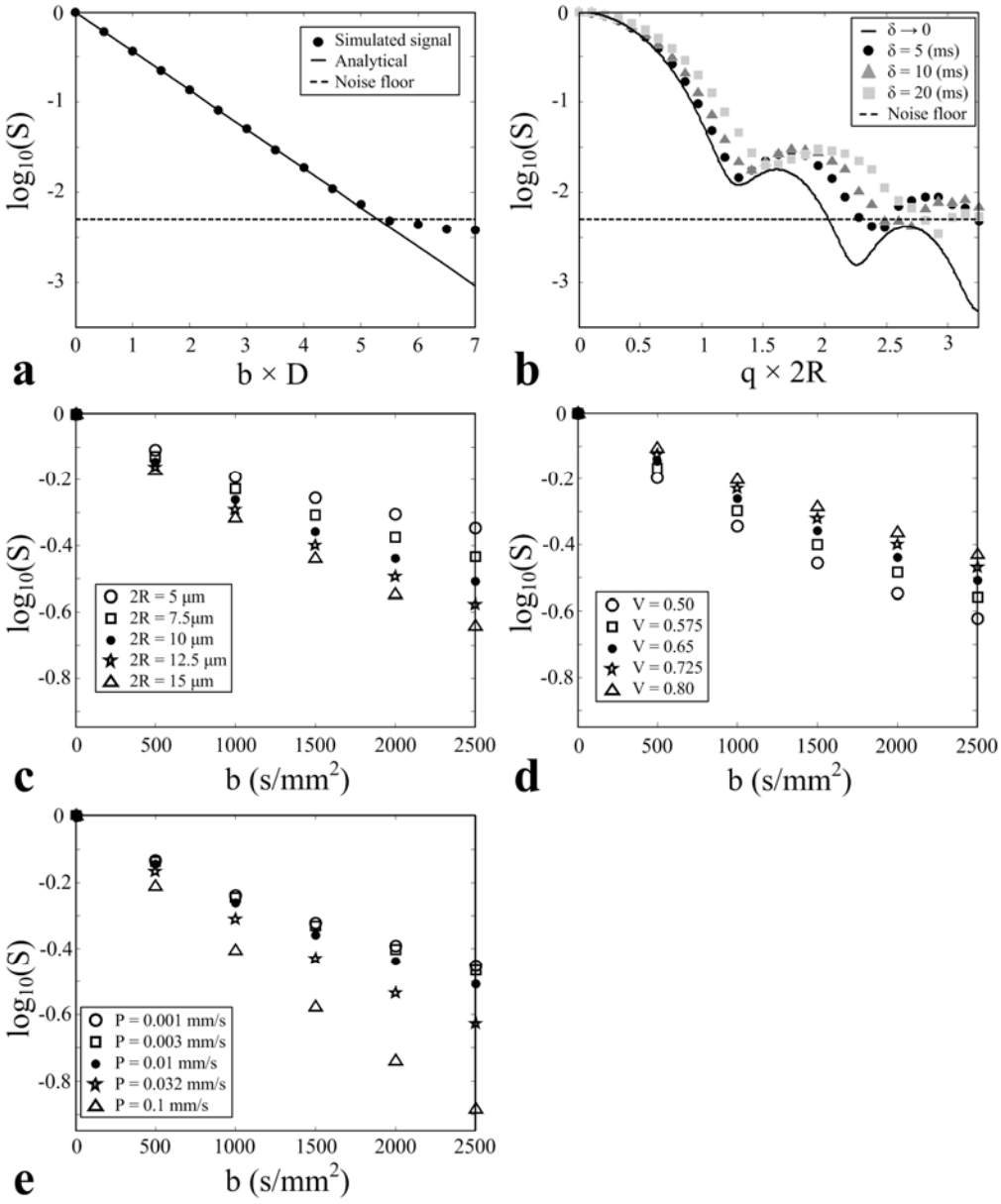

Figure 5.8: a-b: Comparison between the simulated DWI signals and the analytical signal attenuation of free diffusion (a) and restricted diffusion within cells (cell size (2R): 15 μm) (b), where $q = \gamma g \delta$. c-e: Simulated DWI signals versus b-value with the microstructural changes in cell size (2R), cell volume fraction (V), and membrane permeability (P).

Changes in microstructural parameters	χ_ν^2
2R = 5 μm	1.09
2R = 7.5 μm	0.82
2R = 10 μm	0.73
2R = 12.5 μm	0.57
2R = 15 μm	0.49
V = 0.50	1.76
V = 0.575	1.16
V = 0.725	0.38
V = 0.80	0.05
P = 0.001 mm/s	1.07
P = 0.003 mm/s	1.06
P = 0.03 mm/s	0.28
P = 0.1 mm/s	0.03

Table 5.1: The reduced chi-square statistic (χ_ν^2) of the quadratic expansion fits (the DKI and the statistical model) to the datasets with simulated microstructural changes in cell size (2R), cell volume fraction (V), and membrane permeability (P). The changes of the microstructural parameters were made with other parameters kept constant; 2R = 10 μm, V = 0.65, and P = 0.01 mm/s.

versely correlated with membrane permeability. However, the σ_{stat} showed no correlation with membrane permeability.

The ADC, D_{stat}, D_{app} were sensitive to all simulated microstructural changes other than the decrease in membrane permeability (Fig. 5.10). By contrast, the σ_{stat} was specifically sensitive to both the increase and decrease in cell volume fraction. The K_{app} was specifically sensitive to the decrease in cell size and the increase in membrane permeability.

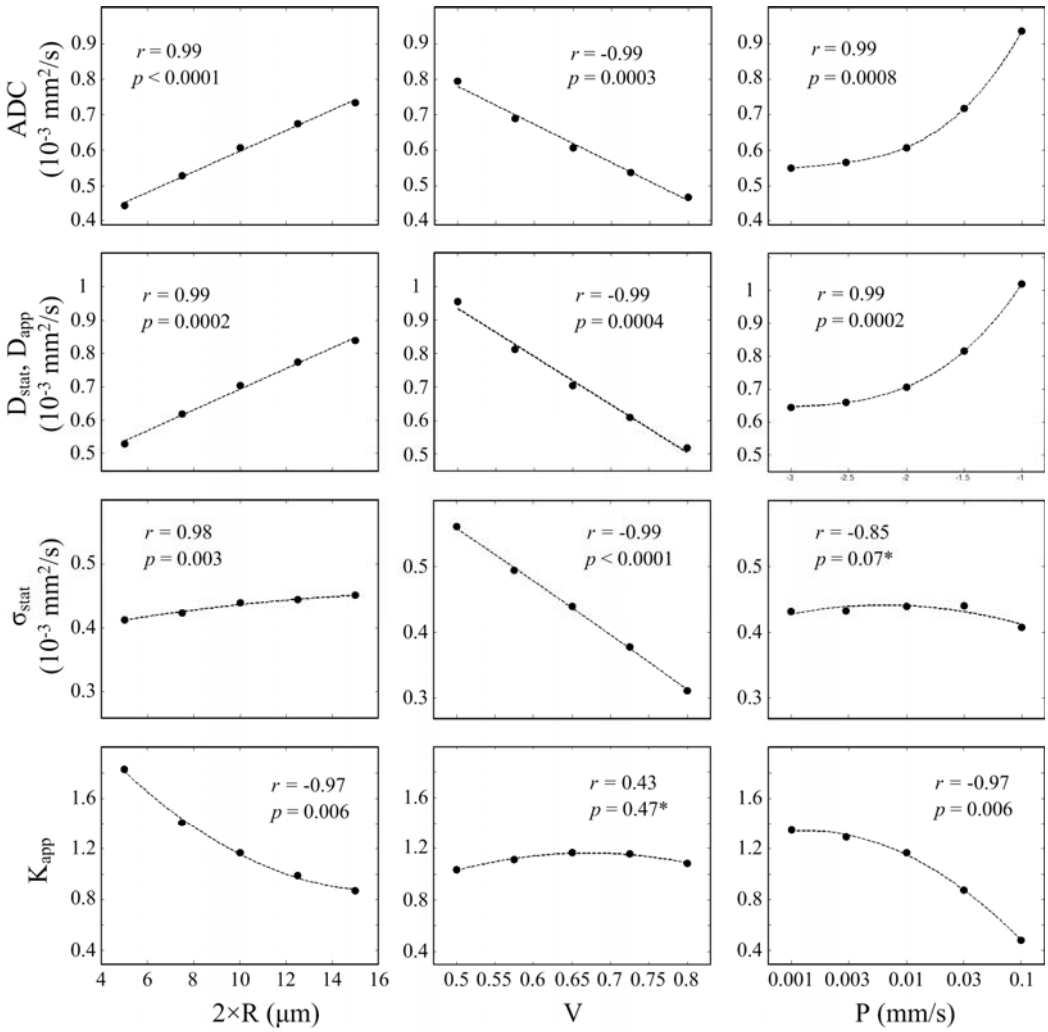

Figure 5.9: Correlations between the fitted parameters and simulated microstructural changes in cell size (2R), cell volume fraction (V), and membrane permeability (P); ADC of the monoexponential model, D_{stat}, σ_{stat} of the statistical distribution model, and D_{app}, K_{app} of the DKI model. * indicates that a correlation is insignificant ($p > 0.05$).

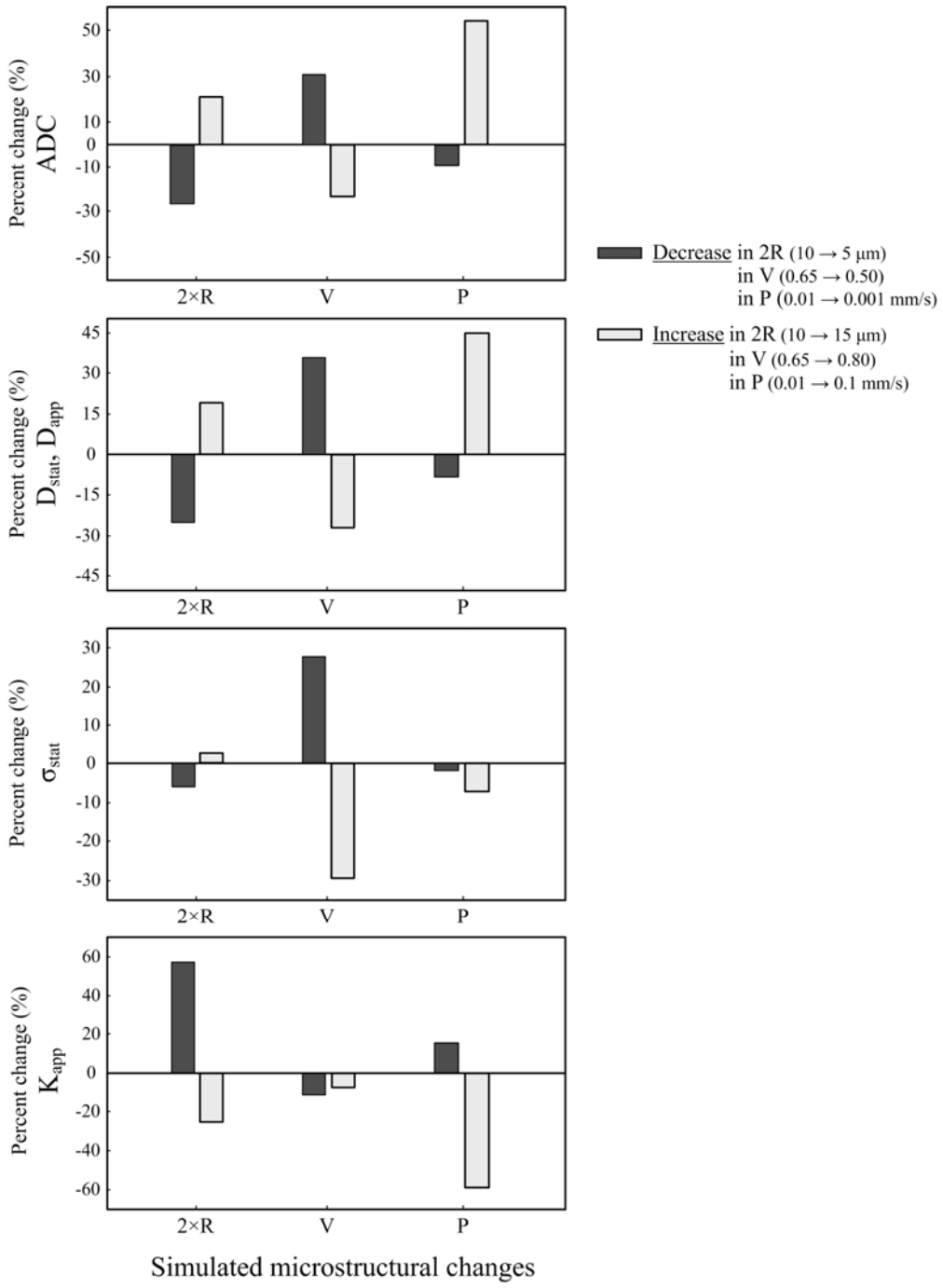

Figure 5.10: Percentage changes of the fitted parameters in response to a decrease and an increase in cell size (2R), cell volume fraction (V), and membrane permeability (P); ADC of the monoexponential model, D_{stat}, σ_{stat} of the statistical distribution model, and D_{app}, K_{app} of the DKI model. Note that the σ_{stat} was uncorrelated with the changes in membrane permeability, and the K_{app} was uncorrelated with the changes in cell volume fraction, as shown in Fig. 5.8.

The percentage changes of the fitted parameters obtained from the simulated noisy data (Fig. 5.11) were consistent with those obtained from the noise-free data (Fig. 5.10). This suggests that the models were insensitive to the simulated rectified noise floor. However, the fitted parameters showed fluctuations due to the simulated noise. In particular, the σ_{stat} showed the largest sensitivity to the simulated noise fluctuations (Fig. 5.11).

5.3.3 Discussion

We investigated the relationship between the statistical distribution and DKI models and simulated microstructural changes, specifically cell size, cell volume fraction, and membrane permeability. We compared the results of these models to those of the monoexponential model. The parameters ADC, D_{stat}, and D_{app} were sensitive to all of the simulated microstructural changes except the decrease in membrane permeability. The ADC, D_{stat}, and D_{app} increased with cell size and membrane permeability, and decreased with cell volume fraction. The measured width of the distribution of diffusion rates (P(D)) by σ_{stat} was specifically sensitive to the changes in cell volume fraction. The σ_{stat} increased with smaller cell volume fraction. The measured index of non-Gaussian water diffusion by K_{app} was specifically sensitive to the decrease in cell size and the increase in membrane permeability. The parameter K_{app} increased with smaller cell size and decreased with larger membrane permeability. We propose that the different sensitivities of these two models may contribute to the observed differences in the previous *in vivo* experiments [70,93-97,111]. More importantly, a combination of these non-Gaussian diffusion models may lead to a better identification and detection of

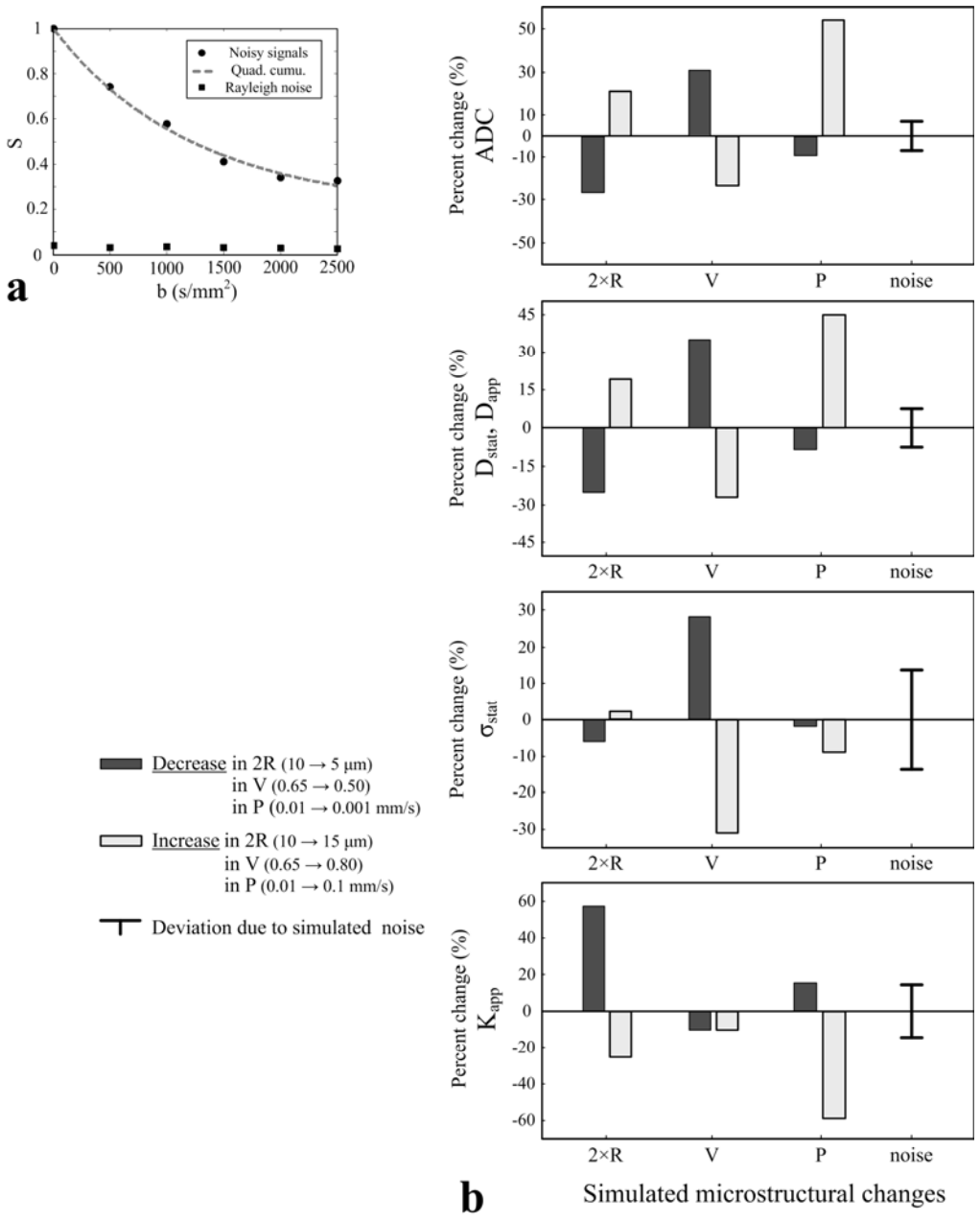

Figure 5.11: Effects of simulated MRI noise (SNR = 50 at b = 0 s/mm^2) on the fitted parameters: a: An example of model fits to the simulated noisy DWI signals. b: Comparisons between percentage changes of the fitted parameters in response to a decrease and an increase in cell size (2R), cell volume fraction (V), and membrane permeability (P), and fluctuations due to the simulated noise; ADC of the monoexponential model, D_{stat}, σ_{stat} of the statistical distribution model, and D_{app}, K_{app} of the DKI model. The percentage change and fluctuation of the fitted parameter were calculated using the average and SD of the fitted parameter across 10,000 experiments.

disease progression. However, cautions should be taken about the increased sensitivity of these models to noise fluctuations at higher b-values (Fig. 5.11).

Our simulated physical system includes randomly packed, 2-D semi-permeable circular cells with the continuously distributed cell size to simulate tissue heterogeneity. Our simulated diffusion time is long ~ 26 ms ($\Delta - \delta/3$) but does not reach long diffusion limit ($\Delta \rightarrow \infty$). Nontheless, the correlations of the ADC with the simulated microstructural changes (Fig. 5.9) are consistent with the correlations predicted by the theoretical tissue model [30] consisting of regularly spaced, semi-permeable 3-D square cylinders at long diffusion time limit. Our chosen cell volume fraction was 0.65, which is lower than their simulated cell volume fraction (0.80) [30], in an attempt to facilitate the variation of the cell volume fraction (0.50 – 0.80) in a random cell packing.

A 2-D computer model can be used to simulate water diffusion perpendicular to the fiber direction of white matter with a typical axonal size (~ 1-3 μm) [30,102,104]. In this study, the simulated 2-D microstructure with a typical cell size of 10 μm was used to approximate a 3-D isotropic microstructure by assuming that the measurements of water diffusion are approximately equal along any direction. We expect that the relationship between the diffusion models and simulated microstructural changes should be similar between a simulated 2-D and 3-D microstructure. However, in an anisotropic microstructure, water diffusion should be directionally dependent in response to microstructural changes [30].

The previous measurements of intracellular water diffusion on HeLa cells [92] has shown that the σ_{stat} correlates with the width of cell size distribution at long diffusion times. In our study, the σ_{stat} measured at a long diffusion time was

specifically sensitive to the simulated changes in cell volume fraction, and it increased with a smaller cell volume fraction. We suspect that the changes in cell volume fraction may directly influence the distribution of intra/extra-cellular compartmental sizes, and smaller cell volume fraction may correlate with an increased width of the compartmental size distribution.

Our experiments showed that the K_{app} had an inverse correlation with the measured diffusivity (ADC, D_{stat}, and D_{app}) upon the change in cell size and membrane permeability (Fig. 5.9). This inverse relationship can be expected from Eq. (5.9). However, the uncorrelated relationship between the K_{app} and the changes in cell volume fraction may be a result of the concurrent increase or decrease of the measured width of P(D) (σ_{stat}) and the measured diffusivity (D_{stat}) (Eq. (5.9)).

A decrease of ADC by approximately 40–60 % following ischemic stroke has been shown by previous studies [1,46]. The underlying mechanisms of this reduction in ADC remain unclear. The increased cell volume fraction is suggested to be one mechanism that results in more hindered extracellular diffusion [48,80]. However, the intracellular diffusion was found to decrease [112,113] or increase [114] at long diffusion times. Another factor of reduced membrane permeability was shown to have a minor impact on the reduced ADC using a Monte Carlo simulation [30]. One recent study applying the DKI on human stroke [99] has shown an increased K_{app} (84 % increase versus 52 % decrease in the ADC). We suggest that this observed increase of the K_{app} may arise from a decrease in cell size following ischemia, as our results showed that the increase of the K_{app} was

sensitive to the decreased cell size and was relatively insensitive to the increased cell volume fraction and decreased membrane permeability (Fig. 5.10).

Limitations of this study include the simplification of intra/extra-cellular structures by neglecting intracellular organelles, cytoplasm, and extracellular matrix, which are also important parameters of the pathological mechanisms [109,115]. Our simulation also neglected T_2 relaxation in intra/extra-cellular compartments, which has been shown to affect the relation between the ADC and microstructural changes [116].

At relatively low b-values ($b \leq 2500$ s/mm^2), the statistical distribution and DKI models are less sensitive to the effects of MRI noise compared with the stretched exponential model fitted with typical high b-values of 4000-5000 s/mm^2. However, at high b-values, the DWI signal arises from water protons with a slower diffusivity. Thus, non-monoexponential models applied at low b-value may not detect microstructural changes related to water with slower diffusivity.

In conclusion, we simulated three important microstructural changes (cell size, cell volume fraction, and membrane permeability), and investigated how the diffusion models responded to the changes. The ADC, D_{stat}, and D_{app} were sensitive to all these changes except for the decrease in membrane permeability. The σ_{stat} was specifically sensitive to the changes in cell volume fraction. The K_{app} was specifically sensitive to the decrease in cell size and the increase in membrane permeability. These results suggest that the models of non-Gaussian water diffusion have different, specific sensitivities and may be used together to better understand the biophysical changes in disease.

Chapter 6

ENHANCED PROPELLER DIFFUSION-WEIGHTED MR IMAGING

This chapter discusses the improvements to PROPELLER diffusion-weighted MR imaging. The violation of the CPMG condition of PROPELLER DWI leads to signal losses and phase inconsistencies between odd and even echoes. The signal losses is mitigated using the phase modulation of refocusing RF pulses, such as MLEV schemes [66]. However, the phase inconsistencies are difficult to remove when a receive-only phase coil such as a phased-array coil is used to increase SNR. The split-blade approach [104] has been proposed to encode odd and even echoes into separate blades. It minimizes phase inconsistencies but results in a smaller navigated region. This work introduces the whole-blade method to minimize the phase inconsistencies while keeping the larger navigated region. The results are compared to the results with the split-blade method.

The FSE-based PROPELLER DWI also causes high SAR and long scan time. Lately, faster PROPELLER techniques, including Turboprop [16], X-prop [23] and Steer-prop [117], have been proposed using a GRASE [18] readout to accelerate the sampling with fewer refocusing RF pulses. However, these faster PROPELLER methods are subject to the phase error arising from off-resonance and system imperfections. This study presents a new phase correction to Turboprop, called Turboprop+. Turboprop+ is then compared to other 'turbo' versions of PROPELLER, specifically Turboprop and X-prop. The Turboprop+ is

also compared to clinical standard EPI method using the same effective image resolution and NEX.

6.1 Background

6.1.1 Split-blade Method

A PROPELLER blade is composed of odd and even echoes. The motion induced phase alternating between odd and even echoes creates phase inconsistencies in a PROPELLER blade. The appropriate phase ordering for either odd or even echoes to produce a consistent motion induced phase only applies using a transmit-receive coil [15]. When a receive-only phase coil is used, an additional coil phase is added to each acquired echo. This coil phase is slowly spatially varying without alternating between odd and even echoes. The mixture of the coil phase and the motion induced phase in a PROPELLR blade makes it difficult to remove the phase inconsistencies.

To address the problem, a method called 'split blade' method [118] has been presented by encoding odd and even echoes into separate blades (Fig. 6.1). In the split blade method, because the motion induced phase and coil phase are consistent throughout every phase-encoded line, the remaining phases in the blade image formed by odd and even gradient echoes can be approximated as:

$$\Phi_{odd}(x, y) = \Phi_{coil}(x, y) + \Phi_{motion}(x, y)$$
$$\Phi_{even}(x, y) = \Phi_{coil}(x, y) - \Phi_{motion}(x, y) \quad (6.1)$$

The coil phase is measured in a blade image without diffusion weighting (b = 0) by applying a pyramid function to the data blade in *k*-space to keep the Gibbs ringing phases in the phase-encoded direction (Fig. 4.12). After removing the coil

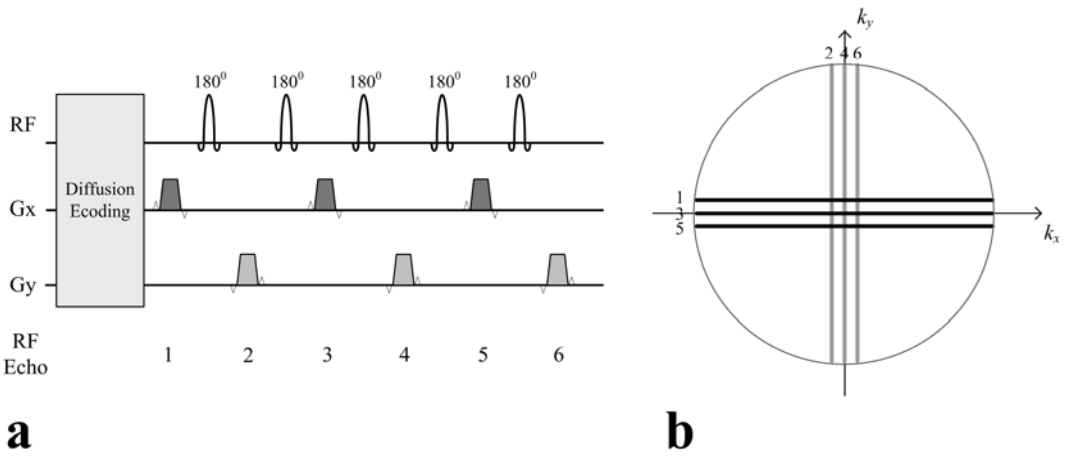

Figure 6.1: Illustration of the split-blade approach, where odd and even echoes are encoded into separate PROPELLER blades, which are oriented orthogonally to each other. At subsequent T_Rs, the blades are rotated to fill a full circle.

phases, coil images are combined and the remaining motion induced phase in a diffusion-weighted blade image of odd and even echoes can be removed respectively.

The encoding scheme of the split blade method, however, results in a smaller navigated region. As illustrated in Fig. 6.1b, for an ETL of 6, the area of the navigated region is 9 (3×3) using the split-blade method, which is only 25 % of the original navigated area of 36 (6×6). In the presence of the rapid varying motion induced phase, the majority of *k*-space data can possibly shift out of the blade, which cannot be corrected by simply removing the motion induced phase [16].

6.1.2 Turboprop DWI

The pulse sequence diagram of Turboprop is shown in Fig. 6.2. It collects multiple gradient echoes around each primary spin echo, and the turbo factor is defined as the number of gradient echoes between each pair of refocusing RF

pulses. Compared with PROPELLER DWI, Turboprop DWI thus achieves more efficient *k*-space sampling with fewer refocusing RF pulses, which decreases SAR. The resulting wider blade also facilitates removing the motion-induced phase. Those benefits of Turboprop, however, are compromised by the increased sensitivity to the phase errors encountered in both EPI or GRASE-based methods. One source of the phase error is off-resonance arising from field inhomogeneity, magnetic susceptibility, and chemical shifts [59,119]. This leads to T_2^* signal loss and ghosting artifacts because of the different off-resonance phase accrual between the phase-encoded lines. Another source of the phase error is system imperfections, such as eddy currents and hardware group delays, resulting in primarily an echo shift along the direction of readout gradient [119,120]. Oscillating readout gradients employed in Turboprop (Fig. 6.2a) thus induce misregistration of gradient echoes, exhibited as ghosting artifacts [119]. Furthermore, data blades in Turboprop are collected with slightly different phase errors, and this data inconsistencies cause signal loss and streaking artifacts [16] even without subject motion. The problem of data inconsistencies is even more exacerbated by the motion-induced phase from the diffusion gradients.

The reference scan method [61] (Fig. 4.7) used with EPI is the typical approach to correct the phase error. This method requires an extra collected reference data without phase encoding to measure the echo shift and constant phase offset for each phase-encoded line. It was used to correct the phase error in Turboprop, where reference data is collected along directions of physical gradients x and y respectively to correct the anisotropic phase error of each rotated blade [121] (Fig. 6.3). However, this method is inadequate when there is a

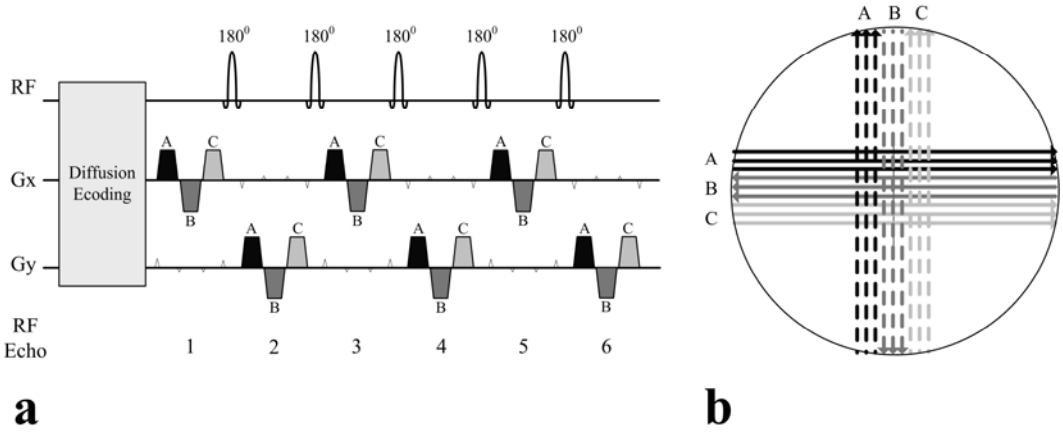

Figure 6.2: Pulse sequence diagram (**a**) and *k*-space sampling scheme (**b**) of split-blade Turboprop. The solid lines refer to odd echoes and the dash lines refer to even echoes. Illustrations are for the turbo factor of 3 and ETL of 6 in one T_R.

large off-resonance phase accrual along the phase-encoded direction [59]. Besides, the off-resonance phase in each rotated blade of Turboprop is different and is insufficiently calibrated by using reference data oriented solely along physical gradients x and y.

6.1.3 X-prop DWI

Another method to accelerate acquisition of PROPELLER is X-prop [122], where the individual gradient echoes are encoded into separate data blades (Fig. 6.4). The idea is also very similar to the recently proposed Steer-prop [117]. Unlike Turboprop, where a data blade is composed of the different gradient echoes, in X-prop, the data blade is encoded by the same gradient echoes with the same gradient polarity. Thus, the echo shifting because of the off-resonance phase accrual and system imperfections is consistent in a data blade, and the phase error can be removed from each data blade using image-space phase correction [15].

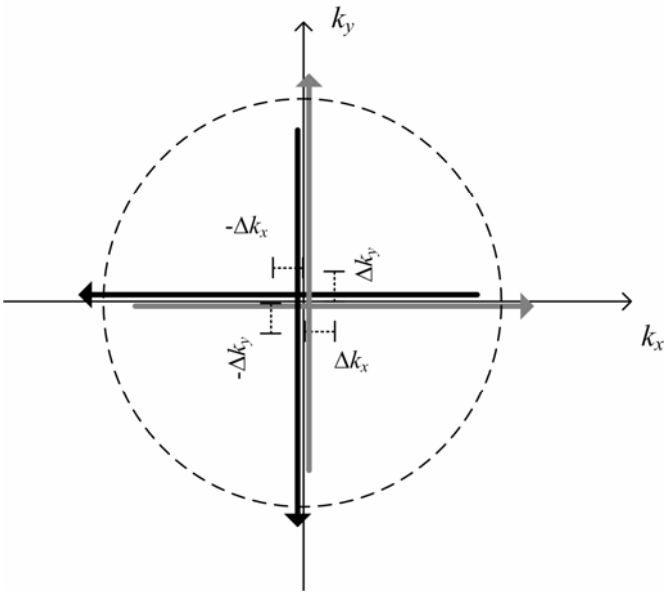

Figure 6.3: Reference scan method in Turboprop correcting for the anisotropic gradient shift and constant phase offset. The reference scan is applied on physical axis x and y respectively, and the measurements are used to circularly interpolate the gradient delays at different orientations.

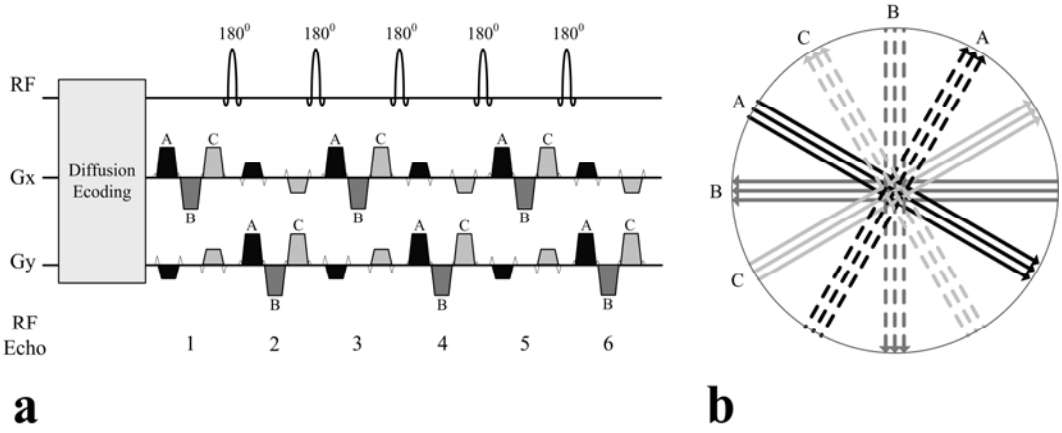

Figure 6.4: Pulse sequence diagram (a) and *k*-space sampling scheme (b) of split-blade X-prop. The solid lines refer to odd echoes and the dash lines refer to even echoes. Illustrations are for the turbo factor of 3 and ETL of 6 in one T_R.

Because no reference scan is required, X-prop achieves faster acquisition with fewer image artifacts than Turboprop. Nonetheless, the sensitivity to the T_2^* signal loss is increased in X-prop by placing the data blades of every gradient echo at the center of *k*-space. The effect of T_2^* signals loss is most apparent when the turbo factor is high [122].

6.2 Whole-blade Method

The split-blade method has addressed the inconsistent phase between odd and even echoes in a non-CPMG echo train. However, the blade width is cut down by half and area of self-navigated region is reduced by 75 % (Fig. 6.1). One way to enlarge the self-navigated region in split-blade method is to increase the ETL. However, this results in a prolonged TE and loss of SNR. This study introduces an approach to combine even and odd echoes into a single blade, called whole-blade method [123]. In contrast to the previous scheme, where the blade images of b = 0 s/mm^2 are averaged to measure the coil phase, this study employs the reference blades, which measure the coil phase for each rotated data blade more accurately. The reference blades are also served as a training data for parallel imaging, called Generalized Autocalibrating Partially Parallel Acquisition (GRAPPA), which further widen the blades and reduce the scan time.

6.2.1 Methods

The flowchart of the whole blade method is shown in Fig. 6.5. Assuming coil phase is slowly varying, it is removed by applying image-space phase correction [15]. Assuming the coil phase is sufficiently removed, the remaining phase in the diffusion-weighted image is the motion induced phase, alternates the sign between

even and odd echoes (Eq. (6.1)). Simply by conjugating either the odd echoes or the even echoes, the resulting motion induced phase is consistent in a data blade. However, the conjugate of image-domain signals corresponds to the conjugate of Fourier-domain signals with reversed frequency and phase-encoding directions [15].

$$\Phi^{*}_{odd}(x, y) = \Phi_{even}(x, y)$$

$$\Omega^{*}_{odd}(-k_x, -k_y) = \Omega_{even}(k_x, k_y) \tag{6.2}$$

Therefore, the inverse operations have to be done to the echoes prior to the conjugation of the echoes. After the combination of the odd and even echoes, the remaining reconstruction is the same as for conventional PROPELLER DWI (Fig. 6.5).

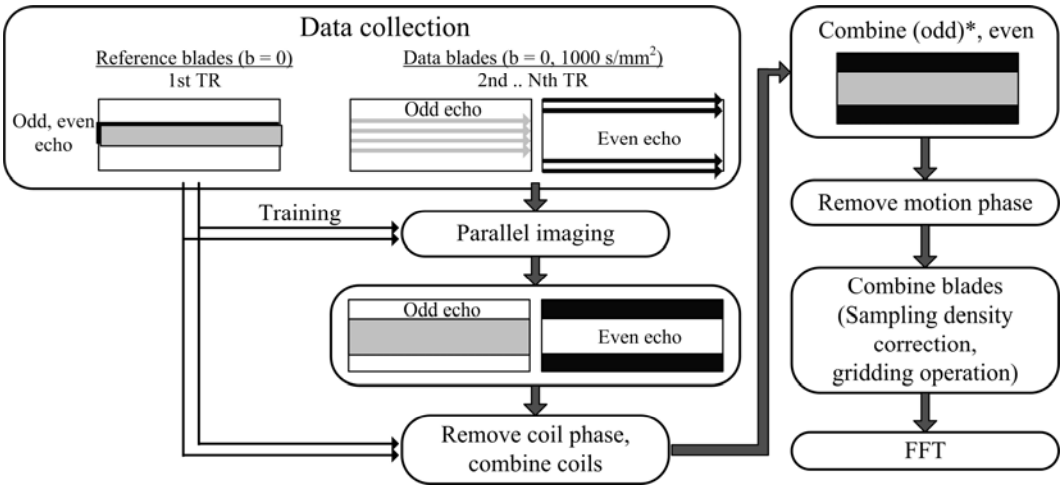

Figure 6.5: Reference blades are collected with no acceleration using odd and even echoes respectively on identical strips in *k*-space, at every blade angle, but only for b = 0. They are collected along with data blades (odd echoes at the center, and even echoes at the edge of the blade), collected with acceleration (R = 2) for all b-value and diffusion directions. After the GRAPPPA, each coil phase is removed for complex coil combination. The whole blade is then created by combining the even echoes and the conjugate of odd echoes. The remaining reconstruction is the same as for the standard reconstruction of PROPELLER DWI.

6.2.2 Experiments

All human studies were approved with the institutional review board and informed consent was obtained from each healthy volunteer. Pulse sequences were implemented on a GE Signa HDx 3 Tesla MR scanner (Milwaukee, Wisconsin) with an eight-channel brain head coil and a gradient system with maximum strength 40 mT/m.

The whole-blade method was applied to the conventional PROPELLER DWI (turbo = 1) and X-prop DWI with the turbo factor of 5. Three-axis DWI images: b = 0 and 1000 s/mm^2 (x, y, and z) were acquired with an entire brain coverage (20 slices). Other imaging parameters were: 192 diameter matrix, FOV

of 240 mm, 20 slices with thickness/gap of 5/1.5 mm, ETL of 16 (PROPELLER), ETL of 12 (X-prop), BW of ± 50 kHz (PROPELLER), and BW of ± 100 kHz (X-prop). The images were also collected using the split-blade method with the identical slice coverage and imaging parameters.

6.2.3 Results and Discussion

The comparisons of the results using the split-blade method and the whole-blade method are shown in Fig. 6.6 (PROPELLER) and Fig. 6.7 (X-prop). The results of whole blade were comparable with split blade method in SNR and artifacts, indicating that the odd/even echo phase inconsistencies were successfully addressed.

For the same ETL, the whole blade method of PROPELLER DWI can produce 4 times the area of the self-navigated region than the area produced by the split blade method (Fig. 6.8a-b). However, this benefit may not be applicable to the X-prop because the areas of the self-navigated regions of the two methods are similar. In addition, the phase inconsistencies may still exist during the combination of odd and even echoes may remain when the coil phase is insufficiently removed.

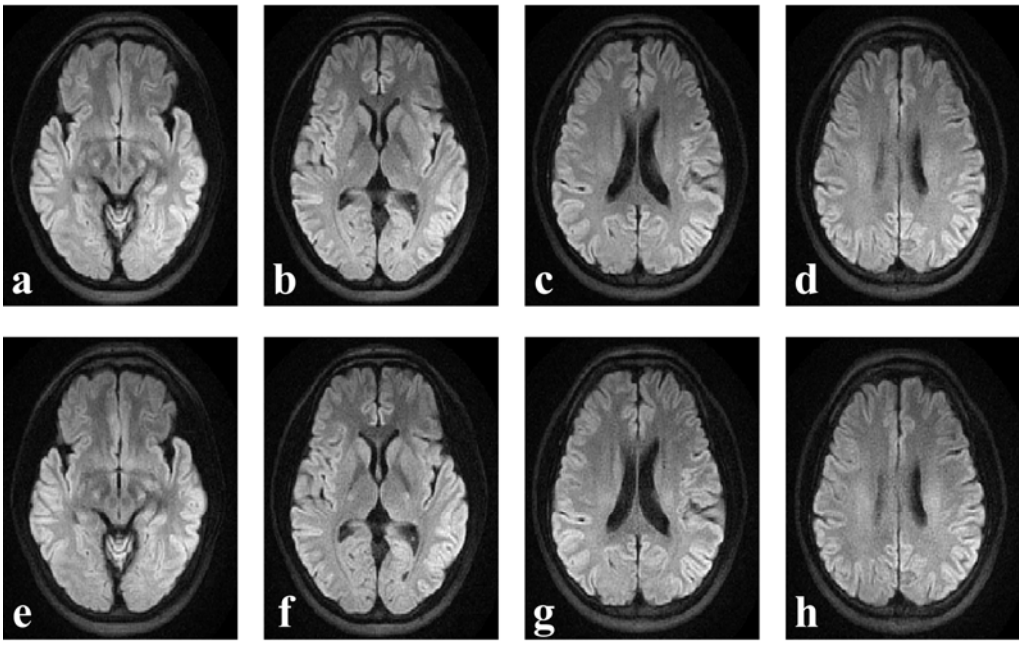

Figure 6.6: Isotropic DW images by a-d: split-blade, and e-h: whole-blade method of conventional PROPELLELR (turbo = 1). All are undersampled with R = 2. 4 out of 20 slices are shown with total scan time: split-blade PROPELLER (4' 14"), and whole-blade PROPELLER (5' 15").

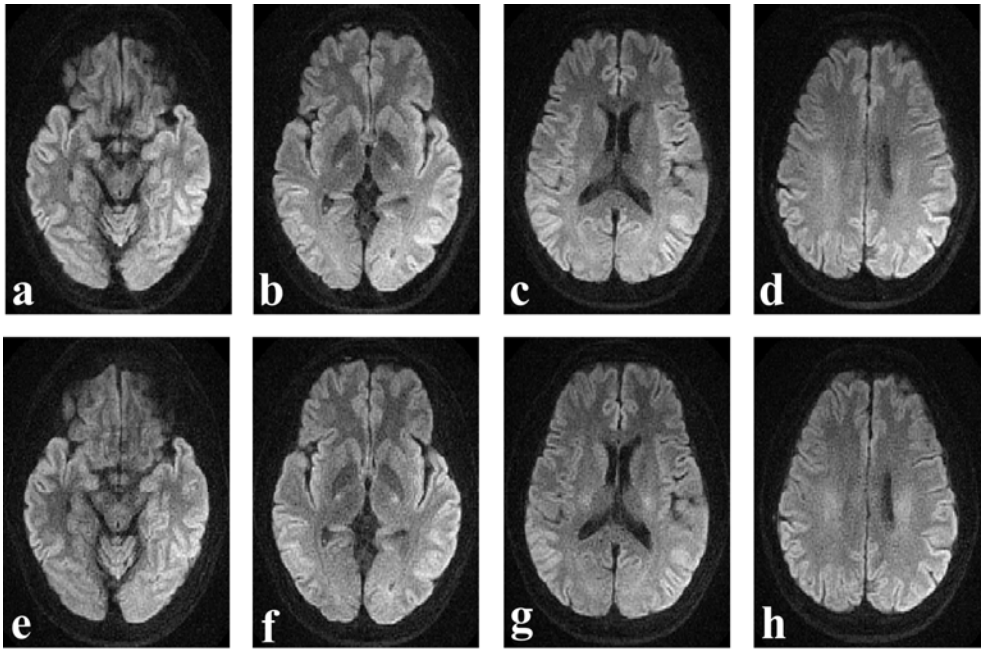

Figure 6.7: Isotropic DW images by a-d: split-blade, and e-h: whole-blade method of X-prop (turbo = 5). All are undersampled with R = 2. 4 out of 20 slices are shown with total scan time: split-blade X-prop (1' 37"), and whole-blade X-prop (2').

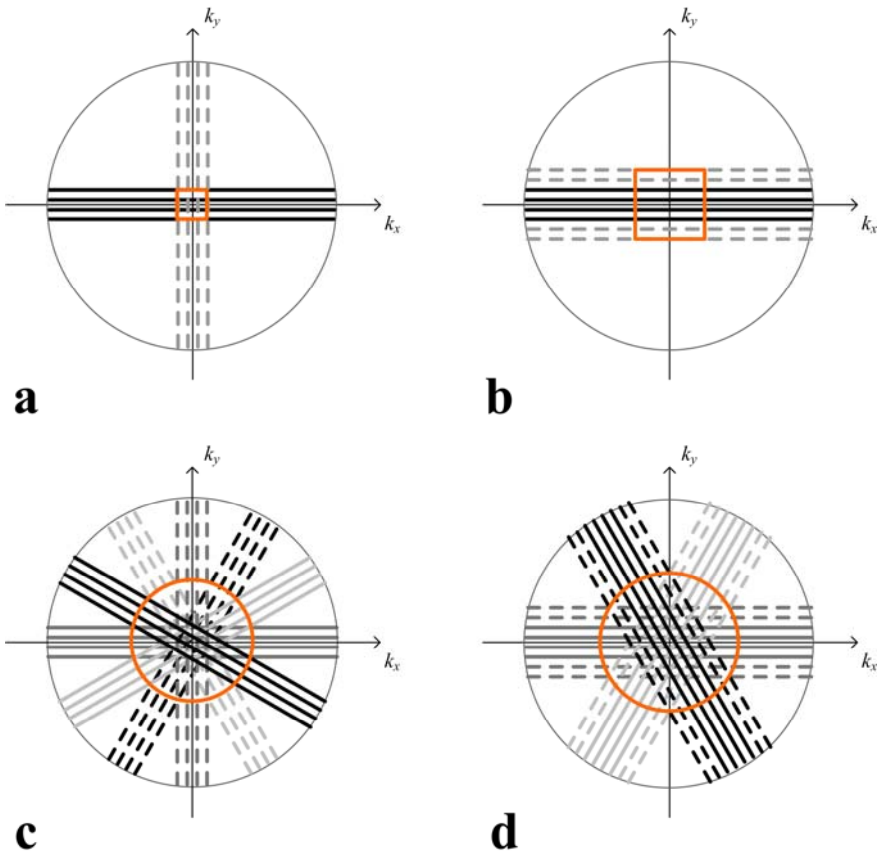

Figure 6.8: *k*-space trajectory at one T_R. The split-blade method: a (PROPELLER) and c (X-prop) and whole-blade method: b (PROPELLER), and d (X-prop). The orange-square and -circle indicate the area of self-navigated regions.

6.3 Turboprop+

Despite the previous attempts to address the phase errors in Turboprop, the turbo factor is nonetheless limited by the increased artifacts due to off-resonance related phase errors especially at high magnetic field. In this work, we introduce a more complete method to correct phase errors in Turboprop, called 'Turboprop+'. The proposed method utilizes calibration blades which are rotated in the same fashion as the Turboprop blades to measure and then remove phase errors originating from off-resonance and system imperfections. Turboprop+ is then compared to other 'turbo' versions of PROPELLER, specifically Turboprop and

X-prop. It is also compared to clinical standard EPI method using the same effective image resolution and NEX.

6.3.1 Methods

Figure 6.9 illustrates the flowchart of the proposed phase correction in Turboprop+. The flip angle of each RF refocusing pulse is assumed to be a perfect 180° with the negligible phase modulation from multiple signal pathways [63], so the amount of off-resonance related phase accrual of the gradient echo increases linearly with the time away from the refocusing time point. A sub-blade represents a *k*-space strip encoded by the same gradient echo (Fig. 6.9b), and the phase-encoded lines of the sub-blade should have consistent phase errors because of their identical readout gradient polarity and off-resonance related phase accumulation. By assuming that phase errors of each sub-blade are slowly varying in space and only negligible subject motion occurs between the scans, the 2-D phase error maps of each sub-blade are created by the extra collected calibration blades at the central *k*-space with b = 0 (Fig. 6.9b). With these phase error maps, the phase errors can then be removed from each sub-blade using image-space phase correction [15]. After the removal of the phase error, the sub-blades are concatenated into one single, wider data blade. The same procedure for the phase correction is applied to the all rotated data blades. Following the phase correction, the remaining reconstruction is the same as for conventional PROPELLER DWI [15].

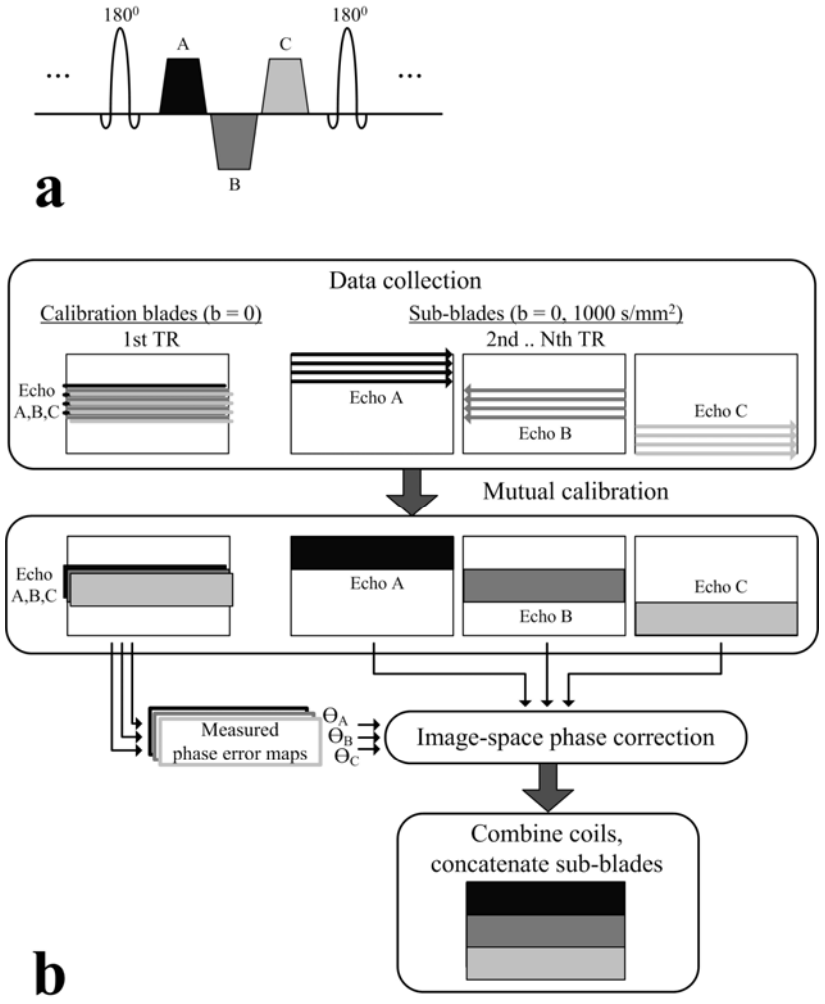

Figure 6.9: Illustration of readout gradients (a) and flowchart (b) of Turboprop+ with the turbo factor = 3. Calibration blades are collected with acceleration (R = 2) on identical strips in *k*-space, at every blade angle, but only for b = 0, using every gradient echo (A, B, C) respectively. They are collected along with sub-blades, collected with acceleration (R = 2) for all b value and diffusion directions. Each sub-blade covers different *k*-space segments encoded by different gradient echoes (A, B, C). After the mutual calibration, the fully sampled calibration blades are windowed by a pyramid function, zero-padded, and Fourier-transformed (Ref. 15) to create phase error maps, which are used to remove the phase errors from each sub-blade. Following the phase correction and coil combination, sub-blades are concatenated into one single, wider data blade. The same procedures of the phase correction are applied to the data blades at every blade angle. The remaining reconstruction is the same as for the standard reconstruction of PROPELLER DWI (Ref. 15).

The accuracy of the calibrated phase error map is related to the blade width of the calibration blade. An image location with large magnetic susceptibility changes, such as an air-tissue interface, can produce the rapidly varying phase errors. The rapidly varying phase errors can shift the majority of *k*-space data out of the calibration blade, creating an inaccurate phase error map. The original calibration blade width is equal to the echo train length (ETL) (Fig. 6.9b), but is cut down to be half the ETL (ETL/2) because of the application of split blade method [118], which attempts to address the non-Carr-Purcell-Meiboom-Gill (non-CPMG) phase alternation between even and odd echoes. To widen the calibration blade, a parallel imaging technique using mutual calibration [124] in split-blade PROPELLER is employed in Turboprop+, and the resulting calibration blade width is increased by 80% or 0.9 × ETL.

In Turboprop+, the calibration blades are rotated in accordance with the data blades, but are only collected with b = 0. Consequently, the additional time required for collecting calibration blades is effectively the time to acquire an additional b = 0 image, but with the data used for calibration. This increase in scan time is small when compared with standard Turboprop, where 4 extra T_Rs are required to collect the reference data.

All human studies were approved with the institutional review board, and informed consent was obtained from each healthy volunteer. Pulse sequences were implemented on a GE Signa HDx 3 Tesla MR scanner (Milwaukee, Wisconsin) with a gradient system with maximum strength 40 mT/m, and using an eight-channel phased array head coil.

The purpose of this experiment was to examine the effects of the phase error on DWI images by increasing the turbo factor from 3 to 7, and to compare the results of Turboprop, X-prop, and Turboprop+ with these changes in the turbo factor. DWI images: b = 0 and 1000 s/mm^2 (x, y, and z) were acquired along physical axes x, y, and z respectively using Turboprop+ with an entire brain coverage (20 slices). Images with identical slice coverage were also acquired using Turboprop and X-prop. Split-blade acquisition and parallel imaging using mutual calibration (R = 2) were applied in all cases. To minimize effects on DWI other than the turbo factor, the ETL (number of refocusing pulses) was reduced at the larger turbo factor to minimize the differences in the T_E. The ETL was set to be 14, 12, 10 for the turbo factor: 3, 5, 7, resulting in the T_E: 130 ms, 139 ms, and 142 ms respectively. Other parameters were: 192 matrix, 240 mm FOV, 20 slices with thickness/gap: 5/1.5 mm, T_R = 5700 ms, R = 2, and BW = 200 kHz. The acquisition of each image required 4 TRs, which was the same for all three turbo factors. The time for collecting the calibration blades in Turboprop+ was approximately 23 sec (4 T_Rs), which was the same as collecting the reference data for Turboprop. The total scan time of X-prop (1 min 37 sec) was shorter than that of both Turboprop and Turboprop+ (2 min) in this experiment, since no calibrations are required for X-prop. The standard phase-encoding order [18] was implemented for both GRASE-based Turboprop and Turboprop+ in this study.

Another dataset was acquired using conventional PROPELLER (turbo factor = 1) as a baseline for comparison. Imaging parameters were: 192 matrix, 240 mm FOV, 20 slices with thickness/gap: 5/1.5 mm, ETL = 20, T_E/T_R = 133/7700 ms, R = 2, and BW = 100 kHz. The acquisition of each image required 8 T_Rs.

In a second experiment, Turboprop+ was compared to EPI method with the same effective image resolution and NEX (Turboprop+: 144 matrix, 1 NEX, and EPI: 128 × 128 matrix, 1 NEX). The effective image resolution is defined as the width of point spread function that is related to the area of *k*-space coverage, given that Nyquist sampling criterion is satisfied. Imaging parameters of Turboprop+ were: 240 mm FOV, 20 slices with thickness/gap: 5/1.5 mm, turbo factor = 7, ETL = 10, T_E/T_R = 123/4500 ms, R = 2, and BW = 200 kHz. The acquisition of each image required 2 TRs. Another set of images of the identical slice coverage were collected with the clinical EPI protocol; the parameters were: 20 slices with thickness/gap: 5/1.5 mm, T_E/T_R = 87/5400 ms, R = 2. The total scan time of Turboprop+ was 52 sec, and that of EPI was 23 sec.

In all experiments, subject motion between the calibration scan and the data collection was assumed to be negligible. To test this assumption, three successive Turboprop+ scans were performed on each of three healthy volunteers. The phase error maps collected during the first scan were used to correct the phase error of all the three scans, and the final reconstructured images of the three scans were compared. The normalized root mean squared error (NRMSE) was calculated to quantify the differences between the reconstructed images using the 'inter-scan' phase error maps and those using the 'intra-scan' phase error maps. The NRMSE is defined as the RMSE divided by the range of image intensity. Finally, the assumption of ideal 180° RF refocusing pulses was also tested by reducing the flip angle from 180° to 120° in successive Turboprop+ scans, and the images with different flip angles were compared.

6.3.2 Results

Figure 6.10 shows a comparison of DW images along the three orthogonal directions using Turboprop, X-prop, and Turboprop+ with the turbo factor = 7, and conventional PROPELLER (turbo = 1) as a baseline. Major differences were in the regions around nasopharynx (white arrows), and were consistently observed in the images of three diffusion-encoding directions and trace-weighted images. The ghosting artifacts in Turboprop were minimized in X-prop, which, however, still exhibited the prominent T_2^* signal loss. Both the ghosting artifacts and T_2^* signal decay were mitigated in Turboprop+.

The effects of modifying the turbo factor on DWI images by Turboprop, X-prop, and Turboprop+ are illustrated in Fig. 6.11. In the regions of temporal lobes (white arrows) with magnetic susceptibility variations, the ghosting artifacts in Turboprop and T_2^* signal loss in X-prop increased noticeably with the turbo factor. By contrast, Turboprop+ achieved a rather uniform image quality throughout the increase in the turbo factor.

A comparison between Turboprop+ and EPI is shown in Fig. 6.12. Although EPI showed higher SNR because of its shorter T_E and lack of RF refocusing pulses, the signal pile-up and warping artifacts in EPI were considerably reduced in Turboprop+ with an identical image resolution and NEX.

Figure 6.13 shows the effect of passive subject motion between the calibration scan and the data collection on Turboprop+. For each of three successive Turboprop+ scans, the phase correction was performed using the phase error maps collected during the first scan (scan 1), so there were more than 2 min

difference (scan 2) and more than 4 min difference (scan 3) between the phase error maps and the data collection. The results of three healthy volunteers showed the consistent image quality between the three successive scans, and the values of NRMSE were less than or equal to 1 %. This suggests that the presented phase correction appears robust to inter-scan passive movements, such as respiration and minor subject motion.

The effect of the flip angles of RF refocusing pulses on Turboprop+ is shown in Fig. 6.14. While the image contrasts remained similar, there was a decrease in SNR when the flip angle was reduced. The signal loss at the low flip angle is largely be due to the violation of the CPMG condition [15].

6.3.3 Discussion

Turboprop+ is presented as a means to address phase errors in Turboprop that results from off-resonance and system imperfections. By employing the calibration blades, phase error induced artifacts, including ghosting artifacts and T_2^* signal loss, were reduced to a great extent in Turboprop+ when compared to Turboprop and X-prop. Although a nominal increase in scan time is needed to collect the calibration blades, this method allows Turboprop+ to be applied with a high turbo factor, thus reducing SAR and scan time without compromising the image quality. The benefit of Turboprop+ is further demonstrated by its comparison with clinical standard EPI (Fig. 6.12), where the severe geometric distortions in EPI were notably mitigated using Turboprop+ with a scan time less than 1 min. Turboprop+ thus is a promising tool for data acquisition in research and clinical DWI.

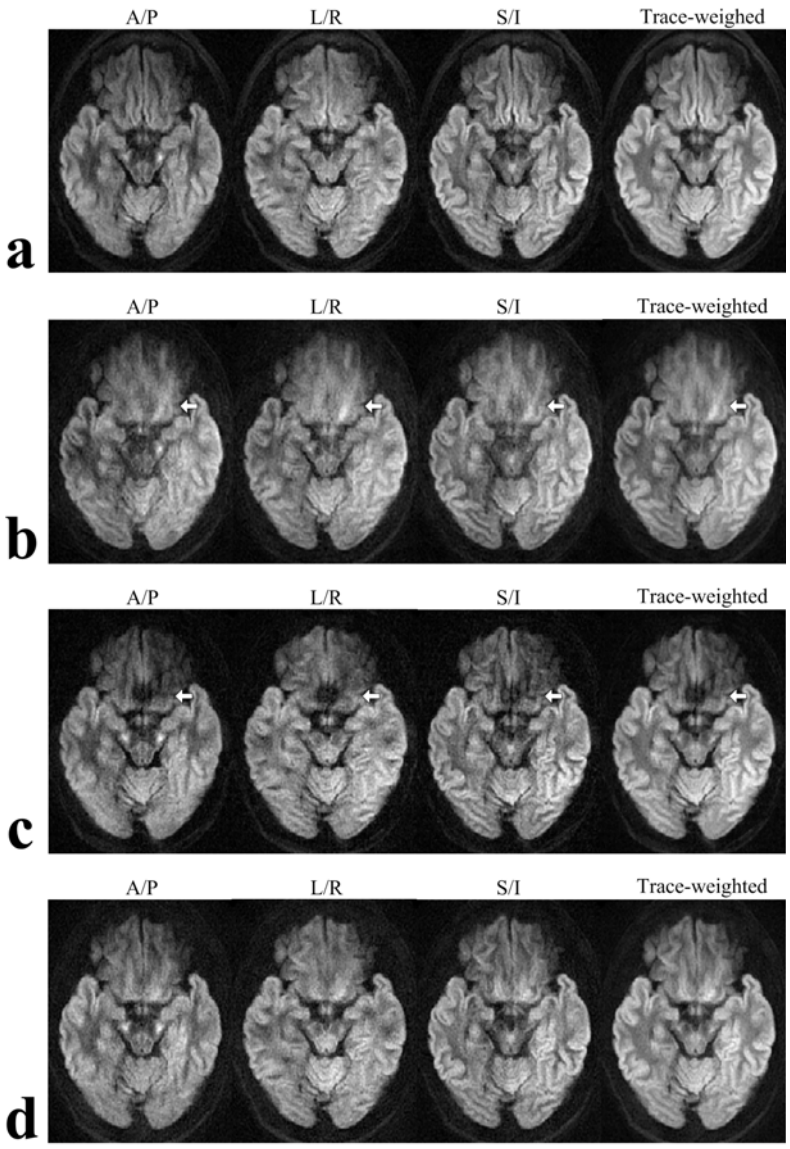

Figure 6.10: DW images with b = 1000 s/mm^2 along three orthogonal directions (from left to right): Anterior/Posterior (A/P), Left/Right (L/R), and Superior/Inferior (S/I) by a: conventional PROPELLER (turbo = 1), b: Turboprop (turbo = 7), c: X-prop (turbo = 7), and d: Turboprop+ (turbo = 7). Trace-weighted images (geometric average of three orthogonal DW images) are shown on the right. All were undersampled with R = 2. Imaging parameters were: FOV = 240 mm, slice thickness = 5 mm, matrix = 192, and ETL = 10. 1 out of 20 slices is shown with scan time: PROPELLER (4 min 14 sec), Turboprop (2 min), X-prop (1 min 37 sec), and Turboprop+ (2min).

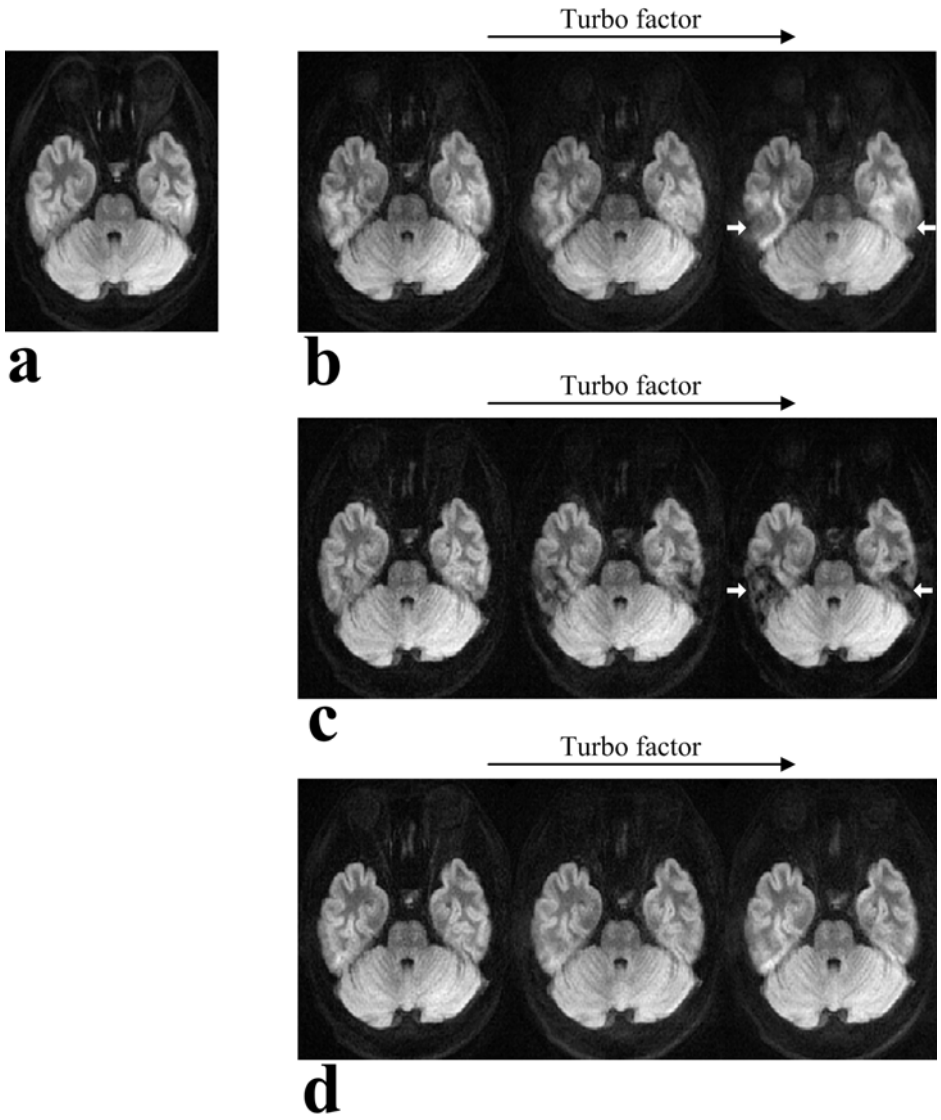

Figure 6.11: Effects of the turbo factor on trace-weighted images (geometric average of three orthogonal DW images with b = 1000 s/mm^2) by a: conventional PROPELLER (turbo = 1), b: Turboprop, c: X-prop, and d: Turboprop+ with an increase in turbo factor from 3 to 7 (left to right). White arrows indicate regions susceptible to the changes in the turbo factor. All were undersampled with R = 2. Imaging parameters were: FOV = 240 mm, slice thickness = 5 mm, matrix = 192. 1 out of 20 slices is shown with total scan time: PROPELLER (4 min 14 sec), Turboprop (2 min), X-prop (1 min 37 sec), and Turboprop+ (2 min).

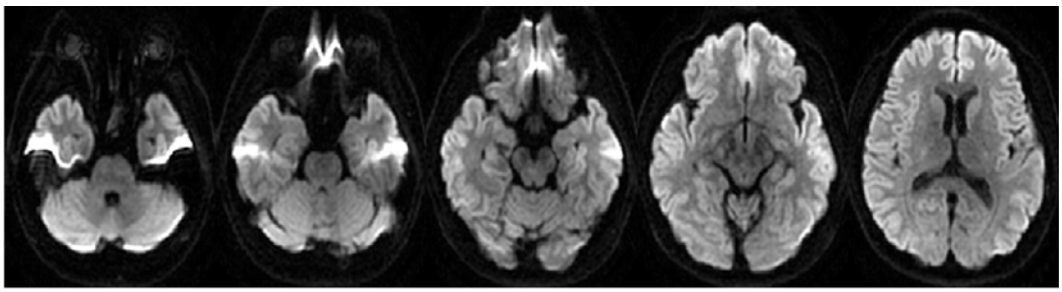

a

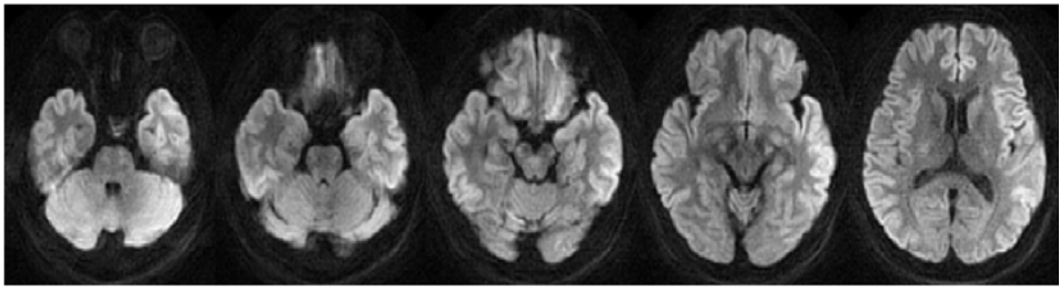

b

Figure 6.12: Trace-weighted images (geometric average of three orthogonal DW images with b = 1000 s/mm^2) by a: EPI, and b: Turboprop+ (turbo = 7). All were undersampled with R = 2. Imaging parameters were: FOV = 240 mm, slice thickness = 5 mm, matrix = 128 × 128 (EPI), and 144 (Turboprop+), and ETL = 10 (Turboprop+). 5 out of 20 slices are shown with scan time: EPI (23 sec), and Turboprop+ (52 sec).

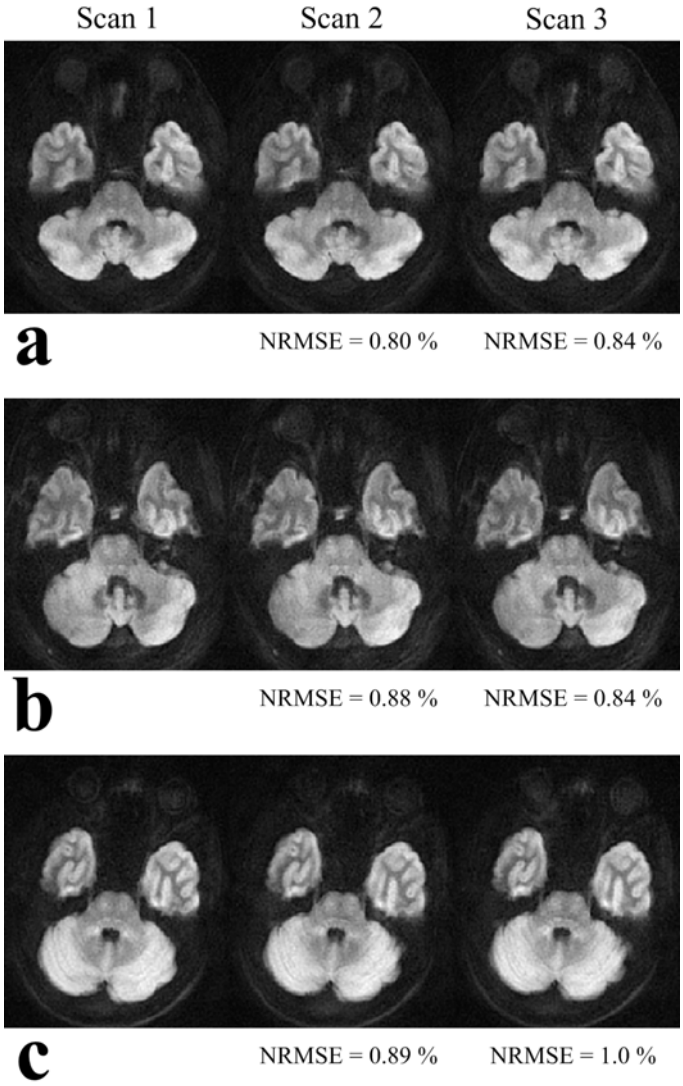

Figure 6.13: Trace-weighted images (geometric average of three orthogonal DW images with b = 1000 s/mm^2) of three healthy volunteers (a-c) from three consecutive scans (from left to right) using Turboprop+ (turbo = 7). The phase error maps acquired during the first scan (Scan 1) were used for the phase correction of all the three Turboprop+ scans (Scan 1-3). The NRMSE quantifies the differences between the reconstructed images using the 'inter-scan' phase error maps and those using the 'intra-scan' phase error maps. All were undersampled with R = 2. Imaging parameters were: FOV = 240 mm, slice thickness = 5 mm, matrix = 192, and ETL = 10. 1 out of 20 slices are shown with total scan time of three scans: 6 min (each scan took 2 min).

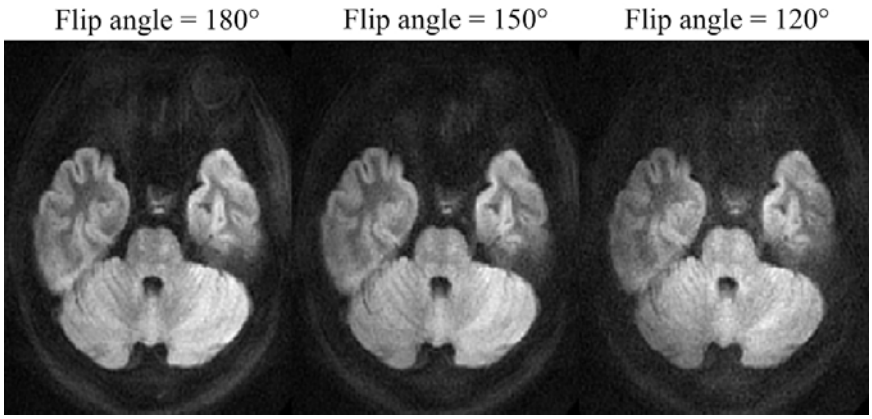

Figure 6.14: Trace-weighted images (geometric average of three orthogonal DW images with b = 1000 s/mm^2) by Turboprop+ (turbo = 7) with a decrease in the flip angle of RF refocusing pulses from 180° to 120° (from left to right). All were undersampled with R = 2. Imaging parameters were: FOV = 240 mm, slice thickness = 5 mm, matrix = 192, and ETL = 10. 1 out of 20 slices is shown with scan time: 2 min.

The rationale of the 2-D image-space phase correction in Turboprop+ relies on a consistent phase error in each sub-blade. The identical gradient polarity of the phase-encoded lines renders the consistent phase errors in a sub-blade arising from eddy currents and hardware group delays. Similar ideas have been previously proposed by Buonocore et al. [120] and Chen et al. [125] to address the odd/even echo inconsistencies in EPI. The consistent off-resonance related phase accumulation in a sub-blade requires a near-ideal 180° flip angle of each RF refocusing pulse to avoid the undesired echoes coming from multiple signal pathways. This requirement seemed sufficiently fulfilled throughout the demonstrated experiments, but could be problematic for a long echo train in the presence of B_1 field inhomogeneity because of the non-CPMG condition, particularity at a low flip angle (Fig. 6.14). These effects from multiple signal

pathways are nonetheless reduced in Turboprop+ by allowing a higher turbo factor and ultimately requiring fewer RF refocusing pulses for *k*-space sampling.

The phase-encoding order of GRASE sequences can be implemented in different ways, and has been shown to influence the image artifacts caused by phase errors [126]. The presented phase correction in Turboprop+, however, is only compatible with the standard phase encoding order used in GRASE [18]. The standard phase encoding order was also applied to Turboprop for the purpose of this study. Further investigation is required to address this concern.

Unlike Turboprop with the 1-D reference scan method, the presented 2-D phase correction enables Turboprop+ to correct phase errors along both the frequency-encoded and phase-encoded directions. However, the assumption of the slowly varying phase error in space may no longer hold when the turbo factor is high. This is an important limiting factor because the ETL, related to the calibration blade width, tends to be short for the high turbo factor to avoid a prolonged T_E. The rapid spatially varying phase errors along the phase-encoded direction can possibly move the majority of *k*-space data out of the calibration blade. This issue was addressed in this study using the parallel imaging method [124]. With the highest applied turbo factor of 7 and an ETL of 10, which results in a calibration blade width of 18, the artifacts from the phase error in Turboprop+, although not removed completely, were for the most part mitigated.

Turboprop+ and X-prop share the similarity that both the phase errors are removed using image-space phase correction by assuming phase errors to be slowly varying in space. In X-prop, the data blades formed by the each gradient echo are placed in central *k*-space (Fig. 6.4). Instead, in Turboprop+, the

sub-blade with the minimal off-resonance related phase errors (e.g. echo B in Fig. 6.9b) is assigned to the center of *k*-space, and the sub-blade with larger off-resonance related phase errors (echo A, C in Fig. 6.9b) is assigned to the outer *k*-space. This minimizes the artifacts from T_2^* signal decay in Turboprop+.

In conclusion, Turboprop+ was proposed in this study to mitigate the phase errors inherent to Turboprop. The improvements allows Turboprop to retain all its advantages relative to conventional PROPELLER, namely short scan time, low SAR, and reduced sensitivity to bulk motion (wider blade) with phase error induced artifacts being further minimized in Turboprop+.

Chapter 7

CONCULSIONS

7.1 Summary and Contributions

This work is dedicated to two aspects of diffusion-weighted MR imaging. One aspect is the phenomenological diffusion modeling. The other aspect is the data acquisition using PROPELLER technique. The summary as well as the contributions of this work is described below.

7.1.1 Behaviors of Phenomenological Diffusion Models

In this study, we have studied the fitted parameters of two non-Gaussian water diffusion models: D_{stat} and σ_{stat} of the statistical distribution model and D_{app} and K_{app} of the DKI model using a b = 2500 s/mm^2, and the ADC of the monoexponential model using a b = 1000 s/mm^2. We fitted these models to the DWI data collected from patients with ischemic stroke (n = 5) and recurrent gliomas (n = 7). Compared with the white matter, brain lesion of ischemic stroke showed the reduced diffusivity, reduced width σ_{stat} of distribution of diffusion rates (P(D)), and increased non-Gaussian water diffusion (K_{app}). Recurrent high-grade brain tumor showed the increased diffusivity, increased width σ_{stat} of distribution of diffusion rates (P(D)), and decreased non-Gaussian water diffusion (K_{app}). These results suggest that each of the fitted parameter has different correlation with the pathological changes. We hypothesized that these observed differences were caused by the different sensitivity of the diffusion models in response to microstructural changes. In particular, the models of non-Gaussian water diffusion were more specific to microstructural changes.

To test the hypothesis, we developed a Monte Carlo simulation of water diffusion in a 2-D microstructure and a DWI experiment. We have simulated three relevant microstructural changes: cell radius, cell volume fraction, and membrane permeability. We have shown that the ADC, D_{stat}, and D_{app} were sensitive to all these changes except for the decrease in membrane permeability. The σ_{stat} was specifically sensitive to the increase and decrease in cell volume fraction. The K_{app} was specifically sensitive to the decrease in cell size and the increase in membrane permeability. Our simulated microstructure is a simplistic physical system. Nonetheless, these results suggest that the models of non-Gaussian water diffusion have different, specific sensitivities and may be used together to better understand underlying biophysical changes due to disease progression.

7.1.2 Enhanced PROPELLER DWI

In this study, we have presented an improvement to the whole blade method by utilizing reference blades to more accurately calibrate the coil phase of odd and even echoes and for GRAPPA training. We have demonstrated that the phase inconsistencies between odd and even echoes were successfully addressed using the improved whole blade method. Furthermore, the self-navigated region became larger using the whole blade method (4 times larger than that using the split blade method), resulting in a more robust removal of the motion induced phase.

High SAR and long scan time are important challenges of PROPELLER data acquisition. In this work, we have proposed a new phase correction to Turboprop, called Turboprop+. We have shown that compared with previous conventional Turboprop and X-prop, the presented Turboprop+ was more immune to the phase

error resulting from off-resonance throughout the increase of turbo factor from 3 to 7. Thus, turboprop+ allows the high turbo factor in PROPELLER, further reducing SAR and scan time without compromising the image quality.

7.2 Future Work and Directions

The presented simulation of 2-D microstructure is a simplified physical system, and is insufficient to account for the complexity of intra/extra-cellular structures. Nonetheless, the idea of altering cell size, cell volume fraction, and membrane permeability independently may be realized in biological tissues. For instance, previous work by Latour et al. [29] used packed erythrocytes to study the time dependence of the diffusion coefficient by varying the membrane permeability and extracellular volume fraction independently. In the future, the *ex vivo* experiments can be devised to mimic the pathological changes and to study the relative sensitivities between diffusion models. However, cautions should be taken about the different biophysical properties between various cell types.

Our simulation is a 2-D system, and no investigation about the directional dependence of the measured diffusion was performed. Because our simulation study showed that the non-Gaussian diffusion models performed differently from the monoexponential model, one would expect that the non-Gaussian diffusion models would reveal different information about the anisotropic microstructural changes in contrast to DTI. Other groups have developed theoretical frameworks to look into the directional dependence [88,127-129]. In the future, our 2-D simulation can be extended to 3-D geometry, such as crossing fibers [130], and randomly oriented cylinders [55].

The stable image quality of Turboprop+ at the high turbo factor provides a potential for a single-shot acquisition. The multi-shot acquisition produces high-resolution DWI images. However, it remains difficult to robustly remove the motion induced phase when non-rigid motion occurs, such as respiratory motion in human body. Therefore, a single-shot method may have a potential application in body DWI. For the current implemented Turboprop+, the highest turbo factor is 7 with ETL of 10. If a whole-blade method is applied to Turboprop+, the resolution in phase-encoded direction would be 126 (with parallel imaging), which is very close to the typical resolution of EPI method: 128. However, the issues including the phase inconsistencies in the whole-blade method still have to be addressed.

REFERENCES

[1]. P. W. Schaefer, P. E. Grant, and R. G. Gonzalez, "Diffusion-weighted MR Imaging of the Brain," *Radiology*, vol. 217, pp. 331-345, 2000.

[2]. T. L. Chenevert, L. D. Stegman, J. M. Taylor, P. L. Robertson, H. S. Greenberg, A. Rehemtulla, and B. D. Ross, "Diffusion magnetic resonance imaging: an early surrogate marker of therapeutic efficacy in brain tumors," *Journal of the National Cancer Institute*, vol. 92, pp. 2029-2036, 2000.

[3]. D. Le Bihan, "The 'wet mind': water and functional neuroimaging," *Physics in Medicine and Biology*, vol. 52, pp. R57-R90, 2007.

[4]. D.S. Grebenkov, "Use, misuse, and abuse of apparent diffusion coefficients," *Concepts in Magnetic Resonance*, vol. 36A, pp. 24-35, 2010.

[5]. P. N. Sen, "Time-dependent diffusion coefficient as a probe of geometry," *Concepts in Magnetic Resonance*, vol. 23A, pp. 1-21, 2004.

[6]. Y. Assaf, and Y. Cohen, "In vivo and in vitro bi-exponential diffusion of N-acetyl aspartate (NAA) in rat brain: a potential structural probe?," *NMR in Biomedicine*, vol. 11, pp. 67-74, 1998.

[7]. R. V. Mulkern, H. P. Zengingonul, R. L. Robertson, P. Bogner, K. H. Zou, H. Gudbjartsson, C. R.G. Guttmann, D. Holtzman, W. Kyriakos, F. A. Jolesz, and S. E. Maier, "Multi-component apparent diffusion coefficients in human brain," *NMR in Biomedicine*, vol. 12, pp. 51-62, 1999.

[8]. T. Niendorf, R. M. Dijkhuizen, D. G. Norris, M. van Lookeren Campagne, and K. Nicolay, "Biexponential diffusion attenuation in various states of brain tissue: implications for diffusion-weighted imaging," *Magnetic Resonance in Medicine*, vol. 36, pp. 847-857, 1996.

[9]. C.A. Clark, and D. Le Bihan, "Water diffusion compartmentation and anisotropy at high b values in the human brain," *Magnetic Resonance in*

Medicine, vol. 44, pp. 852-859, 2000.

[10]. D. A. Yablonskiy, L. G. Bretthorst, and J. J. Ackerman, "Statistical model for diffusion attenuated MR signal," *Magnetic Resonance in Medicine*, vol. 50, pp. 664-669, 2003.

[11]. K. M. Bennett, K. M. Schmainda, R. Bennett, D. B. Rowe, H. Lu, and J. S. Hyde, "Characterization of continuously distributed cortical water diffusion rates with a stretched-exponential model," *Magnetic Resonance in Medicine*, vol. 50, pp. 727-734, 2003.

[12]. J. H. Jensen, J. A. Helpern, A. Ramani, H. Lu, and K. Kaczynski, "Diffusional kurtosis imaging: the quantification of non-gaussian water diffusion by means of magnetic resonance imaging," *Magnetic Resonance in Medicine*, vol. 53, pp. 1432-1440, 2005.

[13]. D. A. Yablonskiy, and A. L. Sukstanskii, "Theoretical models of the diffusion weighted MR signal," *NMR in Biomedicine*, vol. 23, pp. 661-681, 2010.

[14]. R. Bammer, M. Auer, S. L. Keeling, M. Augustin, L. A. Stables, R. W. Prokesch, R. Stollberger, M. E. Moseley, and F. Fazekas, "Diffusion tensor imaging using single-shot SENSE-EPI," *Magnetic Resonance in Medicine*, vol. 48, pp. 128-136, 2002.

[15]. J. G. Pipe, V. G. Farthing, and K. P. Forbes, "Multishot diffusion-weighted FSE using PROPELLER MRI," *Magnetic Resonance in Medicine*, vol. 47, pp. 42-52, 2002.

[16]. J. G. Pipe, and N. Zwart, "Turboprop: improved PROPELLER imaging," *Magnetic Resonance in Medicin*, vol. 55, pp. 380-385, 2006.

[17]. D. Huo, Z. Li, E. Aboussouan, J. Karis, and J. Pipe, "Turboprop IDEAL: a motion-resistant fat-water separation technique," *Magnetic Resonance in Medicine*, vol. 61, pp. 188-195, 2009.

[18]. K. Oshio, and D. A. Feinberg, "GRASE (Gradient- and spin-echo) imaging: a novel fast MRI technique," *Magnetic Resonance in Medicine*, vol. 20, pp. 344-349, 1991.

[19]. H.-J. Smith, and F. Ranallo. *A Non-mathematical Approach to Basic MRI*. Wisconsin: Medical Physics Publishing, 1989.

[20]. A. D. Elster. *Questions and Answers in Magnetic Resonance Imaging*. Missouri: Mosby-Year Book, 1994.

[21]. D. G. Nishimura. *Principles of Magnetic Resonance Imaging*. Stanford University Press, 1996.

[22]. R. Brown, "A brief account of microscopical observations made in the months of June, July and August, 1827, on the particles contained in the pollen of plants; and on the general existence of active molecules in organic and inorganic bodies," *Edinburgh new Philosophical Journal*, vol. 4, pp. 161-173, 1828.

[23]. A. Einstein. *Investigations on the Theory of the Brownian Movement*. New York: Dover, 1956.

[24]. R. Metzler, and J. Klafter, "The random walk's guide to anomalous diffusion: a fractional dynamics approach," *Physics Reports*, vol. 339, pp. 1-77, 2000.

[25]. M. Kopf, C. Corinth, O. Haferkamp, and T. F. Nonnenmacher, "anomalous diffusion of water in biological system," *Biophysical Journal*, vol. 70, pp. 2950-2958, 1996.

[26]. J. Crank. *The Mathematics of Diffusion*. Oxford University Press, USA, 1980.

[27]. A. Papoulis. *Probability, Random Variables and Stochastic Processes*. McGraw-Hill Companies, 1991.

[28]. C. Nicholson, and J. M. Phillips, "Ion diffusion modified by tortuosity and volume fraction in the extracellular microenvironment of the rat cerebellum," *The Journal of physiology*, vol. 321, pp. 225-257, 1981.

[29]. L. L. Latour, K. Svoboda, P. P. Mitra, and C. H. Sotak, "Time-dependent diffusion of water in a biological model system," *Proceedings of the National Academy of Sciences*, vol. 91, pp. 1229-1233, 1994.

[30]. A. Szafer, J. Zhong, and J. C. Gore, "Theoretical model for water diffusion in tissues," *Magnetic Resonance in Medicine*, vol. 33, pp. 697-712, 1995.

[31]. J. Kärger, "NMR self-diffusion studies in heterogeneous systems," *Advances in Colloid and Interface Science*, vol. 23, pp. 129-148, 1985.

[32]. J. E. Tanner, "Transient diffusion in a system partitioned by permeable barriers. Application to NMR measurements with a pulsed field gradient," *The Journal of Chemical Physics*, vol. 69, pp. 1748-1754, 1978.

[33]. E. O. Stejskal, and J. E. Tanner, "Spin Diffusion Measurements: Spin Echoes in the Presence of a Time-Dependent Field Gradient," *The Journal of Chemical Physics*, vol. 42, pp. 288-292, 1965.

[34]. P. T. Callaghan. *Principles of Nuclear Magnetic Resonance Microscopy*. Clarendon Press, Oxford, 1991.

[35]. H. Y. Carr, and E. M. Purcell, "Effects of Diffusion on Free Precession in Nuclear Magnetic Resonance Experiments," *Physical Review*, vol. 94, pp. 630-638, 1954.

[36]. D. G. Taylor, and M. C. Bushell, "The spatial mapping of translational diffusion coefficients by the NMR imaging technique," *Physics in Medicine and Biology*, vol. 30, pp. 345-349, 1985.

[37]. J. E. Tanner, and E. O. Stejskal, "Restricted Self-Diffusion of Protons in Colloidal Systems by the Pulsed-Gradient, Spin-Echo Method," *The Journal of Chemical Physics*, vol. 49, pp. 1768-1777, 1968.

[38]. P. Callaghan, "Pulsed-Gradient Spin-Echo NMR for Planar, Cylindrical, and Spherical Pores under Conditions of Wall Relaxation," *Journal of Magnetic Resonance, Series A*, vol. 113, pp. 53-59, 1995.

[39]. C. H. Neuman, "Spin echo of spins diffusing in a bounded medium," *The Journal of Chemical Physics*, vol. 60, pp. 4508-4511, 1974.

[40]. P. Linse, "The Validity of the Short-Gradient-Pulse Approximation in NMR Studies of Restricted Diffusion. Simulations of Molecules Diffusing between Planes, in Cylinders and Spheres," *Journal of Magnetic Resonance, Series A*, vol. 116, pp. 77-86, 1995.

[41]. P. W. Kuchel, A. Coy, and P. Stilbs, "NMR "diffusion-diffraction" of water revealing alignment of erythrocytes in a magnetic field and their dimensions and membrane transport characteristics," *Magnetic Resonance in Medicine*, vol. 37, pp. 637-643, 1997.

[42]. Y. Cohen, and Y. Assaf, "High b-value q-space analyzed diffusion-weighted MRS and MRI in neuronal tissues - a technical review," *NMR in Biomedicine*, vol. 15, pp. 516-542, 2002.

[43]. W. S. Price, P. Stilbs, and O. Söderman, "Determination of pore space shape and size in porous systems using NMR diffusometry. Beyond the short gradient pulse approximation," *Journal of Magnetic Resonance*, vol. 160, pp. 139-143, 2003.

[44]. N. Shemesh, E. Ozarslan, P. Basser, and Y. Cohen, "Detecting diffusion-diffraction patterns in size distribution phantoms using double-pulsed field gradient NMR: Theory and experiments," *The Journal of Chemical Physics*, vol. 132, pp. 034703, 2010.

[45]. J. Lätt, M. Nilsson, R. Wirestam, E. Johansson, E. M. Larsson, F. Stahlberg, and S. Brockstedt, "In vivo visualization of displacement-distribution-derived parameters in q-space imaging," *Magnetic Resonance Imaging*, vol. 26, pp. 77-87, 2008.

[46]. M. E. Moseley, Y. Cohen, J. Mintorovitch, L. Chileuitt, H. Shimizu, J. Kucharczyk, M. F. Wendland, and P. R. Weinstein, "Early detection of regional cerebral ischemia in cats: comparison of diffusion- and T2-weighted MRI and spectroscopy," *Magnetic Resonance in Medicine*, vol. 14, pp. 330-346, 1990.

[47]. J. A. Helpern, R. J. Ordidge, and R. A. Knight, "The effect of cell membrane water permeability on the apparent diffusion coefficient of water," in *Proceedings of the International Society of Magnetic Resonance in Medicine*, Germany, 1992, p. 1201.

[48]. A. van der Toorn, R. M. Dijkhuizen, C. A. F. Tulleken, and K. Nicolay, "Diffusion of metabolites in normal and ischemic rat brain measured by localized 1H MRS," *Magnetic Resonance in Medicine*, vol. 36, pp. 914-922, 1996.

[49]. M. E. Moseley, Y. Cohen, J. Kucharczyk, J. Mintorovitch, H. S. Asgari, M. F. Wendland, J. Tsuruda, and D. Norman, "Diffusion-weighted MR imaging of anisotropic water diffusion in cat central nervous system," *Radiology*, vol. 176, pp. 439-445, 1990.

[50]. P. Douek, R. Turner, J. Pekar, N. Patronas, and D. Le Bihan, "MR color mapping of myelin fiber orientation," *Journal of computer assisted tomography*, vol. 15, pp. 923-929, 1991.

[51]. K. M. Hasan, D. L. Parker, and A. L. Alexander, "Comparison of gradient encoding schemes for diffusion-tensor MRI," *Journal of Magnetic Resonance Imaging*, vol. 13, pp. 769-780, 2001.

[52]. D. Jones, "The effect of gradient sampling schemes on measures derived from diffusion tensor MRI: a Monte Carlo study," *Magnetic Resonance in Medicine*, vol. 51, pp. 807-815, 2004.

[53]. K. M. Hasan, A. L. Alexander, and Narayana, "Does fractional anisotropy have better noise immunity characteristics than relative anisotropy in diffusion tensor MRI? An analytical approach," *Magnetic Resonance in*

Medicine, vol. 51, pp. 413-417, 2004.

[54]. P. J. Basser, and C. Pierpaoli, "Microstructural and physiological features of tissues elucidated by quantitative-diffusion-tensor MRI," *Journal of magnetic resonance Series B*, vol. 111, pp. 209-219, 1996.

[55]. N. Shemesh, and Y. Cohen, "Microscopic and compartment shape anisotropies in gray and white matter revealed by angular bipolar double-PFG MR," *Magnetic Resonance in Medicine*, vol. 65, pp. 1216-1227, 2011.

[56]. J. D. Tournier, S. Mori, and A. Leemans, "Diffusion tensor imaging and beyond," *Magnetic Resonance in Medicine*, vol. 65, pp. 1532-1556, 2011.

[57]. A. W. Anderson, and J. C. Gore, "Analysis and correction of motion artifacts in diffusion weighted imaging," *Magnetic Resonance in Medicine*, vol. 32, pp. 379-387, 1994.

[58]. R. Bammer, "Basic principles of diffusion-weighted imaging," *European Journal of Radiology*, vol. 45, pp. 169-184, 2003.

[59]. X. Hu, and T. H. Le, "Artifact reduction in EPI with phase-encoded reference scan," *Magnetic Resonance in Medicine*, vol. 36, pp. 166-171, 1996.

[60]. M. A. Bernstein, K. F. King, and X. J. Zhou. *Handbook of MRI Pulse Sequences*. Massachusetts: Elsevier, 2004.

[61]. H. Bruder, H. Fischer, H. E. Reinfelder, and F. Schmitt, "Image reconstruction for echo planar imaging with nonequidistant k-space sampling," *Magnetic Resonance in Medicine*, vol. 23, pp. 311-323, 1992.

[62]. C. L. Ham, J. M. Engels, G. T. van de Wiel, and A. Machielsen, "Peripheral nerve stimulation during MRI: effects of high gradient amplitudes and switching rates," *Journal of Magnetic Resonance Imaging*, vol. 7, pp. 933-937, 1997.

[63]. J. Hennig, "Multiecho imaging sequences with low refocusing flip angles," *Journal of Magnetic Resonance*, vol. 78, pp. 397-407, 1988.

[64]. S. Meiboom, and D. Gill, "Modified Spin-Echo Method for Measuring Nuclear Relaxation Times," *Review of Scientific Instruments*, vol. 29, pp. 688-691, 1958.

[65]. P. Le Roux, "Non-CPMG Fast Spin Echo with full signal," *Journal of Magnetic Resonance*, vol. 155, pp. 278-292, 2002.

[66]. A. J. Shaka, S. P. Rucker, and A. Pines, "Iterative carr-purcell trains," *Journal of Magnetic Resonance (1969)*, vol. 77, pp. 606-611, 1988.

[67]. T. C. Kwee, C. J. Galbán, C. Tsien, L. Junck, P. C. Sundgren, M. K. Ivancevic, T. D. Johnson, C. R. Meyer, A. Rehemtulla, B. D. Ross, and T. L. Chenevert, "Comparison of apparent diffusion coefficients and distributed diffusion coefficients in high-grade gliomas," *Journal of Magnetic Resonance Imaging*, vol. 31, pp. 531-537, 2010.

[68]. T. C. Kwee, C. J. Galbán, C. Tsien, L. Junck, P. C. Sundgren, M. K. Ivancevic, T. D. Johnson, C. R. Meyer, A. Rehemtulla, B. D. Ross, and T. L. Chenevert, "Intravoxel water diffusion heterogeneity imaging of human high-grade gliomas," *NMR in Biomedicine*, vol. 23, pp. 179-187, 2010.

[69]. M. F. Falangola, J. H. Jensen, J. S. Babb, C. Hu, F. X. Castellanos, A. Di Martino, S. H. Ferris, and J. A. Helpern, "Age-related non-Gaussian diffusion patterns in the prefrontal brain," *Journal of Magnetic Resonance Imaging*, vol. 28, pp. 1345-1350, 2008.

[70]. P. Raab, E. Hattingen, K. Franz, F. E. Zanella, and H. Lanfermann, "Cerebral Gliomas: Diffusional Kurtosis Imaging Analysis of Microstructural Differences1," *Radiology*, vol. 254, pp. 876-881, 2010.

[71]. K. M. Bennett, J. S. Hyde, S. D. Rand, R. Bennett, H. G.. J. Krouwer, K. J. Rebro, and K. M. Schmainda, "Intravoxel distribution of DWI decay rates reveals C6 glioma invasion in rat brain," *Magnetic Resonance in Medicine*,

vol. 52, pp. 994-1004, 2004.

[72]. S. Maier, P. Bogner, G. Bajzik, H. Mamata, Y. Mamata, I. Repa, F. Jolesz, and R. Mulkern, "Normal Brain and Brain Tumor: Multicomponent Apparent Diffusion Coefficient Line Scan Imaging," *Radiology*, vol. 219, pp. 842-849, 2001.

[73]. P. Brugieres, P. Thomas, A. Maraval, H. Hosseini, C. Combes, A. Chafiq, L. Ruel, S. Breil, M. Peschanski, and A. Gaston, "Water Diffusion Compartmentation at High b Values in Ischemic Human Brain," *American Journal of Neuroradiology*, vol. 25, pp. 692-698, 2004.

[74]. S. N. Jespersen, C. D. Kroenke, L. Østergaard, J. J. Ackerman, and D. A. Yablonskiy, "Modeling dendrite density from magnetic resonance diffusion measurements," *Neuroimage*, vol. 34, pp. 1473-1486, 2007.

[75]. G. J. Stanisz, A. Szafer, G. A. Wright, and R. M. Henkelman, "An analytical model of restricted diffusion in bovine optic nerve," *Magnetic Resonance in Medicine*, vol. 37, pp. 103-111, 1997.

[76]. Y. Assaf, and P. Basser, "Composite hindered and restricted model of diffusion (CHARMED) MR imaging of the human brain," *Neuroimage*, vol. 27, pp. 48-58, 2005.

[77]. P. N. Sen, and P. Basser, "A Model for Diffusion in White Matter in the Brain," *Biophysical Journal*, vol. 89, pp. 2927-2938, 2005.

[78]. K. P. Whittall, and A. L. Mackay, "Quantitative interpretation of NMR relaxation data," *Journal of Magnetic Resonance*, vol. 84, pp. 134-152, 1989.

[79]. A. Schwarcz, Z. Ursprung, Z. Berente, P. Bogner, G. Kotek, P. Meric, B. Gillet, J.C. Beloeil, and T. Dóczi, "In vivo brain edema classification: New insight offered by large b-value diffusion-weighted MR imaging," *Journal of Magnetic Resonance Imaging*, vol. 25, pp. 26-31, 2007.

[80]. E. Syková, J. Svoboda, J. Polák , and A. Chvátal, "Extracellular volume fraction and diffusion characteristics during progressive ischemia and terminal anoxia in the spinal cord of the rat," *Journal of cerebral blood flow and metabolism*, vol. 14, pp. 301-311, 1994.

[81]. J. V. Sehy, J. J. Ackerman, and J. J. Neil, "Evidence that both fast and slow water ADC components arise from intracellular space," *Magnetic Resonance in Medicine*, vol. 48, pp. 765-770, 2002.

[82]. A. Schwarcz, P. Bogner, P. Meric, J. L. Correze, Z. Berente, J. Pál, F. Gallyas, T. Doczi, B. Gillet, and J. C. Beloeil, "The existence of biexponential signal decay in magnetic resonance diffusion-weighted imaging appears to be independent of compartmentalization," *Magnetic Resonance in Medicine*, vol. 51, pp. 278-285, 2004.

[83]. V. G. Kiselev, and K. A. Il'yasov, "Is the "biexponential diffusion" biexponential?," *Magnetic Resonance in Medicine*, vol. 57, pp. 464-469, 2007.

[84]. J. Pfeuffer, S. W. Provencher, and R. Gruetter, "Water diffusion in rat brain in vivo as detected at very large values is multicompartmental," *Magnetic Resonance Materials in Physics, Biology and Medicine*, vol. 8, pp. 98-108, 1999.

[85]. S. W. Provencher, "A constrained regularization method for inverting data represented by linear algebraic or integral equations," *Computer Physics Communications*, vol. 27, pp. 213-227, 1982.

[86]. R. Richert, "Homogeneous dispersion of dielectric responses in a simple glass," *Journal of Non-Crystalline Solids*, vol. 172-174, pp. 209-213, 1994.

[87]. M. G. Hall, and T. R. Barrick, "From diffusion-weighted MRI to anomalous diffusion imaging," *Magnetic Resonance in Medicine*, vol. 59, pp. 447-455, 2008.

[88]. S. De Santis, A. Gabrielli, M. Bozzali, B. Maraviglia, E. Macaluso, and S. Capuani, "Anisotropic anomalous diffusion assessed in the human brain by scalar invariant indices," *Magnetic Resonance in Medicine*, vol. 65, pp. 1043-1052, 2011.

[89]. R. L. Magin, O. Abdullah, D. Baleanu, and X. J. Zhou, "Anomalous diffusion expressed through fractional order differential operators in the Bloch Torrey equation," *Journal of Magnetic Resonance*, vol. 190, pp. 255-270, 2008.

[90]. X. J. Zhou, Q. Gao, O. Abdullah, and R. L. Magin, "Studies of anomalous diffusion in the human brain using fractional order calculus," *Magnetic Resonance in Medicine*, vol. 63, pp. 562-569, 2010.

[91]. A. F. Fr, L., and V. G. Kiselev, "Effect of impermeable boundaries on diffusion-attenuated MR signal," *Journal of Magnetic Resonance*, vol. 179, pp. 223-233, 2006.

[92]. L. Zhao, A. L. Sukstanskii, C. D. Kroenke, J. Song, D. Piwnica-Worms, J. J. Ackerman, and J. J. Neil, "Intracellular water specific MR of microbead-adherent cells: HeLa cell intracellular water diffusion," *Magnetic Resonance in Medicine*, vol. 59, pp. 79-84, 2008.

[93]. J. A. Helpern, V. Adisetiyo, M. F. Falangola, C. Hu, A. Di Martino, K. Williams, F. X. Castellanos, and J. H. Jensen, "Preliminary evidence of altered gray and white matter microstructural development in the frontal lobe of adolescents with attention-deficit hyperactivity disorder: A diffusional kurtosis imaging study," *J Magn Reson Imaging*, vol. 33, pp. 17-23, 2011.

[94]. J. S. Cheung, E. Wang, E. H. Lo, and P. Z. Sun, "Stratification of heterogeneous diffusion MRI ischemic lesion with kurtosis imaging: evaluation of mean diffusion and kurtosis MRI mismatch in an animal model of transient focal ischemia," *Stroke; a journal of cerebral circulation*, vol. 43, pp. 2252-2254, 2012.

[95]. J. Zhuo, S. Xu, J. L. Proctor, R. J. Mullins, J. Z. Simon, G. Fiskum, and R. P. Gullapalli, "Diffusion kurtosis as an in vivo imaging marker for reactive astrogliosis in traumatic brain injury," *NeuroImage*, vol. 59, pp. 467-477, 2012.

[96]. E. S. Hui, F. Du, S. Huang, Q. Shen, and T. Q. Duong, "Spatiotemporal dynamics of diffusional kurtosis, mean diffusivity and perfusion changes in experimental stroke," *Brain Research*, vol. 1451, pp. 100-109, 2012.

[97]. S. Van Cauter, J. Veraart, J. Sijbers, R. Peeters, U. Himmelreich, F. De Keyzer, S. Van Gool, F. Van Calenbergh, S. De Vleeschouwer, W. Van Hecke, and S. Sunaert, "Gliomas: Diffusion Kurtosis MR Imaging in Grading," *Radiology*, vol. 263, pp. 492-501, 2012.

[98]. P. R. Bevington and D. K. Robinson. *Data Reduction and Error Analysis for the Physical Sciences*. New York: McGraw-Hill, 1992.

[99]. J. H. Jensen, M. F. Falangola, C. Hu, A. Tabesh, O. Rapalino, C. Lo, and J. A. Helpern, "Preliminary observations of increased diffusional kurtosis in human brain following recent cerebral infarction," *NMR in Biomedicine*, vol. 24, pp. 452-457, 2011.

[100]. F. Grinberg, L. Ciobanu, E. Farrher, and N. Jon Shah, "Diffusion kurtosis imaging and log-normal distribution function imaging enhance the visualisation of lesions in animal stroke models," *NMR in Biomedicine*, in press.

[101]. O. Ganslandt, A. Stadlbauer, R. Fahlbusch, K. Kamada, R. Buslei, I. Blumcke, E. Moser, and C. Nimsky, "Proton magnetic resonance spectroscopic imaging integrated into image-guided surgery: correlation to standard magnetic resonance imaging and tumor cell density," *Neurosurgery*, vol. 56, pp. 2005.

[102]. M. G. Hall, and D. C. Alexander, "Convergence and parameter choice for Monte-Carlo simulations of diffusion MRI," *IEEE Transactions on*

Medical Imaging, vol. 28, pp. 1354-1364, 2009.

[103]. E. Fieremans, Y. Dedeene, S. Delputte, M. Ozdemir, Y. Dasseler, J. Vlassenbroeck, K. Deblaere, E. Achten, and I. Lemahieu, "Simulation and experimental verification of the diffusion in an anisotropic fiber phantom," *Journal of Magnetic Resonance*, vol. 190, pp. 189-199, 2008.

[104]. J. C. Ford, and D. B. Hackney, "Numerical model for calculation of apparent diffusion coefficients (ADC) in permeable cylinders -- comparison with measured ADC in spinal cord white matter," *Magnetic Resonance in Medicine*, vol. 37, pp. 387-394, 1997.

[105]. J. Coad, M. Dunstall. *Anatomy and physiology for midwives*. Edinburgh: Elsevier/Churchill Livingstone, 2005.

[106]. F. Aboitiz, A. B. Scheibel, R. S. Fisher, and E. Zaidel, "Fiber composition of the human corpus callosum," *Brain Research*, vol. 598, pp. 143-153, 1992.

[107]. J. Xu, K. Li, R. A. Smith, J. C. Waterton, P. Zhao, H. Chen, M. D. Does, H. C. Manning, and J. C. Gore, "Characterizing Tumor Response to Chemotherapy at Various Length Scales Using Temporal Diffusion Spectroscopy," *PLoS ONE*, vol. 7, pp. e41714, 2012.

[108]. E. Syková, and C. Nicholson, "Diffusion in Brain Extracellular Space," *Physiological Reviews*, vol. 88, pp. 1277-1340, 2008.

[109]. J. Zámecník, L. Vargová, A. Homola, R. Kodet, and E. Syková, "Extracellular matrix glycoproteins and diffusion barriers in human astrocytic tumours," *Neuropathology and Applied Neurobiology*, vol. 30, pp. 338-350, 2004.

[110]. M. Nilsson, J. Lätt, D. van Westen, S. Brockstedt, S. Lasič, F. Ståhlberg, and D. Topgaard, "Noninvasive mapping of water diffusional exchange in the human brain using filter-exchange imaging," *Magnetic Resonance in Medicine*, in press.

[111]. M. D. Silva, T. Omae, K. G. Helmer, F. Li, M. Fisher, and C. H. Sotak, "Separating changes in the intra- and extracellular water apparent diffusion coefficient following focal cerebral ischemia in the rat brain," *Magnetic Resonance in Medicine*, vol. 48, pp. 826-837, 2002.

[112]. J. A. Goodman, J. J. Ackerman, and J. J. Neil, "Cs + ADC in rat brain decreases markedly at death," *Magnetic Resonance in Medicine*, vol. 59, pp. 65-72, 2008.

[113]. K. Harkins, J.P. Galons, T. Secomb, and T. Trouard, "Assessment of the effects of cellular tissue properties on ADC measurements by numerical simulation of water diffusion," *Magnetic Resonance in Medicine*, vol. 62, pp. 1414-1422, 2009.

[114]. J. Xu, M. D. Does, and J. C. Gore, "Sensitivity of MR diffusion measurements to variations in intracellular structure: effects of nuclear size," *Magnetic Resonance in Medicine*, vol. 61, pp. 828-833, 2009.

[115]. G. Srinivasan, N. Rangwala, X. J. Zhou, "Steer-PROP: A GRASE-PROPELLER sequence with inter-echo steering gradient pulses," in *Proceedings of the International Society of Magnetic Resonance in Medicine*, Stockholm, 2010, p. 81.

[116]. J. G. Pipe, "Split-blade PROPELLER DWI," in *Proceedings of the International Society of Magnetic Resonance in Medicine*, Canada, 2003, p. 2126.

[117]. S. B. Reeder, E. Atalar, B. D. Bolster, and E. R. McVeigh, "Quantification and reduction of ghosting artifacts in interleaved echo-planar imaging," *Magnetic Resonance in Medicine*, vol. 38, pp. 429-439, 1997.

[118]. M. H. Buonocore, and L. Gao, "Ghost artifact reduction for echo planar imaging using image phase correction," *Magnetic Resonance in Medicine*, vol. 38, pp. 89-100, 1997.

[119]. Z. Li, J. G. Pipe, C. Y. Lee, J. P. Debbins, J. P. Karis, and D. Huo, "X-PROP: A fast and robust diffusion-weighted propeller technique," *Magnetic Resonance in Medicine*, vol. 66, pp. 341-347, 2011.

[120]. J. G. Pipe, " Whole Blade Method for Robust PROPELLER DWI," in *Proceedings of the International Society of Magnetic Resonance in Medicine*, Berlin, 2007, p. 1486.

[121]. Z. Li, J. G. Pipe, E. Aboussouan, J. P. Karis, and D. Huo, "A parallel imaging technique using mutual calibration for split-blade diffusion-weighted PROPELLER," *Magnetic Resonance in Medicine*, vol. 65, pp. 638-644, 2011.

[122]. N. K. Chen, and A. Wyrwicz, "Removal of EPI Nyquist ghost artifacts with two-dimensional phase correction," *Magnetic Resonance in Medicine*, vol. 51, pp. 1247-1253, 2004.

[123]. G. Johnson, D. A. Feinberg, and V. Venkataraman, "A comparison of phase encoding ordering schemes in T2-weighted GRASE imaging," *Magnetic Resonance in Medicine*, vol. 36, pp. 427-435, 1996.

[124]. M. G. Hall, and T. R. Barrick, "Two-step anomalous diffusion tensor imaging," *NMR in Biomedicine*, vol. 25, pp. 286-294, 2012.

[125]. E. S. Hui, M. M. Cheung, L. Qi, and E. X. Wu, "Towards better MR characterization of neural tissues using directional diffusion kurtosis analysis," *Neuroimage*, vol. 42, pp. 122-134, 2008.

[126]. H. Lu, J. H. Jensen, A. Ramani, and J. A. Helpern, "Three-dimensional characterization of non-gaussian water diffusion in humans using diffusion kurtosis imaging," *NMR in Biomedicine*, vol. 19, pp. 236-247, 2006.

[127]. G. T. Balls, and L. R. Frank, "A simulation environment for diffusion weighted MR experiments in complex media," *Magnetic Resonance in Medicine*, vol. 62, pp. 771-778, 2009.